Fall 1-31-2012

Terahertz wireless communication

Ke Su
New Jersey Institute of Technology

Recommended Citation

Su, Ke, "Terahertz wireless communication" (2012). *Dissertations*. 295.
https://digitalcommons.njit.edu/dissertations/295

ABSTRACT

TERAHERTZ WIRELESS COMMUNICATION

by
Ke Su

The goal of this thesis is to explore Terahertz (THz) wireless communication technology. More specifically the objective is to develop and characterize several THz communication systems and study the effect of atmosphere propagation through fog droplets and dust particles on THz communications.

For demonstration, a THz continuous wave (CW) photomixing system is designed. Terahertz signals are phase encoded with both analog ramp signals and pseudorandom binary data, transmitted over a short distance, and detected. The limitation of transmission bandwidth, low single to noise ratio, vibration effects are also analyzed. In order to study and compare propagation features of THz links with infrared (IR) links under different weather conditions, a THz and IR communications lab setup with a maximum data rate of 2.5 Gb/s at 625 GHz carrier frequency and 1.5 μm wavelength, have been developed respectively. A usual non return-to-zero (NRZ) format is applied to modulate the IR channel but a duobinary coding technique is used for driving the multiplier chain-based 625 GHz source, which enables signaling at high data rate and higher output power. The bit-error rate (BER), signal-to-noise ratio (SNR) and power on the receiver side have been measured, which describe the signal performance.

Since weather conditions such as fog and dust exhibit a spectral dependence in the atmospheric attenuation, the corresponding impact on THz in comparison with IR communications is not equivalent. Simulation results of attenuation by fog and dust in the millimeter and sub-millimeter waveband (from 0.1 to 1 THz) and infrared waveband (1.5

μm) are presented and compared. Experimentally, after THz and IR beams propagated through the same weather conditions (fog), performance of both channels are analyzed and compared. The attenuation levels for the IR beam are typically several orders of magnitude higher than those for the THz beam. Mie scattering theory was used to study the attenuation of THz and IR radiation due to the dust particle. Different amounts of dust are loaded in the chamber to generate a variety of concentration for beam propagation. As the dust loading becomes heavier, the measured attenuation becomes more severe. Under identical dust concentrations, IR wavelengths are strongly attenuated while THz shows almost no impact.

TERAHERTZ WIRELESS COMMUNICATION

by
Ke Su

A Dissertation
Submitted to the Faculty of
New Jersey Institute of Technology and
Rutgers, the State University of New Jersey - Newark
in Partial Fulfillment of the Requirements for the Degree of
Doctor of Philosophy in Applied Physics

Federated Department of Physics

January 2012

.

APPROVAL PAGE

TERAHERTZ WIRELESS COMMUNICATION

Ke Su

Dr. John F. Federici, Dissertation Advisor Date
Distinguished Professor of Physics, NJIT

Dr. Lothar Moeller, Committee Member Date
Bell Labs, Alcatel-Lucent, Holmdel, NJ

Dr. Tao Zhou, Committee Member Date
Associate Professor of Physics, NJIT

Dr. Andrei Sirenko, Committee Member Date
Associate Professor of Physics, NJIT

Dr. Zhen Wu, Committee Member Date
Professor of Physics, Rutgers University, Newark, NJ

Dr. Haim Grebel, Committee Member Date
Professor of Electrical and Computer Engineering, NJIT

BIOGRAPHICAL SKETCH

Author: Ke Su

Degree: Doctor of Philosophy

Date: January 2012

Undergraduate and Graduate Education:

- Doctor of Philosophy in Applied Physics,
  New Jersey Institute of Technology, Newark, NJ, 2012

- Master of Science in Material Science,
  Fudan University, Shanghai, P. R. China, 2006

- Bachelor of Science in Applied Physics,
  Zhengzhou University, Zhengzhou, P. R. China, 2003

Major: Applied Physics

Presentations and Publications:

K. Su, L. Moeller, R. B. Barat, and J. F. Federici, " Experimental comparison of performance degradation from terahertz and infrared wireless link in fog," Journal of the Optical Society of America A: Optics and Image Science, and Vision (Accepted) (2011).

J. F. Federici, L. Moeller, and K. Su, " Terahertz communications," in *Handbook of Terahertz Technology for Imaging and Sensing (Submitted)* (2011).

L. Moeller, J. F. Federici, and K. Su, "2.5 Gbit/s duobinary signalling with narrow bandwidth 0.625 terahertz source," Electronics Letters **47**, 856-858 (2011).

L. Moeller, J. F. Federici, and K. Su, "THz wireless communications: 2.5 Gb/s error-free transmission at 625 GHz using a narrow-bandwidth 1 mW THz source," in *General Assembly and Scientific Symposium, URSI,* (Istanbul 2011).

K. Su, Z. Liu, R. B. Barat, D. E. Gary, Z.-H. Michalopoulou, and J. F. Federici, "Two-dimensional interferometric and synthetic aperture imaging with a hybrid terahertz/ millimeter wave system," Appl. Opt. **49**, E13-E19 (2010).

Z.-H. Michalopoulou, S. Mukherjee, Y. Hor, K. Su, Z. Liu, R. B. Barat, D. E. Gary, and J. F. Federici, "RDX detection with THz spectroscopy," Journal of Infrared, Millimeter, and Terahertz Waves **31**, 1171-1181 (2010).

Z. Liu, K. Su, D. E. Gary, J. F. Federici, R. B. Barat, and Z.-H. Michalopoulou, "Video-rate terahertz interferometric and synthetic aperture imaging," Appl. Opt. **48**, 3788-3795 (2009).

A. M. Sinyukov, Z. Liu, Y. L. Hor, K. Su, R. B. Barat, D. E. Gary, Z.-H. Michalopoulou, I. Zorych, J. F. Federici, and D. Zimdars, "Rapid-phase modulation of terahertz radiation for high-speed terahertz imaging and spectroscopy," Opt. Lett. **33**, 1593-1595 (2008).

K. Su, Z. Liu, D. E. Gary, R. B. Barat, Z.-H. Michalopoulou, and J. F. Federici, "Interferometric and synthetic aperture real-time terahertz imaging," presentation at American Physics Society Meeting, (Pittsburgh, PA, March 2009).

K. Su, Z. Liu, L. Moeller, and J. F. Federici, "Data encoding on continuous wave THz signals for sensing," presentation at International Symposium on Spectral Sensing Research, (Hoboken, NJ, June 2008).

K. Su, Z. Liu, D. E. Gary, R. B. Barat, Z.-H. Michalopoulou, and J. F. Federici, "Video-rate terahertz interferometric synthetic aperture imaging," presentation at Eighth New Jersey Universities Homeland Security Research Consortium Symposium, (Princeton, NJ, December 2008).

To my beloved parents, my husband and my son

谨献给我深爱的父母, 丈夫和儿子

ACKNOWLEDGMENT

I would like to express my sincere gratitude to Dr. John Federici, my academic advisor, not only for his extensive knowledge, insight, and guidance in the academic field, but also for his support, encouragement, and personal advice. Special appreciation is given to Dr. Lothar Moeller at Bell Labs Lucent Technologies. As one of my committee members, Dr. Moeller has always been extremely generous with his time, knowledge and ideas to help me with experimental methodology and system setup development.

Appreciation is also extended to Dr. Andrei Sirenko, Dr. Tao Zhou, Dr. Zhen Wu and Dr. Haim Grebel for actively participating in my research and serving in my dissertation committee.

I would like to acknowledge Dr. Barat Robert for numerous conversations and valuable advices for developing the fog and dust chamber. I also thank my friends in the lab and physics department for their help and discussions during my years at NJIT. The staff of physics department was extremely kind and helpful to me, and my work wouldn't have been completed without their help.

This research is supported by the National Science Foundation under Grant No. ECCS-1102222.

Finally, I wish to offer the utmost appreciation to my beloved family: my husband and my little baby boy for their understanding and the sacrifices they have made throughout my study and my parents for their encouragement and endless support in my life.

TABLE OF CONTENTS

Chapter **Page**

1 INTRODUCTION………………………………………………………… 1

1.1 Terahertz Communication Systems………………………………………. 1

1.1.1 THz Time-Domain Systems……………………………………… 5

1.1.2 Photonic MMW/ UTC-PD Opto-Electronics Systems …………... 8

1.1.3 Integrated Circuit Systems………………………………………... 9

1.1.4 Multiplied Microwave Systems…………………………………... 10

1.1.5 Quantum Cascade Laser Systems………………………………… 11

1.2 Infrared Communication Systems………………………………………... 12

1.3 Atmospheric and Free-Space Damping Including Fog, Rain, Dust and Snow on THz and IR links………………………………………………... 15

1.3.1 Basic Definitions………………………………………………….. 15

1.3.1.1 Atmosphere……………………………………………... 15

1.3.1.2 Aerosol………………………………………………….. 16

1.3.1.3 Attenuation……………………………………………... 16

1.3.1.4 Absorption……………………………………………… 16

1.3.1.5 Scattering……………………………………………….. 17

1.3.1.6 Scintillation……………………………………………... 17

1.3.2 Atmospheric Attenuation of THz and IR communication Links… 18

1.3.2.1 Simulations……………………………………………... 18

TABLE OF CONTENTS
(Continued)

Chapter **Page**

1.3.2.2 Experimental Characterization of Environment on THz Communication Links………………………………… 19

1.3.3 Scintillation Effects on the THz and IR Communication Link…... 22

2 EXPERIMENTAL METHODOLOGY………………………………………. 25

2.1 THz CW Photo Mixing Communication System……………………….. 25

2.1.1 Distributed Feedback (DFB) Diode Laser System………………. 27

2.1.1.1 DFB Laser Source……………………………………… 27

2.1.1.2 BoosTA (High Power Semiconductor Optical Amplifiers)…………………………………………….. 28

2.1.1.3 ISCAN (Quadrature Interferometer)………………….. 28

2.1.2 Signal Modulation………………………………………………. 30

2.1.3 THz Generation and Detection………………………………….. 32

2.1.3.1 Theory…………………………………………………. 32

2.1.3.2 Photoconductive Antenna…………………………….. 33

2.2 Frequency Multiplier Chain Based 625 GHz Wireless Communication System……………………………………………………………… 34

2.2.1 THz Source……………………………………………………….. 35

2.2.2 Signal Modulation (Duobinary Modulation)……………………. 36

2.2.3 Transmission Channel…………………………………………… 37

TABLE OF CONTENTS
(Continued)

Chapter **Page**

2.2.4 THz Receiver and Signal Detection…………………………….. 37

2.3 IR Wireless Communication System at 1.5 µm…………………………. 38

2.3.1 Transmitter and Receiver Elements of IR Communication Link… 39

2.3.2 Proportional–Integral–Derivative Controller (PID Controller)….. 41

2.3.2.1 Introduction of PID Topology………………………….. 41

2.3.2.2 PID Controller for the Fog Environment……………… 42

2.3.3 Data Acquisition…………………………………………………. 43

3 PERFORMANCE ANALYSIS AND CHARACTERIZATION OF THE DATA LINKS……………………………………………………………… 44

3.1 Characterization of THz CW Photo Mixing Data Link………………….. 44

3.1.1 Analog Ramp Signal Modulation………………………………… 44

3.1.2 Pseudorandom Bit Sequence (PRBS) Modulation……………… 46

3.1.3 Characterization of THz Tx and Rx by Fast Spectrum Scanning… 47

3.1.4 Limitation of THz CW Photo Mixing Data Link………………… 49

3.1.4.1 THz Tx and Rx Spectrum Limitation………………….. 49

3.1.4.2 Bandwidth Limitation………………………………….. 50

3.1.4.3 Low Signal to Noise Ratio (SNR) and Vibration Effects. 50

3.2 Characterization of Frequency Multiplier Chain Based 625 GHz Wireless Communication Link…………………………………………………….. 51

TABLE OF CONTENTS
(Continued)

Chapter **Page**

3.2.1 Double Balanced Mixer Characteristics………………………. 51

3.2.2 Power Transfer Function Measurement……………………… 52

3.2.3 Performance of Duobinary Modulation Technique…………… 53

3.2.4 Performance Analysis of Detected Signal……………………... 55

3.2.5 Signal-To-Noise Ratio (SNR) Measurement…………………… 57

3.3 Characterization of IR Wireless Communication System at 1.5 µm…….. 58

4 COMPARISON OF PERFORMANCE DEGRADATION FROM TERAHERTZ AND INFRARED WIRELESS LINKS IN FOG…………….. 59

4.1 Fog Introduction……………………………………………………… 60

4.2 Fog Attenuation and Scattering Mechanisms…………………………… 61

4.2.1 Fog Attenuation………………………………………………. 61

4.2.2 Scattering Mechanism…………………………………………… 62

4.3 Scintillation Effects on the THz and IR Communication Link…………... 64

4.4 Millimeter Wave Attenuation Due to Fog………………………………. 67

4.4.1 Double-Debye Model…………………………………………. 67

4.4.2 Simulation Results…………………………………………….. 69

4.5 Infrared Wave Attenuation Due to Fog…………………………………... 71

4.5.1 Full Mie Scattering Calculation: Theoretical Approach………… 71

4.5.1.1 Total Extinction Coefficient…………………………… 71

TABLE OF CONTENTS
(Continued)

Chapter **Page**

4.5.1.2 Particle Size Distribution………………………………. 72

4.5.1.3 Fog Attenuation……………………………………… 72

4.5.2 Empirical Approach……………………………………………. 73

4.5.2.1 Principles of Kruse, Kim and Al Nabulsi Models……… 73

4.5.3 Simulation Results………………………………………………... 75

4.6 Experimental Results…………………………………………………….. 78

4.6.1 Experimental Setup…………………………………………… 78

4.6.2 Experimental Results…………………………………………….. 79

4.6.2.1 Signal Attenuation by Fog……………………………… 79

4.6.2.2 Fog Visibility Characterization………………………… 82

4.6.2.3 Scintillation Effects in Fog Chamber………………….. 83

5 COMPARISON OF PERFORMANCE DEGRADATION FROM TERAHERTZ AND INFRARED WIRELESS LINKS IN DUST……………. 86

5.1 Experimental Methodology………………………………………………. 87

5.1.1 Dust Particle Size Distribution for Bentonite……………………. 87

5.1.2 Dust Chamber Design…………………………………………….. 88

5.1.3 Force Balance Analysis of the Dust Particle……………………... 90

5.1.3.1 The Intermediate Range of Reynolds Numbers………… 93

5.1.3.2 Is Newton's Regime Appropriate?................................ 94

TABLE OF CONTENTS
(Continued)

Chapter **Page**

5.1.3.3 Is the Reynolds Number in the Stoke's Regime?............ 94

5.1.3.4 Volumetric Flow Rate Calculation…………………….. 95

5.1.4 Experiment Setup……………………………………………… 95

5.2 Mie Scattering Theory………………………………………………. 96

5.3 Experimental Results……………………………………………….. 98

5.3.1 0.05 g of Dust……………………………………………….. 98

5.3.1.1 Transmission Link Performance with Disabled PID Controller……………………………………………. 98

5.3.1.2 Scintillation Effects study with PID Controller………… 101

5.3.2 0.08 g of Dust…………………………………………….......... 104

5.3.2.1 Transmission Link Performance with Disabled PID Controller……………………………………………. 104

5.3.2.2 Scintillation Effects Study with PID Controller……….. 106

5.3.3 Comparison of Different Dust Densities…………………………. 107

5.4 Simulation Results…………………………………………………... 109

6 CONCLUSIONS AND FUTURE PERSPECTIVES…………………………... 115

6.1 Summary of Research Results…………………………………………. 115

6.2 Future Work……………………………………………………………. 117

LIST OF TABLES

Table **Page**

1.1 Summary of THz Communication Link Measurements 4

1.2 Division of Infrared Radiation by International Organization for Standardization (ISO)……………………………………………………….…………………….. 13

4.1 Typical Fog Droplets with Radius, and Corresponding Size Parameter for Wavelengths of 480 µm and 1.5 µm....………………………………………….... 63

4.2 Double-Debye Model Predication of Attenuation for Frequency Up to 1000 GHz, Water Content: $w=1g/m^3$ ……………....……………………………… 69

4.3 DSD Gamma Parameters, Reflectivity Z, LWC and Visibility V of the Considered Four Models of the Fog...…………………….................................. 72

4.4 Comparison of THz Experimental and Theoretical Specific Attenuation at Different Visibility ………………………………………………………………. 83

5.1 Bentonite Particle Size Distribution Parameter …..….....……………………….. 87

5.2 Reynolds Numbers for Different Regimes………………………………………. 93

LIST OF FIGURES

Figure **Page**

1.1 The electromagnetic spectrum...…….....................………………………. 1

1.2 Experimental setup for analog THz communication link using and external THz modulator ………………………………………………………………….... 5

1.3 THz communication set-up based on THz TDS system…………………………. 6

1.4 (a)-(c) Eye diagrams at different data rate and error-free operation, (d) at 1.5 Mb/s with BER=10^{-4}, (e) measured and simulated required TVS at different data rates…………………………………………………………………………. 8

1.5 Microwave frequency multiplier (a) THz source (b) THz receiver……………... 10

1.6 Schematic of link showing quantum cascade laser at left and quantum well photodetector on right………………………………………………………… 12

1.7 Calculated atmospheric attenuation in THz and IR band………………………... 18

1.8 Comparison of attenuation coefficient between calculation and measurements at 103 GHz for a 1 minute integration time……………………………………… 20

1.9 Measured BER for 120GHz wireless link (10.3Gb/s data rate) versus rain attenuation…………………………………………………………………….. 21

1.10 Comparison between calculation and measurements at 355.2 GHz for a 1 minute integration time………………………………………………………............. 21

1.11 Air turbulence causes refractive index fluctuations resulting into speckle (intensity variations at receiver) that limits the reach of IR systems…………….. 23

2.1 Schematic diagram for THz CW photo mixing communication system (a) laser system (b) optical system (c) signal modulation and detection (d) THz Tx and Rx ……………………………………………………………………………... 26

2.2 Quadrature interferometer (ISCAN)…………………………………………... 29

2.3 Quadrature signal and corresponding mode signatures………………………….. 30

LIST OF FIGURES
(Continued)

Figure **Page**

2.4 Electro-optic phase modulator ………………………………………………….. 31

2.5 Terahertz generation Laser-gated photoconductive antenna Vbias: Bias voltage applied to the gallium-arsenide (GaAs) substrate ……………………………….. 34

2.6 Schematic of up converting frequency multiplier chain based 625 GHz transmission link ………………………………………………………………... 35

2.7 (a) Schematic diagram of IR wireless communication link, (b) IR source, (c) IR receiver and signal detection …………………………………………………… 39

2.8 The block diagram of PID controller…………………………………………. 41

3.1 THz detector voltage output versus time as a function of modulated phase. The sawtooth waveforms (left column) illustrate the modulated voltage (modulation rate is 100 kHz). Middle column and left column are simulated detector signals and experimental detector output, respectively. (a) Phase modulation is 5 radian (smaller than 2π), corresponding modulation voltage is 290V (b) Phase modulation is 2π, corresponding modulation voltage is 360V (c) Phase modulation is 8 radian (larger than 2π), corresponding modulation voltage is 460V…………………………………………………………………………… 45

3.2 Eye diagrams at different data rates (a) data rate:150kb/s (b) data rate: 200kb/s (c) data rate:400kb/s (b) data rate: 500kb/s. …………………………………….. 47

3.3 Rapid frequency tuning curves for the measured THz (a) 1 THz scanning range with 1 GHz step (b) Unit in logarithmic scale with 1 GHz step (c) 30 GHz to 130 GHz scanning range with 100MHz step……………………………………. 48

3.4 (a) THz detector voltage output versus time as a function of modulated phase. (modulation rate is 100 kHz, THz carrier wave frequency: 91GHz). CH1: the sawtooth waveform (modulation function) CH2: detected signal from THz Rx. (b) noise level……………………………………………………………….. 50

3.5 Double balanced mixer characteristics…………………………………………... 51

3.6 Power transfer function of system and spectrum of data signal at THz source input………………………………………………………………………… 53

LIST OF FIGURES
(Continued)

Figure **Page**

3.7 Eye diagrams at 100 ps/div (a) output PPG, (b) output add & delay filter, (c) after low pass filter (LPF1), (d) input to THz source (carrier @12.5 GHz), (e) output RX LPF, and (f) corresponding signal spectra…………………………… 54

3.8 Bit error curves for long and short PRBSs with and without decision threshold optimization. Eye diagram at decision gate input……………………………….. 57

3.9 IR BER curves for long and short PRBSs with fixed decision threshold optimized at $BER=10^{-6}$ ……………………………………………………. 58

4.1 (a) Size parameter distribution of fog particles for wavelength of 480 *um* (625 GHz) and 1.5 *um* and the corresponding regions for Rayleigh, Mie, and non-selective or geometrical scattering…………………………………………….. 63

4.1 (b) Isotropic scattering (Rayleigh scattering) and forward scattering (Mie scattering)………………………………………………………………… 64

4.2 Air turbulence causes refractive index fluctuations resulting into speckle (intensity variations at receiver) that limits the reach of IR systems…………….. 65

4.3 (a) Double-Debye model predication of attenuation for frequency up to 1000 GHz, water content: $w=1g/m^3$ and temperature from -20 ℃ to +20 ℃ (b) Logarithmic scale…………………………………………………………… 70

4.4 (a) Extinction coefficients versus wavelength for advection fog and various visibility values as derived from FASCOD (b) Extinction coefficients vs wavelength for radiation fog and various visibility values as derived from FASCOD…………………………………………………………………… 73

4.5 Specific attenuation using Kruse model for 1550 nm wavelength………………. 76

4.6 Specific attenuation using Kim model for 1550 nm wavelength………………… 76

4.7 Specific attenuation using Al Nabulsi model for 1550 nm wavelength…………. 77

4.8 Specific attenuation for 1550 nm wavelength predicted by different models…… 77

4.9 Specific attenuation versus wavelength for various visibility values derived from Kim model…………………………………………………………….. 78

LIST OF FIGURES
(Continued)

Figure **Page**

4.10 (a) Schematic diagram of THz and IR wireless communication link through fog chamber, (b) IR source, (c) IR receiver and signal detection…………………… 79

4.11 (a) Attenuation of THz link and IR link with time (b) Log(BER) of THz link and IR link with time (c) IR attenuation in dB relative to THz attenuation in dB over time……………………………………………………………………. 81

4.12 Specific Attenuation of THz link and IR link with time (dB/km)……………….. 82

4.13 Infrared visibility with time calculated by Kim model …………………………. 82

4.14 (a) Individiually normalized outputs of photodetectors(PD1, PD2, PD3) in dB, b) Opitcal power of IR and RF power of THz due to fog, c) Log(BER) of IR and THz links impaired by fog…………………………………………………….. 85

5.1 Particle size distribution of Bentonite measured by laser diffraction particle size analyzer……………………………………………………………………... 87

5.2 (a) Schematic diagram of dust chamber design (b) real picture of dust chamber design……………………………………………………………………. 89

5.3 Free body diagram of the dust particle………………………………………... 90

5.4 (a) Schematic diagram of THz and IR wireless communication link through dust chamber, (b) IR source, (c) IR receiver and signal detection…………………… 96

5.5 (a) Predicted IR attenuation due to spherical airborne particles, (b) Predicted THz attenuation due to spherical airborne particles…………………………… 98

5.6 Detected IR signal for the 0.05gram dust (a) Free Space (PD-2) (b) SM Fiber Detector (PD-3) (c) Optical Power of IR(dBm), (d) Log(BER) of IR…………... 99

5.7 (a) Attenuation of THz link and IR link with time (b) Log(BER) of THz link and IR link with time…………………………………………………….. 100

5.8 Detected IR signal with single mode fiber detector and free space detector for the source caused vibration……………………………………………………. 101

LIST OF FIGURES
(Continued)

Figure **Page**

5.9 (a) Individually normalized outputs of photodetector(PD-1, PD-2, PD-3) in dB, (b) opitcal power of IR and RF power of THz due to dust, (c) Log(BER) of IR and THz links impaired by dust………………………………………………. 103

5.10 Detected IR signal for the 0.08gram dust (a) Free Space (PD-2) (b) SM Fiber Detector (PD-3) (c) Optical Power of IR(dBm), (d) Log(BER) of IR………….. 104

5.11 (a) Attenuation of THz link and IR link with time (0.08gram) (b) Log(BER) of THz link and IR link with time……………………………………………….. 105

5.12 (a) Individually normalized outputs of photodetector (PD1, PD2, PD3) (b) outputs of the photodetector with noise elimination…………………………….. 106

5.13 (a) Normalized voltage detected by free space detector (PD-2) for different amount of the dust (b) Optical power of IR for different amounts of dust (c) Log(BER) of IR for different amounts of dust ………………………………….. 107

5.14 (a) Attenuation for different amount of the dust (b) Log(BER) of THz for different amounts of dust…………………………………………………………… 109

5.15 (a) The extinction efficiency as a function of size parameter. (b) The extinction efficiency as a function of frequency. (c) The relationship between parameter size and frequency…………………………………………………………….. 111

5.16 The particle density with time…………………………………………………… 113

5.17 Comparison of experimental results and simulation results of THz attenuation ……………………………………………………………………. 114

CHAPTER 1

INTRODUCTION

In this chapter, basic background information of Terahertz (THz) technology and Infrared (IR) technology are introduced. Then ongoing research on the development of experimental THz communication links and IR communication links is reviewed. Finally, scintillation effects and atmospheric and weather impacts (dust, fog, rain) on the THz and IR communication are discussed and compared.

1.1 Terahertz Communication Systems

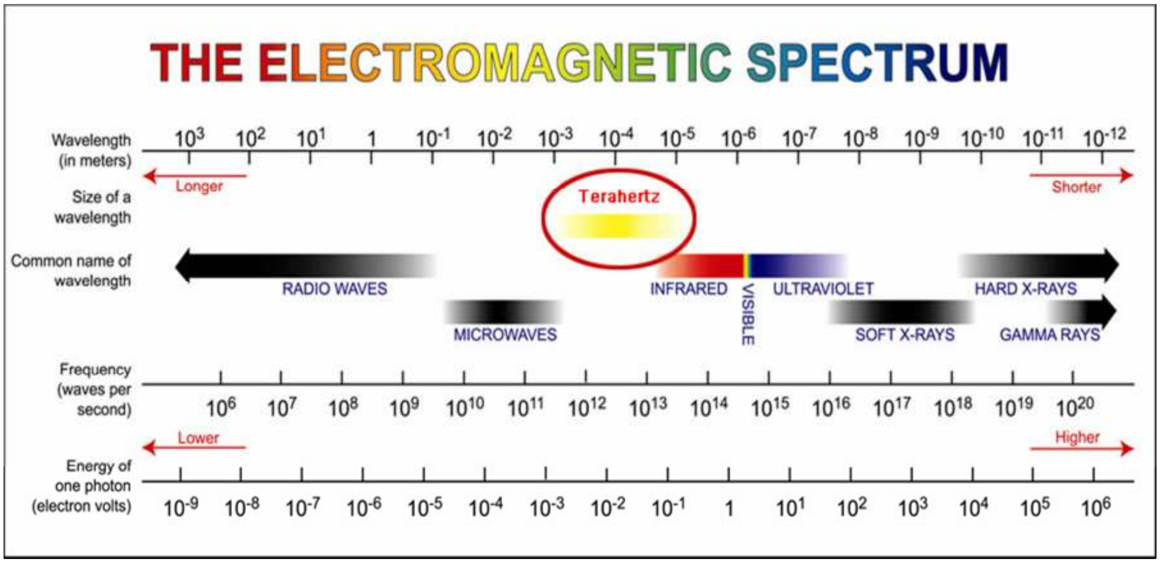

Figure 1.1 The electromagnetic spectrum.

The terahertz region of the electromagnetic spectrum, located in the gap between the microwave and infrared, is typically defined as the frequency range from 0.1 THz to 10 THz, which corresponds to the free-space wavelength from 3 millimeter (mm) to 30 micrometers (µm) (as shown in Figure 1.1). This region is also called the “THz gap”.

It is bridging the gap between the electronic and photonic response. Below the THz range (microwaves), electronic components are commercially available. In the frequency range higher than THz (optical and infrared waves), high efficient thermal sources and commercial thermal cameras (detectors) are available and optical techniques are applicable. However, within the THz range, neither optical nor electronics devices could fully meet the application requirements. It lacks suitable components such as convenient and inexpensive sources, sensitive detectors, and high speed modulators.

Over the past few years, the field of terahertz science and technology has changed dramatically. Many new advances in the technology of THz sources and detectors [1-3] have revolutionized the field. Many applications for THz systems has been introduced in the literature, ranging from explosive and concealed weapon detection [4-6], biology imaging [7, 8], nondestructive testing and quality [9, 10] control to next generation wireless communication systems. Here, the focus is on describing approaches to wireless THz communication.

Edholm’s law of bandwidth [11] predicts the need of data rates around 5-10 Gb/s in 10-15 years from now. The increasing demand for higher data rates suggests the development of wireless communication networks at higher carrier frequencies. Consequently, one can expect that such systems will soon push towards to the low THz frequency range due to its inherently larger accessible bandwidth compared to microwave and millimeter communication bands [12]. A review by Koch [13] in 2007 predicts that Wireless LAN systems will be replaced or supplemented by the THz based communication systems in 2017-2023.

Compared to microwave or millimeter wave systems, THz wireless communication link offers some advantages. The summary is as follows:

- Ultra-high bandwidth: THz communications have the potential for increased bandwidth capacity compared to microwave systems.
- Unregulated frequencies: Frequencies above 300 GHz are currently unallocated by the Federal Frequency Allocation Commission (FCC) and offer very high bandwidth.
- Directional beam: THz communications are inherently more directional than microwave or millimeter (MMW) links since THz waves have less free-space diffraction. The link budget analysis [15] suggested at the same antenna aperture with the microwave, transmission for the 350 GHz require a large gain per antenna, which requires THz emission to be highly directional and therefore, line of sight detection is required.
- High security: THz communication can be implemented as a “secure” communication link [16]. THz can support ultrahigh bandwidth spread spectrum systems, which can enable secure communication, large capacity networks, and protection against channel jamming attacks.

Towards higher carrier competing frequencies (IR), THz also shows some advantages, such as:

- Lower attenuation of THz radiation compared to IR under certain weather conditions (fog and dust).
- Scintillation effects of THz radiation are smaller than IR radiation which allows THz to provide longer links compared to wireless IR link.
- There is more ambient IR light noise typically present compared to ambient THz noise.
- There is an eye safety with IR wavelengths requiring that IR transmitted power be limited to eye-safe power levels, however, THz is safe for human health with available commercial source power.

In this following part, the recent developments of ultrahigh-speed wireless communication links using carrier frequencies of over 100 GHz will be reviewed (as shown in Table 1.1).

Table 1.1 Summary of THz Communication Link Measurements. BER Stands for Bit-Error-Rate. PDA Stands for Photoconductive Antenna. MZM Stands for Mach-Zender Modulator. PRBS Stands for Pseudo Random Bit Sequence. UTC-PD Stands for Uni-Traveling Carrier Photodetector. ASK Stands for Amplitude-Shift Keying. NRC Stands for Non-Return-to-Zero. MMIC Stands for Millimeter Wave Integrated Circuits

THz system	THz carrier frequency (GHz)	Modulation hardware	Maximum distance (m)	Modulation method	Modulation rate or bandwidth	BER	Reference
THz time-domain system	300	External modulator	0.48	Analog	6 kHz		[17]
	300	PDA	1	Analog	5 Kb/s		[18]
	300	PDA	1	Digital (PRBS)	1 MHz	10^{-8}	[19]
Opto-electronic /UTC-PD	120	Optical MZM modulator	100	Digital (PRBS)	10 Gb/s	10^{-10}	[20]
	120	Optical MZM modulator	250 450	Digital (ASK)	3 Gb/s	10^{-10}	[21, 22]
	200	Optical MZM modulator	2.6	Digital (NRZ)	1.0625 Gb/s	10^{-9}	[23]
	250	Optical modulator	0.5	Digital (ASK)	8 Gb/s	10^{-10}	[24, 25]
	300-400	Optical modulator	0.5	Digital (ASK)	2 Gb/t, 12.5 Gb/t	10^{-12}	[26, 27]
Millimeter wave integrated circuit	120	MMIC	800	Digital (ASK)	10 Gb/s	10^{-12}	[28]
	120	MMIC	5800	Digital (ASK)	10 Gb/s	10^{-12}	[29]
Microwave multiplication	300	Sub harmonic mixer	22	Analog	6 MHz		[30]
	300	Sub harmonic mixer	52	Digital video broadcasting	96 Mb/s	$\sim 10^{-8}$ at 30cm	[31]
	625	Microwave mixer	1	Duobinary/ PRBS	2.5 Gb/s	10^{-10}	[32]
Quantum cascade laser (QCL)	3800	Electronic modulation of QCL	2	Quantum cascade laser	10 kHz		[33, 34]

Source: [16, 35]

1.1.1 THz Time-Domain Systems (TDS)

The first three THz wireless communication links in the Table 1.1 are all based on THz time-domain systems. All three structures have some common characteristics: (a) photoconductive antenna (PDA) structures are all utilized as the THz transmitter and receivers (b) transmission center frequency is roughly 0.3 THz (c) The maximum data rate is limited by the repetition rate of the Ti: Sapphire Laser (typically ~80 MHz) and electronic bandwidth of the PDA (~1 MHz) (d) To detect the maximum THz signal at the peak of THz pulse, the transmitter to receiver distance ant timing of the gating pulsed need to be adjusted. Consequently, timing jitter of the laser or variations in the optical path length degrades the quality of the link.

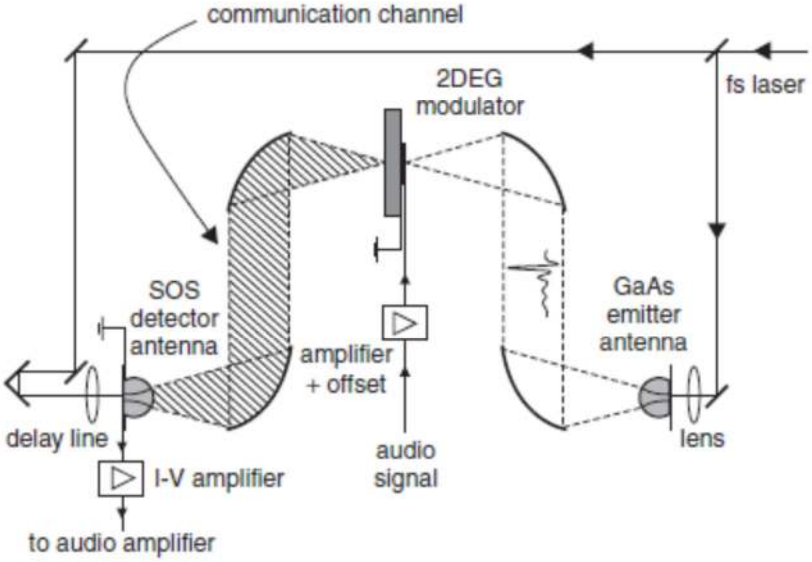

Figure 1.2 Experimental setup for analog THz communication link using an external THz modulator.
Source: [17]

Kleine-Ostmann et al. [17] first demonstrated the transmission of an audio signal through THz communication links which utilized a modified THz time-domain system and an external modulator based on the depletion of a two-dimensional electron gas (shown in Figure 1.2). The audio signals up to 25 kHz could be transmitted through a 0.48 m distance. The bandwidth of the THz detection was limited by the time-constant of the lock-in and 7 kHz cutoff frequency of the I-V amplifier.

Another analog THz link based on THz time-domain system was demonstrated by Liu et al. [18]. The audio signals were modulated upon the THz carrier by directly modulating the bias voltage of the THz receiver. The transmission distance is about 100 cm. The 3 dB frequency response of the transmission channel was about 20 kHz. To demonstrate the fidelity of data transmission, music was transmitted through the data channel by using the electronic output from a computer's speaker to modulate the electronic bias to the THz transmitter. In frequency domain, good fidelity of data transmission up to ~2 kHz could be observed.

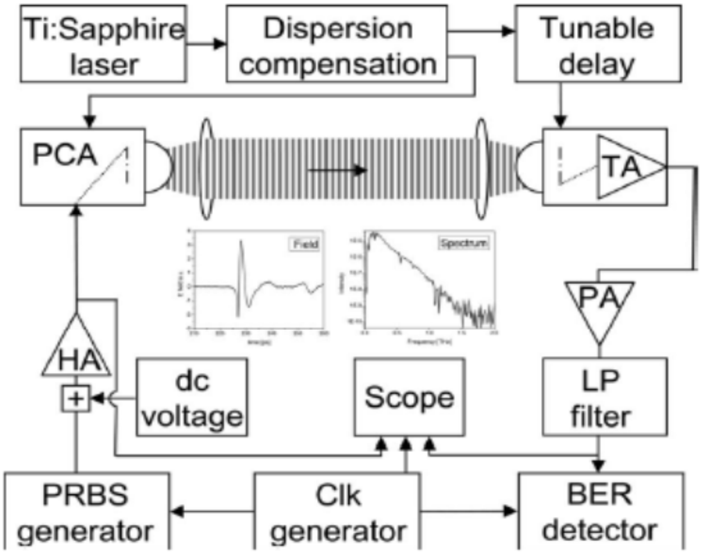

Figure 1.3 THz communication set-up based on THz TDS system. HA: high-voltage amplifier, PCS: photoconductive switch, TA: transimpedance amplifier, PA: preamplifier, LP: low pass, CLK: clock tone.
Source:[19]

Moeller et al. [19] demonstrated bipolar and on/off keying of THz pulses with maximum modulation index by direct digital data encoding of photoconductive emitter antenna' bias voltage, thereby enabling data rates almost three orders of magnitude higher than described in the previous two communication system[17, 18]. The experimental set-up is shown in Figure 1.3, which consists mainly of a commercially available THz TDS system which is electrically connected to a data source and BER tester. The emitter antenna is electrically driven by a digital signal carrying the data instead of a constant bias. A dc-coupled amplifier can increase the voltage at the antenna input to about 20 V. A dc-offset between 0 V and ±Vpp/2 can be added to the pattern generator output, allowing the signal format to vary continuously between bipolar and on/off modulation. As the electrical field of the THz pulse directly depends on the sign and the amount of the applied antenna bias, the pseudo random binary sequence (PRBS) data are linearly mapped onto the THz signal and form its envelope.

As shown in Figure 1.4, at error-free operation (bit error rate (BER)<10^{-8}), a high impedance sampling scope recorded 0.5 Mb/s, 1 Mb/s, and 1.5 Mb/s eye diagrams, showing the data-rate dependent ISI caused by limited receiver bandwidth. At low transmitter voltage swing (TVS), receiver noise (Figure 1.4 d) limits the BER=10^{-4}, which is manageable using forward error correcting codes. At this BER level the minimal required TVS for different data rates is determined to quantify ISI (intersymbol interference) caused performance degradations (Figure 1.4 e). A comparison with a 2nd order low pass (LP) filter simulations of the receiver shows good agreement with the measurement. Increasing the TVS widens the eye which results into a reduced BER. Tests showed that long (2^{23}-1) and short (2^{7}-1) PRBSs yield same BER performance.

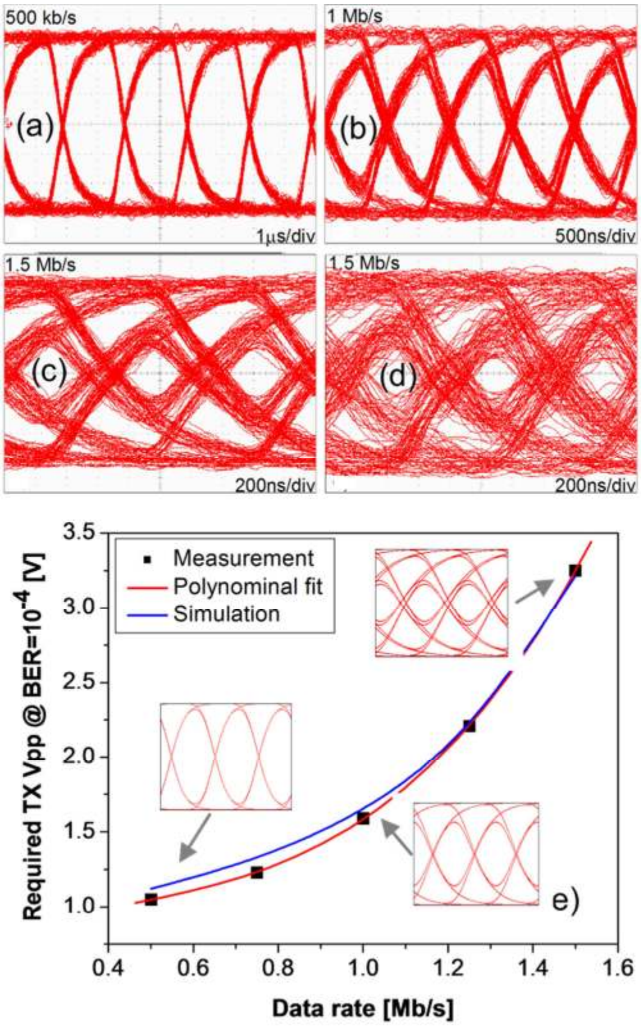

Figure 1.4 (a)-(c) Eye diagrams at different data rate and error-free operation, (d) at 1.5 Mb/s with BER=10^{-4}, (e) measured and simulated required TVS at different data rates. Source:[19]

1.1.2 Photonic MMW/UTC-PD Opto-Electronics Systems

Over the years, Nippon Telegraph and Telephone Corporation (NTT) group in Japan has achieved substantial innovations in hardware components and several sub-THz communication links which have been developed [26]. There are three types of systems listed in Table 1.1.

- Photonic MMW/UTC-PD THz sources and Schottky diode detector [20].

- Photonic MMW/UTC-PD THz sources and MMIC receivers [21].
- An integrated MMIC transmitter and receiver [28].

The first two are radio-over-fiber (RoF) systems, which refer to modulating optical carrier signals at millimeter wave frequencies. The optical signals can be routed to a THz transmitter module using low loss optical fibers. Within the THz transmitter module, the modulated optical beam is converted to a THz signal using a uni-traveling carrier photodiode (UTC-PD) and launched into free space using a feed horn. The motivations and advantages of the ROF system are several folds, listed as followed:

- A RoF system could be an attractive solution to line of sight requirement limitation because the millimeter signals can be transmitted over long distances by using optical fibers with an optical frequency comb.
- A RoF system can easily be integrated into a high-speed optical fiber communication link as part of a first mile and last mile solution.

1.1.3 Integrated Circuit Systems

While the 1.5μm fiber-optical components of the RoF systems enable easy integration with high-speed optical communications systems, there is a drawback of the photonic approach in terms of additional optical components, system size, total cost, and added power consumption. Clearly, replacing the opto-electronic THz source with an integrated electronic device - which could function in concert with the Monolithic Microwave Integrated Circuit (MMIC) receiver chip – would eliminate many of these issues. Yamaguchi et al. [28] implemented a flexible coplanar waveguide MMIC chipset [36], which included amplifiers, modulators, and demodulators, as the THz transmitter and receiver in a 10 Gb/s wireless link. The link exhibited a 10^{-12} BER of a 10 Gb/s signal over 800 m distance [28]. Improvements to the 120 GHz transmitter and well as implementation of forward error correction algorithms have extended the link distance to 5.8 km with an error-free transmission of 10 Gb/s data [29].

1.1.4 Multiplied Microwave Systems

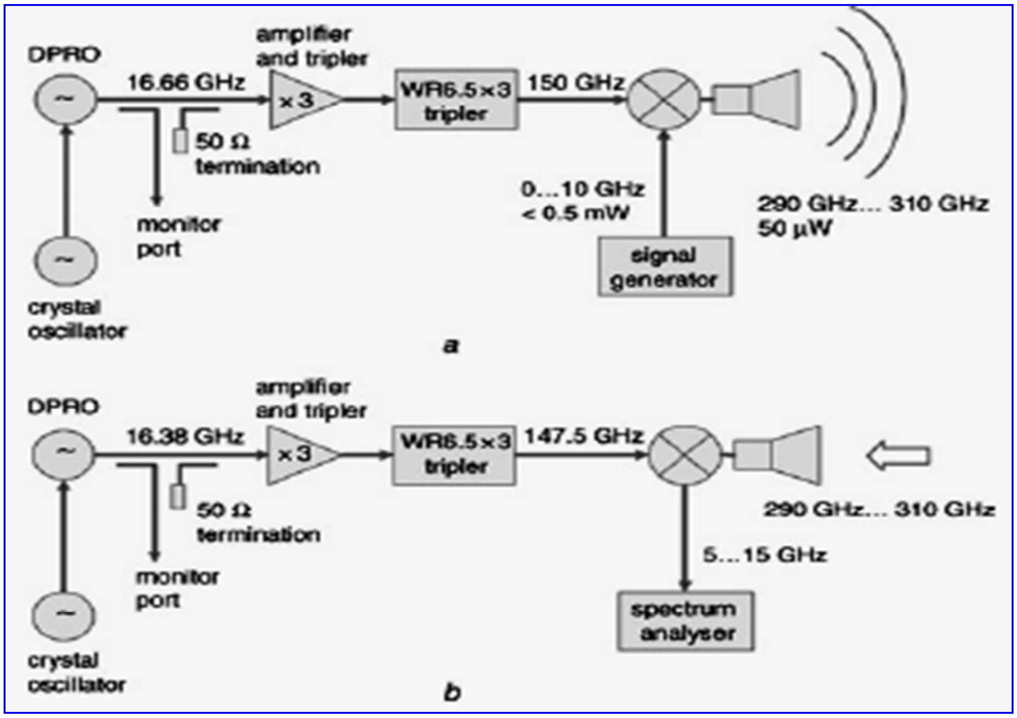

Figure 1.5 Microwave frequency multiplier (a) THz source (b) THz receiver.
Source: [30]

Jastrow et al. demonstrated the analog [30] and digital [31] video signal transmission at 300 GHz using a microwave multiplier system. As shown in Figure 1.5, the system consists of a frequency multiplied (6X) 16.66 GHz local oscillator (LO). The resulting 150 GHz signal is converted to a 290-310 GHz signal using a sub-harmonic mixer and a DC-10GHz signal generator. The receiver LO is 16.38 GHz so that the intermediate frequency (IF) of the receiver (5 GHz) is detected using heterodyne detection.

To demonstrate data transmission, Jastrow et al. transmit a color video baseband signal with 6 MHz bandwidth which is modulated on an ultrahigh frequency (UHF) carrier (855.25MHz) and then acts as the “signal generator” to be transmitted over THz link. At the receiver, the 5 GHz intermediate frequency (IF) is mixed down to baseband and fed to a standard TV card. The TV card input requires a minimum signal to noise of ratio of 40 dB. The image quality if viewed on computer screen. Using just the THz feed horns, excellent picture quality is reported up to 0.5 m with significant degradation observable at transmission distances of 0.8 m. When lenses are used to collimate the THz radiation, a maximum link distance of 22 m is achieved. The system [30] has been used for digital transmission [31], which is capable of transmitting digital video broadcast (DVB) data at a rate of 96 MB/s over a distance of 52 m using forward error correction codes. A multiplied microwave source for THz communication experiments at 625 GHz has been recently reported [32]. Power, bit-error rate (BER), and signal-to-noise ratio (SNR) measurements on the receiver side describe the signal performance of a 625 GHz link with duobinary format driving THz source. The structure and the experimental results will be described in detail in Chapter 2 and Chapter 3.

1.1.5 Quantum Cascade Laser Systems

Grant et al. developed the quantum cascade laser (QCL) THz free space communication system consisted of a 3.8 THz QCL laser in conjunction with a cryogenically cooled (12K) quantum well photodetector [34]. Figure 1.6 is schematic of the link. At the left a quantum cascade laser housed in a vacuum Dewar provides 3.8 THz radiation which is collected and collimated by a parabolic mirror labeled M1. M1 is a 50 mm focal length off-axis parabolic reflector while M2 is 76 mm focal length. After reflected by M2, Terahertz radiation is coupled through the semi-insulating substrate to the mesa at 45° angle as is done in quantum well infrared photodetector (QWIP).

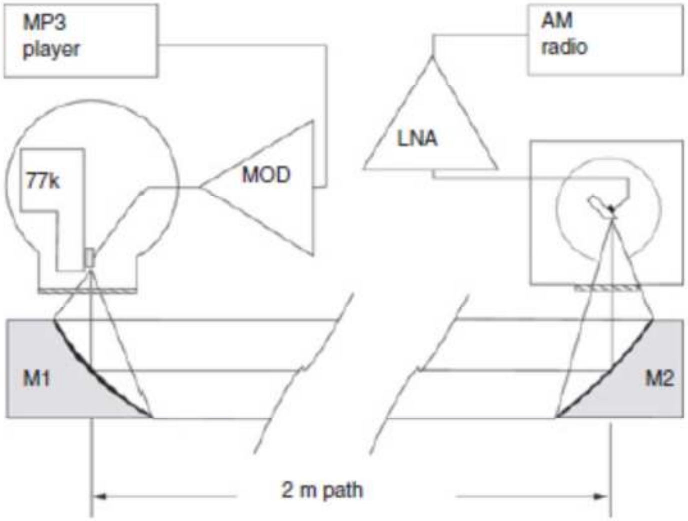

Figure 1.6 Schematic of link showing quantum cascade laser at left and quantum well photodetector on right.
Source: [34]

Analog audio data was transmitted over 2 m path length. Under normal operation, a custom-made pulse generator generated 8ns pulses at a repetition rate of 455 kHz. On top of this constant modulation, an audio frequency modulation is applied. The resulting combined signal electronically modulates the QCL. The quantum well photodetector is sufficiently fast enough to measure the 455 kHz pulse repetition rate as well as the side-bands generated by the audio modulation. The electronic output of the photo-detector is amplified and passed through a 10 kHz low pass filter. Finally, the signal is passed to the antenna input of an AM radio to recover the audio signal. No information or metrics were presented as to the recovered audio signal quality.

1.2 Infrared (IR) Communication Systems

The infrared radiation is the region of electromagnetic spectrum between the THz and visible light, which is in the frequency range from 100 THz to 430 THz, and the corresponding wavelength range from 0.7 µm to 1000 µm. The whole infrared band can be further divided to three sub-regions: the near infrared region (0.7-3) µm, middle infrared region (3-50) µm and far infrared region (50-1000) µm (shown in Table 1.2).

Table 1.2 Division of Infrared Radiation by International Organization for Standardization (ISO)

Designation	Wavelength	Frequency
Near Infrared (NIR)	0.7-3 µm	100 THz-430 THz
Mid Infrared (MIR)	3-50 µm	6 THz-100 THz
Far Infrared (FIR)	50-1000 µm	300 GHz-6 THz

There are many applications IR technology at this time such as infrared imaging [37, 38], tracking [39], heating [40], spectroscope [38] and wireless communications etc. Here, the focus is on describing approaches to wireless IR communications. Wireless infrared communications refers to the use of free space propagation of light waves in the near infrared band as a carrier for communication [41]. The primary applications for wireless infrared communications are listed as follows:

- Short-term cable-less connectivity of information change between two users, such as business cards, file sharing.
- Wireless local area network (WLANs).
- Wireless input and control devices, such as wireless mouse, remote controls, remote electronic keys.

Infrared technology offers several important advantages over radio as a form of wireless communication.

- Potentially huge bandwidths.
- Low cost, small size (portable) and low power requirements (ideal for laptops, telephones and personal digital assistants).
- Simple circuitry: no special or proprietary hardware is required. It can be incorporated into the integrated circuit of a product.

- Higher security: This signal confinement over short distance makes it easy to secure transmissions against casual eavesdropping.
- Immunity to electromagnetic interference (EMI): IR does not interfere with signals from other devices.
- Portable.

However, despite the advantages presented by the infrared medium, IR also shows some drawbacks:

- Line of sight: transmitters and receivers must be almost directly aligned (able to see each other) to communicate.
- Blocked from persons and objects. Communication from one room to another requires the installation of infrared access points that are interconnected via a wired backbone.
- Short range: performance drops off with longer distances.
- Light, weather sensitive: high attenuation when transmitted through air and atmosphere phenomena such as direct sunlight, rain, fog, dust, pollution. THz transmission could offer an effective alternative in this environment.
- Eye safety: IR has eye safety issue which causes the power limitation.

IR free space communication links at 1.5 μm wavelength are the most common optical transmission for short reach (up to 10 km). As previously noted by Koch, wireless IR systems are 30 years old, yet until recently the highest data rates reported were 155 Mb/s for the indoor systems (for diffuse configurations) [14]. The author demonstrated 155 Mb/s wireless transmissions with electronic position detection and tracking of the transmitter at an imaging infrared receiver over a distance of nearly 2 m. A 2007 review [42] of the field in IR shows no improvement beyond the 155 Mb/s data rate reported in 2001. Only recently has a 10 Gb/s data rate been demonstrated in a simulated atmospheric environment [42]. The key to increasing the IR wireless data rate to 10 Gb/s was advanced modulation formats such as orthogonal frequency division multiplexing.

For outdoor systems, optical wireless links have been demonstrated for distances of more than 25 miles and up to 40 Gb/s [43, 44].

When IR is used for outdoor systems, two of the most important issues with IR free-space communications are transceiver misalignment due to atmospheric turbulence and/or humidity fluctuations in the beam path (scintillation) as well as atmospheric absorbance of the IR signal [45]. Atmospheric turbulence and humidity fluctuations cause temporally and spatially dependence variations in the atmospheric real refractive index. Consequently, the location of the IR beam on the receiver tends to vary in time leading to scintillation effects. One of the solutions proposed is use of backup links, such as THz communication links.

1.3 Atmospheric and Free-Space Damping Including Fog, Rain, Dust and Snow on THz and IR links

When THz and IR links are used for outdoor communications, the adverse atmospheric conditions, such as fog, rain, dust and snow will affect the performance of transmission links to different degrees. In this section, the basic definitions will be introduced and experimental characterization of environment on THz and IR communication links will be discussed and compared.

1.3.1 Basic Definitions

1.3.1.1 Atmosphere. Atmosphere is defined as the gaseous mass or envelope surrounding the Earth, which is primarily composed of nitrogen (N_2, 78%), oxygen (O_2, 21%), and argon (Ar,1%), but there are also a number of other elements such as water (

H_2O, 0% to 7%) and carbon dioxide (CO_2, 0.01% to 1%), present in smaller amounts. There are also small particles that contribute to the composition of the atmosphere, such as particles generated by combustion, dust, debris, and soil. The combination of all the elements comprising the atmosphere contributes to its absorption and its behavior.

1.3.1.2 Aerosol. An aerosol is a suspension of solid or liquid particles such as haze particles, clouds, and fog in a gaseous medium with the size range commonly between 0.01 and 10 μm in the radius. The incoming light can be absorbed and scattered by aerosol suspended droplets or particles. The fog droplets are the most important atmospheric elements that contribute to the attenuation of an optical signal through Mie scattering. The loss of light by scattering increases the atmospheric extinction, which is the sum of actual absorption and scattering. The concentration of aerosol particles is high close to the earth's surface and low at high altitudes.

1.3.1.3 Attenuation. Atmospheric attenuation is defined as the process whereby some or all of the energy of an electromagnetic wave is lost (absorbed or/and scattered) when traversing the atmosphere [46]. For the typical wavelengths employed by wireless IR links (850 nm, 1550 nm), the attenuation contribution from the atmosphere is relatively low compared to the attenuation contribution from weather conditions. Gebhart et al. [47] mention that attenuation values are around 0.2 dB/km for clear atmospheric conditions, and 10 dB/km in urban regions (due to dust). Attenuation due to heavy fog, on the other hand, can reach values greater than 300 dB/km.

1.3.1.4 Absorption. Absorption is the process of conversion of the energy of a photon to internal energy, when electromagnetic radiation is captured by matter. When particles in the atmosphere absorb light, this absorption provokes a transition (or excitation) in the particle's molecules from a lower energy level to a higher one. In the context of optical wireless communications, the absorption peak refers to the specific wavelength at which most power is absorbed by a particular impurity in a specific medium. The atmospheric absorption is wavelength dependent and the atmospheric windows due to absorption are created by atmospheric gas.

1.3.1.5 Scattering. Scattering is defined as the dispersal of a beam of particles or of radiation into a range of directions as a result of physical interactions. When a particle intercepts an electromagnetic wave, part of wave's energy is removed by the particle and re-radiated into a solid angle centered at it. The details of the scattering principle will be introduced in Chapter 4.

1.3.1.6 Scintillation. With regard to communications, scintillation is defined as a random fluctuation on the received field strength caused by irregular changes in the transmission path over time [46]. In the specific case of optical wireless communications, this term refers to the strength variation of an optical signal as it travels through air, and it derives from small fluctuations (optical turbulence) in the index of refraction along the optical path. After fog, low clouds, and direct sunlight, scintillation is the factor that causes most significant performance deterioration of an optical wireless links. Scintillation effect can accumulate over a few kilometers of propagation distance. Scintillation also appears to be more significant when the receiver has a small aperture [48].

1.3.2 Atmospheric Attenuation of THz and IR Communication Links

1.3.2.1 Simulations. Atmospheric attenuation of THz and IR communications are impacted differently by weather conditions such as fog, rain, snow, and humidity. Figure 1.7 compares the atmosphere attenuation of millimeter waves, THz and IR waves at sea level for different weather conditions.

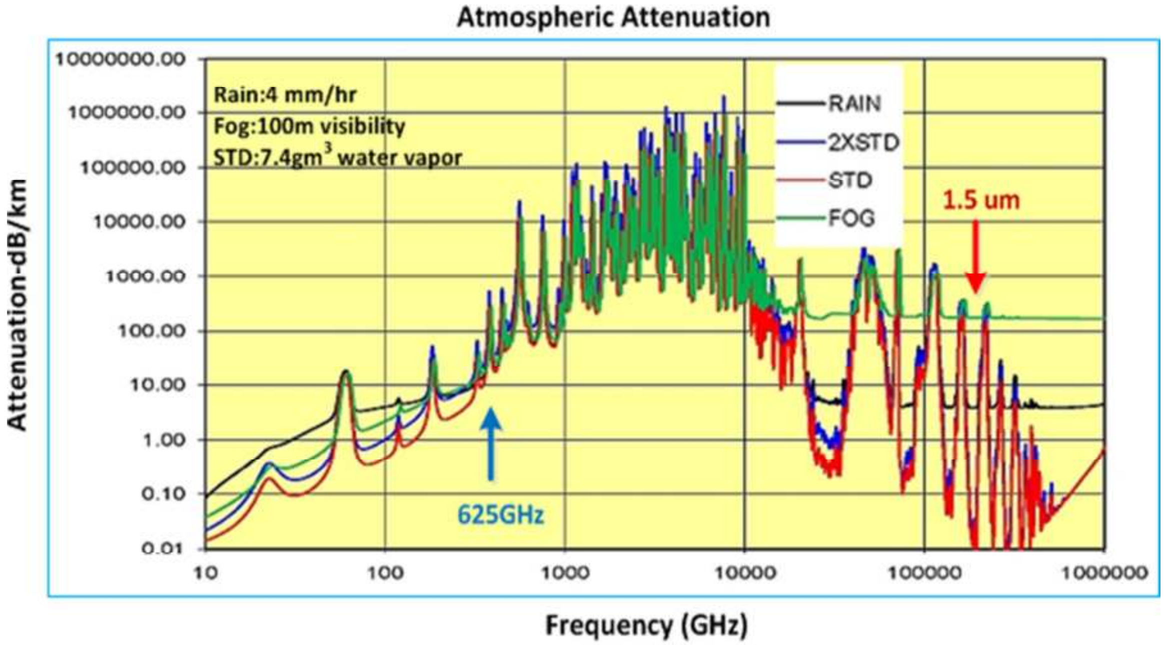

Figure 1.7 Calculated atmospheric attenuation in THz and IR band. ITU recommendations are used from 10 to 1000 GHz. MODTRAN 4 is used from 30 to 0.3 microns. A code for the 1-10 THz region was developed by MMW Concepts LLL[49]. The dashed line corresponds to 4 mm/hr of rain. The dash-dot line corresponds to 100m visibility of fog, and the solid line corresponds to US standard atmospheric conditions at sea level (59% relative humidity = 7.5 g/m^3 water content). The dotted line corresponds to 15 g/m^3 of water content. A wavelength of 1.5 µm corresponds to 2×10^5 GHz.
Source:[49]

Under fog conditions the THz absorption at ~625 GHz is around 20 dB/km which is considerably lower than the 200 dB/km that the 1.5 µm wavelength suffers. The maximum reach of THz radiation in fog can be much larger than those of usual IR based systems. Thus T-rays based communication systems could serve as a back-up for foggy weather when IR signaling fails. It also should be noted that above 200 GHz and below 10 THz, the attenuation is dominated by atmospheric water vapor, with attenuation due to rain and fog playing a minor role. In the IR, fog and smoke will cause significant attenuation.

1.3.2.2 Experimental Characterization of Environment on THz Communication Links.

As noted by Brown [50] in his extensive consideration of MMW and THz remote sensing systems, there is little or no experimental data on THz scattering by fog, rain, particulates, *etc.* Brown attributes the limited experimental data to a lack of calibrated THz instrumentation and the general difficulty in distinguishing absorption from scattering effects.

Recent measurements of THz propagation through a humid atmosphere [51] characterize attenuation of the water vapor form 0.2 to 2 THz using THz time-domain spectroscopy and show higher attenuation than previously measured or predicted in this THz transmission windows.

For the rain environment, the experimental data at 97 GHz [52] indicates a reasonable agreement between measured rain attenuation values and those predicted by different models. Differences in the measured and predicted values suggest that further measurements are required to fully validate rain attenuation models at the higher MMW or sub-THz frequency range. At a frequency region of above 100 GHz, the effect of rain has been characterized only at 103 GHz [53], 120 GHz [54], and 355.2 GHz [55]. Utsunomiya and Sekine conducted propagation experiments at 103 GHz over 390 m. The experimental data was compared with the calculation from the relationship between the attenuation and the rainfall rate for the Marshall-Palmer, Best, Joss-Thams-Waldvogel and Weibull raindrop size distributions (shown in Figure 1.8). The Weibull distribution shows a good agreement with the experiment results.

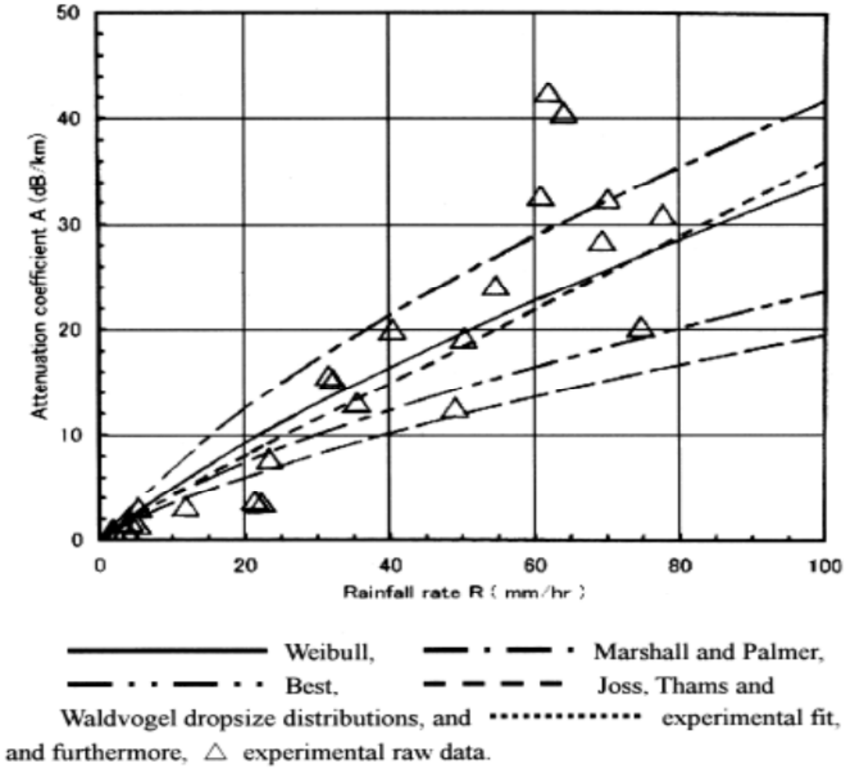

Figure 1.8 Comparison of attenuation coefficient between calculation and measurements at 103 GHz for a 1 minute integration time.
Source: [53]

In comparing the measured BER with rain attenuation, Hirata et al. [54] observe an interesting discrepancy between the experimental measurements and predicted theory. As shown in Figure 1.9, as the rain attenuation increases, the BER increases relative to the theoretical predictions from random noise theory. The author suggests two possible explanations: wave front distortions (scintillations) or the difference in the measurement cycle for rain attenuation (averaged over 1s) and BER (averaged over 100 ps).

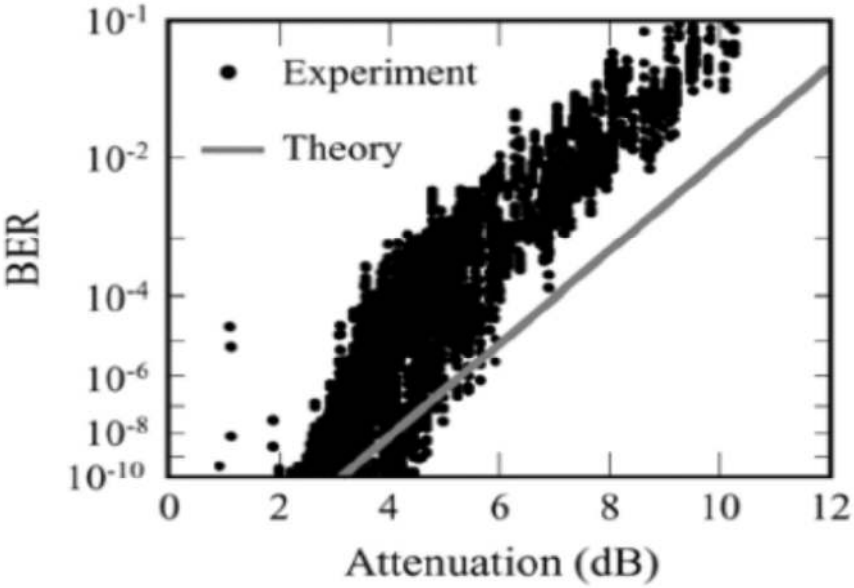

Figure 1.9 Measured BER for 120GHz wireless link (10.3Gb/s data rate) versus rain attenuation.
Source: [54]

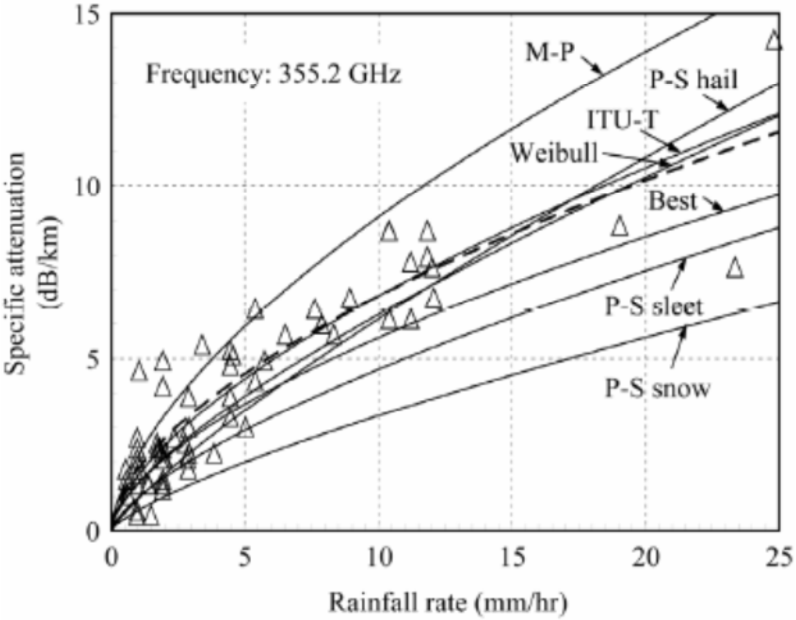

Figure 1.10 Comparison between calculation and measurements at 355.2 GHz for a 1 minute integration time.
Source: [55]

The rain attenuation at 355.2 GHz was measured at the National Defense Academy and calculated using four rain-drop-size distribution and International

Telecommunication Union (ITU-R) specific attenuation models. The calculated results were compared with propagation experiments under rainfall intensities of up to 25 mm/hr (shown in Figure 1.10), which proves that the experimental propagation results were in good agreement with of the calculation from the specific attenuation model for use in predication method recommended by ITU-R provides the best fit for the experimental data.

The first direct experimental performance comparison between THz (625GHz) and IR (1.5 µm) communication links, meaning that both signals passing the same weather conditions (fog), has been recently reported [56]. The measurements results will be described in detail in Chapter 4.

Due to the relatively small size of atmospheric particulates such as dust and smoke compared to the THz wavelength, one would expect minimal THz attenuation due to airborne particulates. Mann [57] had predicted that fog and smoke has little or no effect up to 1 THz. A rough estimate of the attenuation can be made assuming that the particulates act as spherical Mie scattering centers. Following a simple Mie scattering formalism that was used previously to study attenuation of THz radiation due to particle grains one can estimate the attenuation at IR, THz and sub-THz frequencies using known particles sizes and concentrations. The details will be discussed in Chapter 5.

1.3.3 Scintillation Effects on the THz and IR Communication Link

There have been some measurements of scintillation effects at 97 GHz which showed that the long-term probability distribution of scintillation amplitudes due to rain could be modeled by the Mousley-Vilar equation [52]. Knowledge of the scintillation amplitude distribution can be used to predict the degradation of the communication link due to scintillation. Experimental evidence that has been published concerning the effect of scintillation on THz communication includes brief comments [21, 22] and a more detailed analysis in [23]. Yamaguchi et al. [28] shows the measurement of the scintillations due to the effect of wind on the propagating 125 GHz radiation (shown in Figure 1.11). When wind velocity increased, the receiver axis deviation also increased which caused the input power to decrease. However, since the input power even in the presence of the wind was greater than the minimum required, the authors did not observe any increase in BER due to the wind.

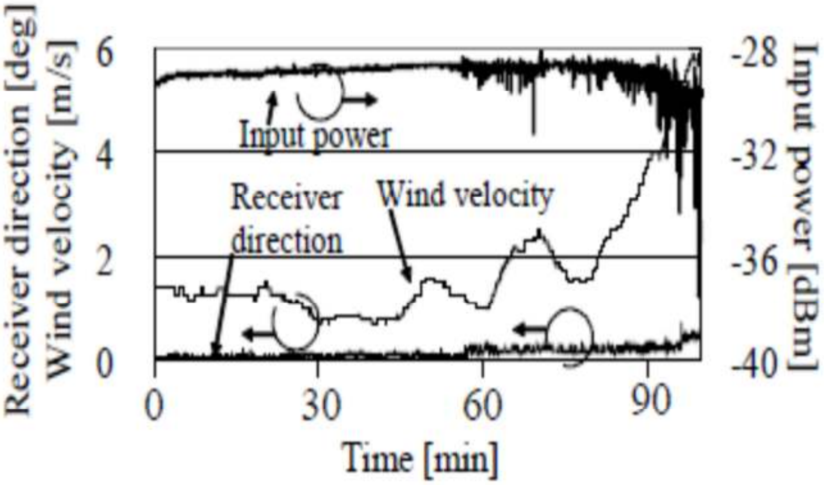

Figure 1. 11 Experiment result for the 800 m transmission: input power versus wind velocity and Receiver axis deviation.
Source: [28]

For the IR links, experimental results on scintillation were reported by Gebhart et al. [47] for a very long wireless IR link (of over 61 km). Their results show amplitude variations (at the receiver) originated by air turbulence during clear sky conditions of up to 30 dB. Their results also indicate that this problem becomes more significant as the distance between the transmitter and the receiver increases. Also, Scintillation effects have been analyzed and a variety of theoretical models have been built to characterize the scintillation effects on the IR links [58, 59].

CHAPTER 2

EXPERIMENTAL METHODOLOGY

In order to study and compare propagation features of Terahertz (THz) links with Infrared (IR) links under different weather conditions, THz and IR communication lab setups were developed. In this chapter, the experimental methodologies are presented with emphasis on the design of two types of THz communication systems, namely THz continuous-wave (CW) photomixing communication system [60-62] and frequency multiplier chain based 625 GHz communication system [32, 63]. The IR wireless communication system at 1.5 µm [56] and proportional-integral-derivative (PID) controller [64] used for dynamic range improvement for the IR system are also described.

2.1 THz CW Photo Mixing Communication System

For the THz CW photomixing configuration two laser sources are typically multiplied or mixed in a device such as a photoconductive antenna structure [65-67], where laser beams with the Terahertz difference frequency excite charge carries in the semiconductor material. Terahertz radiation is generated at the difference frequency of the two laser sources. The value of the beat frequency can be easily regulated by changing the temperature of the laser diodes, or laser current. For the communication experiments reported here, the phase of one of the lasers is modulated using an optoelectronic magnesium-oxide-doped lithium niobate (MgO: $LiNbO_3$) phase modulator, which is connected to a pseudorandom bit sequence (PRBS) generator. Since the speed of modulators can be as high as the gigahertz range, one essentially can eliminate the speed limitations due to mechanical scanning in acquiring a THz waveform.

The experimental setup for the THz CW photo mixing communication system is sketched below in Figure 2.1, which includes distributed feedback (DFB) laser system, optics, THz transmitter (Tx) and receiver (Rx), signal modulation, and detection subsystems.

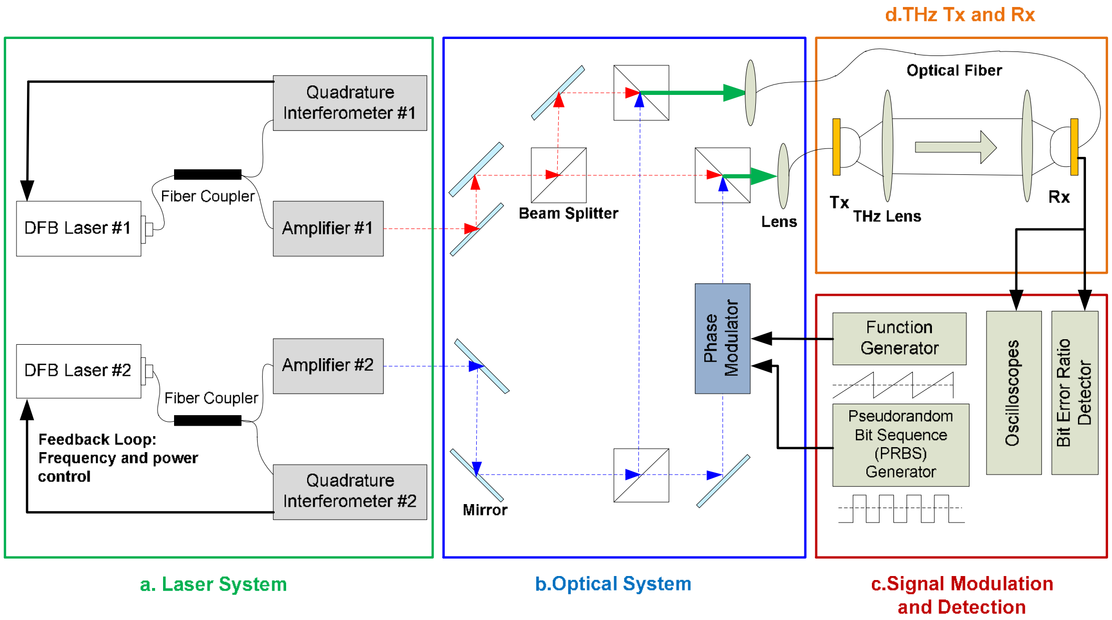

Figure 2.1 Schematic diagram for THz CW photo mixing communication system. (a) laser system (b) optical system (c) signal modulation and detection (d) THz Tx and Rx.

As shown in Figure 2.1, THz radiation is generated at the beating frequency of two single mode distributed Bragg reflector diode lasers (TOPTICA DL DFB) operating near 850 nm. The output of each laser is evenly split using the first pair of beam splitters. The MgO: LiNbO$_3$ phase modulator (New Focus 4002) is inserted into one of the beams from Laser Diode #2, which could be modulated either by analogy signal (generated by function generator) or digital signal (generated by pseudorandom bit sequence generator). After splitting and passing one beam through the modulator, the light from the two lasers are combined with another pair of beam splitters. The combined laser light is couple into polarization maintaining optical fibers and delivered to both the THz transmitter (Tx) and receiver (Rx) which are low-Temperature-Grown GaAs bowtie-type photo-conductive dipole antennae (PDA). The PDA is mounted on the back of a semi hemispherical silicon lens which reduces the divergence of the THz radiation from the antenna. The total optical power on both channels is ~25 mW. A bias of 20 V DC is applied to power the THz transmitter. Two identical THz lenses with short focal lengths (~32 mm) allow source beam transmissions over distances of 1 meter (beam diameter ~ 20 mm) followed by refocusing of the beam on the receiver side into the receiver.

2.1.1 Distributed Feedback (DFB) Diode Laser System

For the photo mixing system, it is necessary to ensure a single-mode operation of both lasers. The DFB technique is utilized in the system to eliminate multimode operation of diodes. The DFB Laser system employs two Toptica DFB diode lasers with center wavelength of 855 nm, BoosTA (high power semiconductor optical amplifiers) and ISCAN (quadrature interferometer, laser mode monitor and frequency control).

2.1.1.1 DFB Laser Source. DFB diodes feature a diffraction grating structure within the active region of the semiconductor. The structure builds a one dimensional interference grating (Bragg Scattering). The grating provides optical feedback for the laser, restricting their emission spectrum to a single longitudinal mode.

The DFB diode can be tuned by changing either the chip temperature (thermal tuning rate: 25 GHz/K (0.058 nm/K) or the operating current (electrical tuning rate: 1.1 GHz/mA (0.0027 nm/mA) [68]. Thermal tuning achieves extremely large mode-hop free scan ranges (continuous frequency scans of up to 1400 GHz can be realized by means of a temperature sweep of ~50 K). Electric tuning is favorable for rapid modulation and frequency stabilization tasks.

Each DFB Laser is protected from optical feedback by a 60 dB isolator, and coupled into the 90:10 single mode (SM), polarization-maintaining Panda fiber coupler. Its weaker output, approximately 1% of the guided light intensity, is launched in the ISCAN (quadrature interferometer) used in the frequency and power control loops of the respective laser. Another port is connected to the BoosTA (amplifiers).

2.1.1.2 BoosTA (High Power Semiconductor Optical Amplifiers). The BoosTA is the high power semiconductor optical amplifier. With 40 mW BoosTA input power, the maximum power after amplification can reach 400 mW, which provides the high power source for the terahertz generation.

2.1.1.3 ISCAN (Quadrature Interferometer). The attainable frequency resolution of a CW terahertz setup is only limited by the frequency stability and linewidth of the utilized laser sources. However, the sensitivity of the DFB wavelength to changes in temperature-the very effect responsible for the large tuning range-makes the DFB laser susceptible to frequency jitter and drifts. Without active frequency control, this result in a technical linewidth of ~5 MHz on time scale of 100 ms, while the drift can be as high as several 100 MHz within few minutes. For high-speed terahertz communication, this is clearly not sufficient.

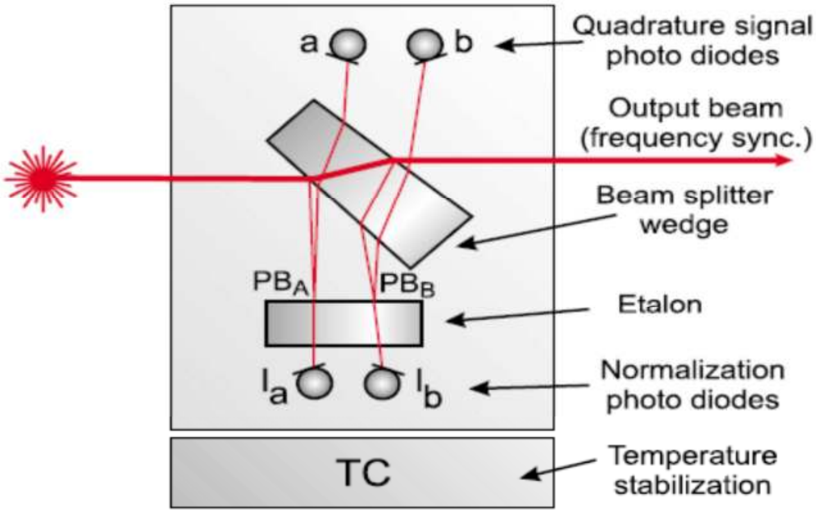

Figure 2.2 Quadrature interferometer (ISCAN).
Source: [68]

For frequency stabilization as well as controlled frequency tuning, each DFB laser is regulated by electronic feedback from a fiber-coupled quadrature interferometer (ISCAN) [69]. The principle of the ISCAN is based on quadrature signal generation within a low-finesse temperature stabilized Fabry-Perot etalon (Figure 2.2). A wedge shaped beam splitter within the interferometer head generates two low-intensity probe beams (PB_A and PB_B), which enter a low-finesse, temperature-stabilized Fabry–Perot etalon (free spectral range of 7.7 GHz) under slightly different angles. The etalon generates a pair of interference signals with a relative phase of $\pi/2$. These signals are detected by two photodiodes (a, b) and combined into a quadrature signal, the phase of which is a linear function of the optical frequency. Two further photodiodes within the quadrature interferometer serve to monitor the laser intensity. The intensity value is used in an additional control loop that corrects the laser current in order to maintain a constant average output power over the entire tuning range of the DFB laser.

The normalized quadrature signal can be visualized on an oscilloscope operating in XY-mode: when the laser frequency is scanned, each of the photodiodes a and b detects an oscillating, near-sinusoidal signal. The XY-display yields a circle, where the momentary phase angle corresponds to the laser frequency. The completed circumference of the circle represents the range of the frequency scan. A mode-hop free scan yields a smooth curve, whereas a mode-hop within the scan range is recognized by a sudden jump across the circle (Figure 2.3). Using the Iscan, the frequency stability can be better than 20 MHz/24 hours.

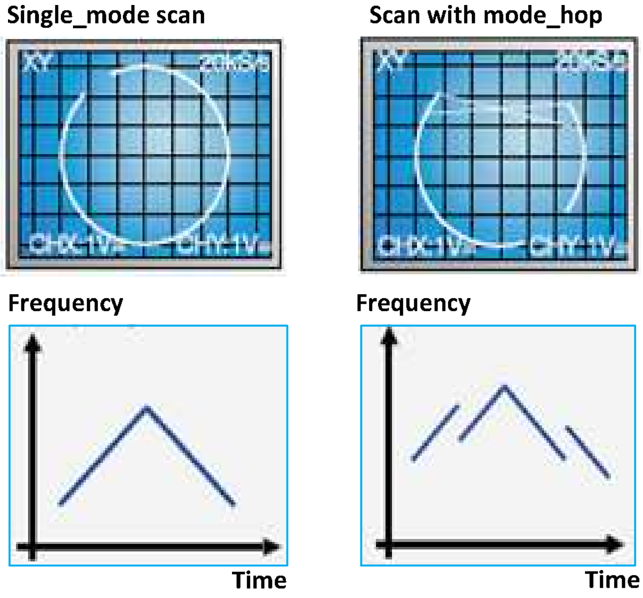

Single_mode scan

Scan with mode_hop

Figure 2.3 Quadrature signal and corresponding mode signatures.
Source: [68]

2.1.2 Signal Modulation

A New Focus 4002 MgO: $LiNbO_3$ phase modulator is used in the experiments, which can be operated at any frequency from DC to 100 MHz. It is based upon the linear electro-optic effect—the change in the refractive index is linearly proportional to the applied electric field. The applied voltage induces a change in refractive index along the polarization axis of the infrared laser beam. By varying the applied voltage to the phase modulator, the optical path length experienced by the propagating laser beam varies proportionally.

The configuration of phase modulator is illustrated in Figure 2.4. It contains an electro-optic crystal of length l with electrodes separated by the crystal thickness d (the electrode spacing). The voltage V is applied directly across the crystal's electrodes, which is perpendicular to the light propagation (transverse modulation mode). The generated electrical field can be expressed as:

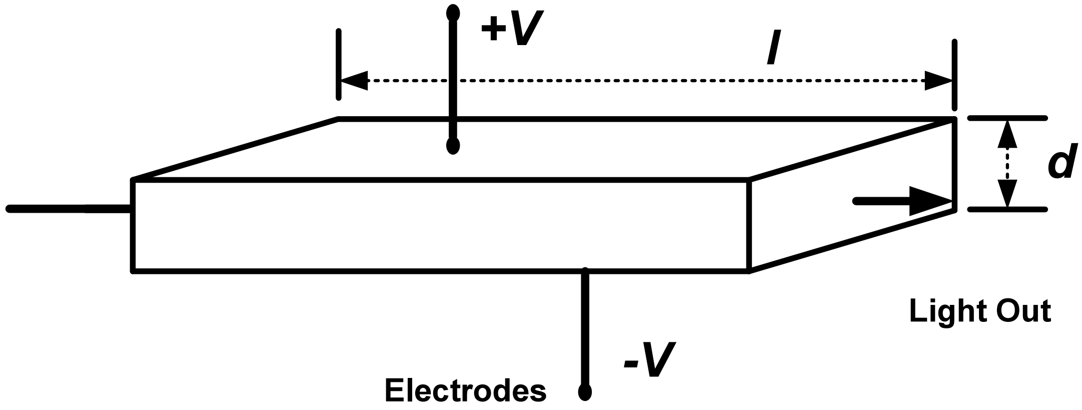

Figure 2.4 Electro-optic phase modulator.

$$E = \frac{V}{d} \tag{2.1}$$

The induced index of refractive change by an external electric field signal is:

$$\Delta n = \frac{1}{2} n_e^{3} r_{33} E \tag{2.2}$$

where Δn is the change of the refraction index, n_e is the unperturbed refraction index of the crystal (the refractive index of the crystal at zero voltage) and r_{33} is the electro-optic coefficient. The phase shift obtained by applying a voltage V at the input SMA (SubMiniature version A) connector can be expressed as:

$$\Delta\varphi = \frac{2\pi}{\lambda}\Delta L = \frac{2\pi}{\lambda} l\Delta n \tag{2.3}$$

where L is the optical path length (OPL), l is the geometric length of the crystal and λ is the vacuum wavelength of the DFB laser. Substituting Equations 2.1 and 2.2 into 2.3, yields a phase change as a function of:

$$\varphi_m(t) = \frac{\pi}{\lambda} n_e{}^3 r_{33} \frac{l}{d} V(t). \tag{2.4}$$

The half-wave voltage is defined as the voltage that could produce a phase shift of π, which is

$$V_\pi = \frac{d}{n_e{}^3 r_{33} l}\lambda \tag{2.5}$$

For the phase modulation model 4002, the half-wave voltage is typically 178 volts at 850 nm, corresponding to a modulation depth, β, of 0.0176 radians/volt.

2.1.3 THz Generation and Detection

2.1.3.1 Theory. THz radiation is generated by photo mixing of the two laser beams in the THz transmitter. The generated THz wave can be presented as a product of electric fields[62],

$$E_{THz} \sim \overrightarrow{E_1} \cdot \overrightarrow{E_2} \sim E_1 \sin(\omega_1 t + \phi_1) E_2 \sin(\omega_2 t + \phi_2) \sim E_1 E_2 \left[\cos(\Delta\omega t + \Delta\phi_o)\right] \tag{2.6}$$

where $\Delta\omega = \omega_1 - \omega_2, \Delta\phi_0 = \phi_1 - \phi_2$, E_1 and E_2 are the amplitudes of infrared DFB electric fields at the frequencies ω_1 and ω_2, and phases ϕ_1 and ϕ_2, respectively. In Equation 2.6, it is assumed that the polarization of the two beams from laser diode #1 and #2 are parallel so that the vector dot product of the infrared E fields simply becomes a scalar multiplication. The electro-optic phase modulator will induce an addition phase shift $\phi_m(t)$ which gives:

$$E_{THz} \sim E_1 E_2 \left[\cos(\Delta\omega t + \Delta\phi_o + \phi_m(t)\right] \tag{2.7}$$

The detected THz signal is determined by mixing (multiplying) the incoming THz radiation of Equation 2.7 with the two infrared DFB signals present at the THz detector:

$$E_{\det} \sim E_{THz} \cdot (E_1 \cdot E_2) \sim E_{THz}(t, \phi_p) E_1 \sin(\omega_1 t + \phi_3) E_2 \sin(\omega_2 t + \phi_4) \tag{2.8}$$

Simplifying Equation 2.8 gives

$$E_{\det} \sim E_1^{\,2} E_2^{\,2} \cos(\phi_m(t) + \phi_p + (\phi_1 - \phi_3) + (\phi_2 - \phi_4)) \tag{2.9}$$

where ϕ_3 and ϕ_4 represent the phase of the beams from DFB #1 and DFB #2, respectively, at the THz receiver. The phase shift ϕ_p is induced by the free space between the transmitter and receiver. Consequently, the voltage produced by the THz detector varies sinusoidally with a linear increasing applied voltage to the phase modulator.

2.1.3.2 Photoconductive Antenna. THz Transmitter and Receivers are low temperature grown Gallium Arsenide (LT-GaAs) antennas [70, 71]. THz radiation is generated using a photoconductive emitter consisting of a small piece of semiconductor crystal (commonly gallium arsenide) on which two planar metal electrodes form an antenna supporting a large electric field across its surface (see Figure 2.5). A laser beam (with some beat frequency $\omega_1 - \omega_2$) is focused onto the gap between the electrodes. This generates charge carriers in the form of electron–hole pairs at the plate of the semiconductor. The application of a bias voltage accelerates these charge carriers. An induced current is generated, which radiates a THz wave into the free space. An external silicon lens reduces the divergence of the THz radiation from the antenna. The photoconductive receiver (operating in reverse way to the transmitter) is used as the detection technique.

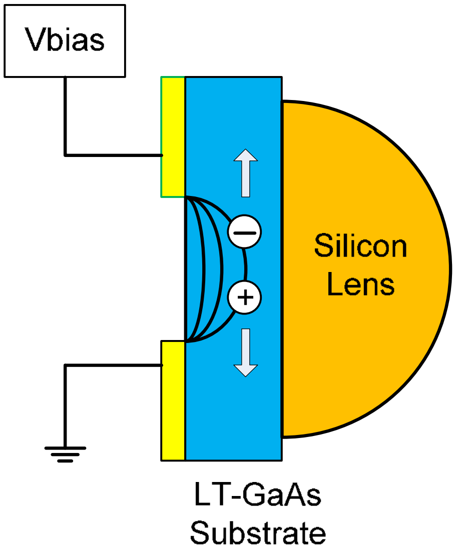

Figure 2.5 Terahertz generation laser-gated photoconductive antenna Vbias: Bias voltage applied to the gallium-arsenide (GaAs) substrate.

2.2 Frequency Multiplier Chain Based 625 GHz Wireless Communication System

In order to obtain simultaneously high output power and larger transmitter bandwidth at a high carrier frequency, a frequency multiplier chain based a 625GHz wireless communication system was developed. A duobinary modulation technique [72, 73] utilized in the system ensured a sufficiently narrow spectrum bandwidth to pass an up-converting frequency multiplier chain. Compared to other transmitter architectures, the source seems to have advantages in terms of maximum output power when considering currently commercially available components. On the receiver side, a Schottky diode operated in direct detection modes, convert the THz signal to baseband, which is less complex than mixer based receivers. The block diagram (Figure 2.6) shows the main transmitter and receiver elements of the up converting frequency multiplier chain based 625 GHz transmission link.

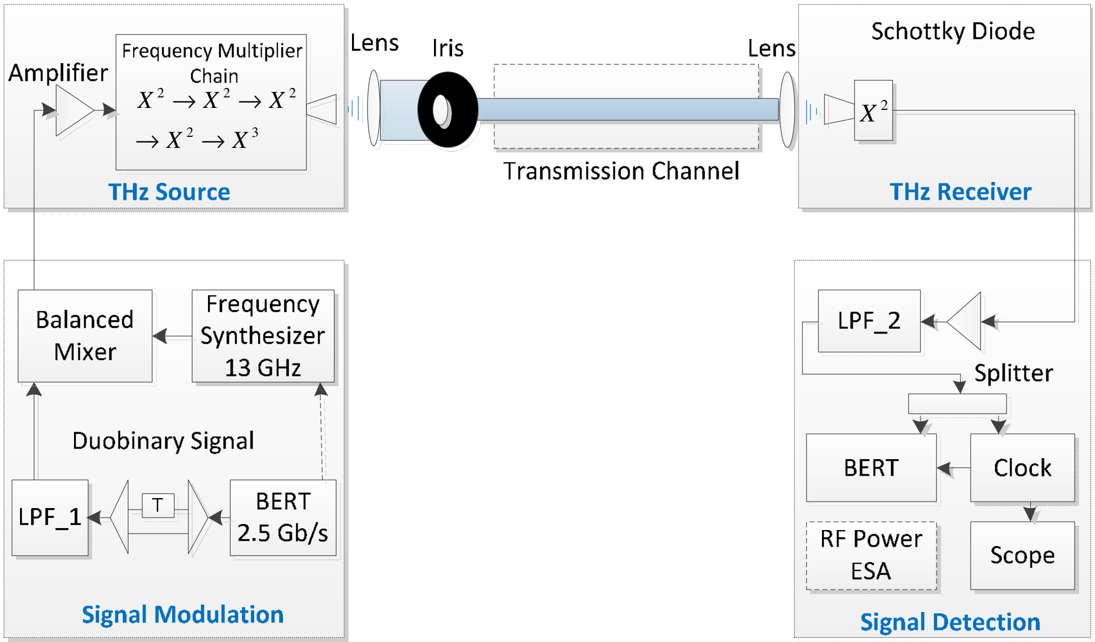

Figure 2.6 Schematic of up converting frequency multiplier chain based 625 GHz transmission link.

2.2.1 THz Source

The THz source (Virginia Diodes Inc.) is based on a Frequency-Multiplier-Chain with about 1 mW output power when operated in a continuous wave (CW) mode. It consists of an amplifier driven at 2 W saturation power followed by four frequency doublers and one frequency tripler, all based on biased Schottky diodes, which feed a horn antenna with 2.4 mm aperture. A launched tone within the frequency acceptance band between 12.2 GHz and 13.6 GHz gets up converted into a frequency band between 585 GHz and 653 GHz. The biasing of the Schottky diodes is actively controlled. However, the feedback loop cannot counteract amplitude variations by a data modulation due to its bandwidth limitation to the kHz range.

2.2.2 Signal Modulation (Duobinary Modulation)

The source's acceptance frequency band between 12.8-13.6 GHz for an applied input RF tone requires multi Gb/s data rate signals with comparably narrow bandwidth such that intersymbol interference (ISI) effects [74] caused by bandwidth reduction can remain small. Duo-binary modulation yields a relatively compact spectrum compared to regular (non-return-to-zero) NRZ modulation by applying phase coding and pulse widening. Several techniques have been proposed to generate duobinary modulation. The delay-and-add approach is applied in the system.

As shown in the signal modulation block of Figure 2.6, a 2.5 Gb/s NRZ format is generated by a pulse pattern generator (PPG) with adjustable output power. The signal is divided into two replicas by means of a wideband 6 dB electrical power splitter and one branch is delayed by the duration of a bit (400 ps) with respect to the other. The replicas are combined with another 6 dB power splitter, terminated with 10 dB 50 Ohm attenuators at both input, in order to achieve better impedance matching and less reflections. A quasi Gaussian low pass filter (LPF-1) with about 1700 MHz 3 dB bandwidth is then applied to reduce the spectral width of the signal, mainly by cutting off its tail. This signal is launched into the intermediate frequency (IF) port of a double balanced mixer where the data modulates the output of a frequency synthesizer that is connected to the local oscillator (LO) port. It is a specific feature of the double-balanced mixer that a negative input at the IF port causes a 180 degree phase shift of the signal at the radio frequency (RF) output. This is utilized to establish the required phase coding for duobinary modulation. The data signal enters the THz source and modulates the THz radiation which emanates from the horn antenna of the THz source with 2.4 mm aperture.

Note, after the first frequency doubler of the source, the duobinary phase coding is eliminated due to the squaring operation of the Schottky diode.

2.2.3 Transmission Channel

The output of the horn antenna is collimated by a THz lens (beam diameter ~20 mm) with short focal length (~32 mm) and transmitted over distances with up to a few meters length. After that an identical THz lens couples the beam into a receiver horn similar to the transmitter antenna whose output is connected to a zero biased Schottky diode.

2.2.4 THz Receiver and Signal Detection

The detector functions in the low power region (input power <10 mW) to good approximation as a square law converter with a responsitivity of about 2500 V/W at 600 GHz. The Schottky diode's output is amplified by about 42 dB using two amplifiers (80 kHz-7 GHz pass band, 6 dB noise figure, maximum output power~19 dBm) and filtered by a quasi-Gaussian low pass filter (LPF-2) with 3GHz 3dB-bandwidth. A 6dB electrical power splitter launches one output (Vpp~500mV) to a high-speed scope or a Bit Error Rate Tester (BERT) and the other to a 2.5 Gb/s NRZ clock recovery circuit that synchronizes the measurement equipment.

Note that the current detector design, based on commercially available Schottky diodes, is suboptimal for high-speed signaling. The video resistance of the diodes, under low input power, is nominally ~1.5k Ohm and connected via a series of 50 Ohm transmission lines and cables to an external high-speed electrical amplifier with matched input impedance [75]. For low speed applications and after replacing the amplifier with a high impedance device, a voltage of about 70 mV at the Schottky diode output is detectable. However with 50 Ohm termination of the diode a significantly smaller voltage level is accessible at the high-speed amplifier input. A rough estimate (applying voltage divider rule 50/1550) shows thus only about 3% of the signal voltage generated in the Schottky diode is applied to the amplifier input. This estimate can be used to determine the operation regime of the diode. At the amplifier output RF powers of about -14 dBm for a BER around 10^{-9} is typically. Assuming an amplifier gain of about 42 dB, the aforementioned voltage conversion factor of the diode, and a diode responsivity of 2500 V/W yields an effective launched THz power of about 20 μW. This is significantly more than the vendor specs for the linear operation range of the device. An iris with 8.5 mm aperture, inserted concentrically into the beam, limits its total power to an amount that results in a BER of about 10^{-7} for an unloaded fog chamber.

2.3 IR Wireless Communication System at 1.5 µm

The block diagram (Figure 2.7) shows the main transmitter and receiver elements of IR communication link, data acquisition interfaces, and proportional-integral-derivative controller (PID controller) for IR power stabilization.

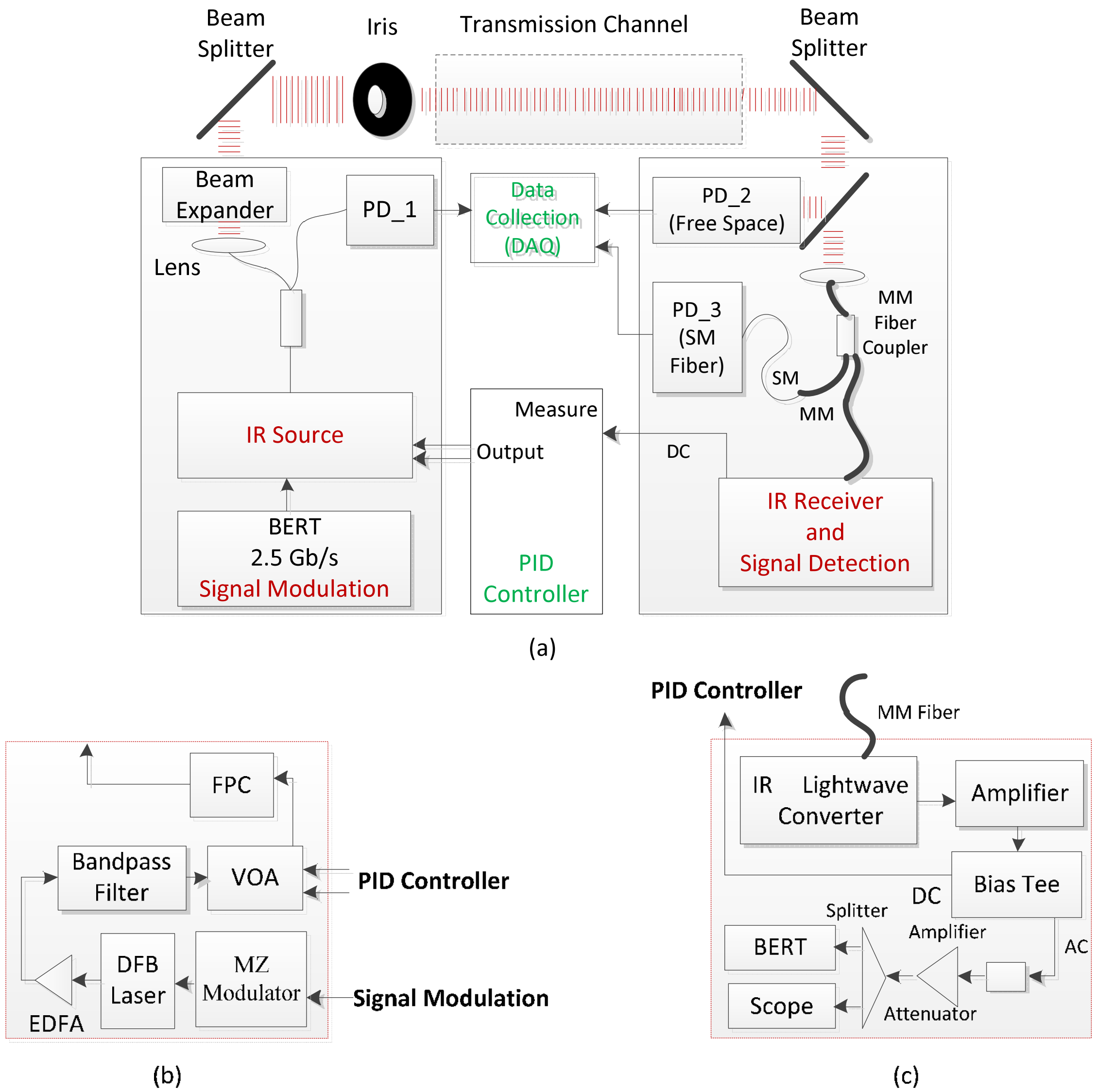

Figure 2.7 (a) Schematic diagram of IR wireless communication link, (b) IR source, (c) IR receiver and signal detection.

2.3.1 Transmitter and Receiver Elements of IR Communication Link

The IR transmitter (Figure 2.7 (a)) consists of a DFB laser (wavelength~1550 nm), a Mach-Zehnder optical modulator, a high power erbium-doped fiber amplifier (EDFA), a narrow bandwidth optical filter (~1 nm bandwidth), a low loss variable optical attenuator (VOA) and a fiber based polarization controller (FPC). All are connected by standard single mode fiber. The beam splitting ratio is polarization dependent and the FPC is adjusted to achieve the maximum detectable receiver power. The Mach-Zehnder modulator is driven by the same 2.5 Gb/s NRZ signal as the THz transmitter. An EDFA amplifies the modulator output to about 25 dBm, the maximum input power of the bandpass filter, which reduces the detection of spontaneous emission on the receiver side. After passing through the VOA, controlled by a proportional-integral-derivative controller (PID controller), the IR signal is launched into the 90:10 single mode (SM) fiber coupler. Its weaker output, launched into photo detector PD-1 serves as monitor for the power entering the fog chamber. A fiber collimator expands the IR beam to about 20 mm diameter, which is comparable to the THz beam size before the iris.

The collimated IR beam could be superposed with the THz beam using a beam combiner (see above) with 55% reflection ratio at 45 degree incident angle, transmitted through the environment chamber (such as fog, dust, humidity chamber), and deflected at its output with a similar beam splitter to spatially separate THz and IR signals. The second beam splitter taps of a fraction of the IR power leaving the chamber and launches it towards a large area photo diode (effective area 19.6 mm^2) of detector PD-2, which in combination with PD-1 is used to determine the power loss caused by the chamber load. The remaining beam power enters via a fiber collimator a 1x2 multi-mode (MM) fiber coupler with 50:50 splitting ratio. Its output power is launched to a low bandwidth photo detector (PD-3) with a 1 m long standard single mode fiber (SSMF) and to a dc-coupled IR lightwave converter (Agilent 81495A) with 9 GHz bandwidth. The lightwave converter is twofold used for data detection and measuring the optical power of the incoming signal, which is accessible via general purpose interface bus (GPIB). A bias tee (Figure 2.6 (c)) at the converter output allows for extracting a voltage proportional to the

DC components of the data signal, which serves as feedback for the PID controller of the VOA. The ac-output of the bias tee is strongly attenuated and thereafter amplified in order to level the signal-to-noise ratio (SNR) such that BERs around 10^{-7} and higher can be adjusted while satisfying the BERT requirements of input voltage swings between 250 mV and 2 V.

2.3.2 Proportional-Integral-Derivative Controller (PID Controller)

2.3.2.1 Introduction of PID Topology. The controller consists of a front end with differential input amplifier (proportional control), followed by an integrator and a differentiator, arranged in what is known as ‘ideal’ PID topology. PID topology provides a simple way to minimize the effect of disturbances to a system. As shown in Figure 2.8, A PID controller calculates an "error" value as the difference between a measured process variable and a desired setpoint (ε =set point-measured process variable). Then the controller uses the error to generate three control signals:

1. Proportional, the amplified error: $P \times \varepsilon$
2. Integral, the time integral of the error signal multiplied by a gain coefficient : $I\int \varepsilon dt$
3. Derivative, the time derivative of the amplified error signal multiplied by a gain coefficient $D : D\frac{d\varepsilon}{dt}$

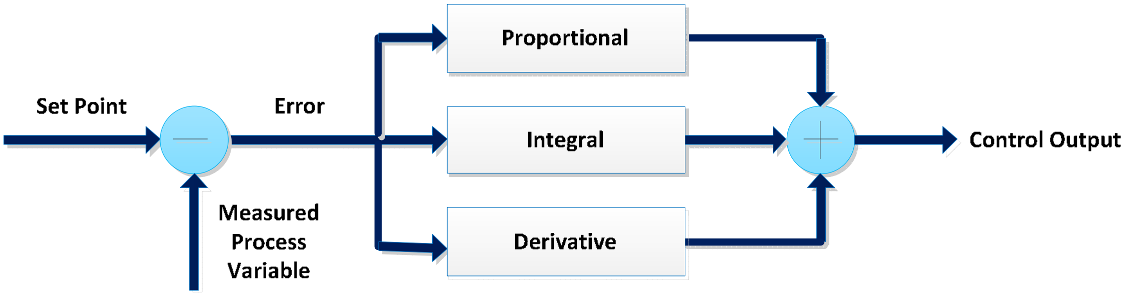

Figure 2.8 The block diagram of PID controller.

After three correcting terms, the proportional, integral, and derivative terms are summed to calculate the output of the PID controller. The final form of the PID algorithm is:

$$Output = P \times \varepsilon + I \int \varepsilon dt + D \frac{d\varepsilon}{dt} \tag{2.10}$$

By tuning the three parameters in the PID controller algorithm, the controller can provide control action designed for specific process requirements. The response of the controller can be described in terms of the responsiveness of the controller to an error, the degree to which the controller overshoots the setpoint and the degree of system oscillation.

2.3.2.2 PID Controller for the Fog Environment. One expects significantly higher attenuation levels for the IR signal than the THz beam when passing through fog. Simulations suggest that the losses in dB/m differ by a factor between approximately 10 and 100. While in the setup power measurements can be performed easily over a dynamic range of 40 dB, BER recordings for determining the data signal quality typically cover only a few dB of receiver input power variation. In order to increase the dynamic range of the IR system for BER recordings, the PID controller, adjusting the launched power into the chamber, is applied. Thus even at high attenuation levels the receiver power drops only insignificantly or stays constant. The output of PID controller is connected to a variable optical attenuator (VOA) with comparable short response time (< 10 μs) but nonlinear response curve. An external voltage, equivalent to the output of IR lightwave converter for the case of an unloaded fog chamber and a BER~ 10^{-6}, serves as reference for the PID controller. When fog starts to attenuate the received data signal, the control loop decreases the initially set attenuation of the VOA to keep the power level on the receiver side constant. Typically, the control loop can cover a dynamic range of about 5 to 10 dB under stable operation.

2.3.3 Data Acquisition

The output of PD-1, PD-2, and PD-3 are recorded via a DAQ board with 16 bit resolution and 1 kHz and 10 kHz sampling rate, sufficiently high to track even the fastest fluctuations of the signals. BERs, RF power of THz signal, and optical power of the IR signal are recorded via GPIB. A LabView time controller, set to a minimum clock rate of 500 ms, which the GPIB interface can handle, synchronizes all recordings.

CHAPTER 3

PERFORMANCE ANALYSIS AND CHARACTERIZATION OF THE DATA LINKS

In this chapter, data modulation and transmission of THz signals and IR signals are demonstrated and analyzed. For the THz CW photomixing communication system, THz signal are phase encoded with both analog ramp signal and pseudorandom binary data, transmitted over a short distance and detected. The limitations of transmission bandwidth, low signal to noise ratio, vibration effects are also discussed here. The THz spectrum response exhibits significant spectral peaks and valleys. To circumvent the inherent limitation of the THz CW system and compare propagation features of THz links with IR links under different weather conditions, a THz and IR communications lab setup with a maximum data rate of 2.5 Gb/s at 625 GHz carrier frequency and 1.5 µm wavelength , have been developed, respectively. A usual non return-to-zero (NRZ) format is applied to modulate the IR channel but a duobinary coding technique is used for driving the multiplier chain-based 625 GHz source, which enables signaling at high data rate and higher output power. The bit-error rate (BER), signal-to-noise ratio (SNR) and power on the receiver side have been measured, which describe the signal performance.

3.1 Characterization of THz CW Photo Mixing Data Link

3.1.1 Analog Ramp Signal Modulation

According to Equation 2.9, the output voltage from THz receiver (Rx) varies sinusoidally with a linearly increasing applied voltage. However, if the voltage swing corresponds to a phase shift that was either smaller than or larger than 2π, the output voltage from the THz

Rx would not be perfectly sinusoidal. The corresponding voltage swing required for a complete 2π phase shift in the modulator is 360 V.

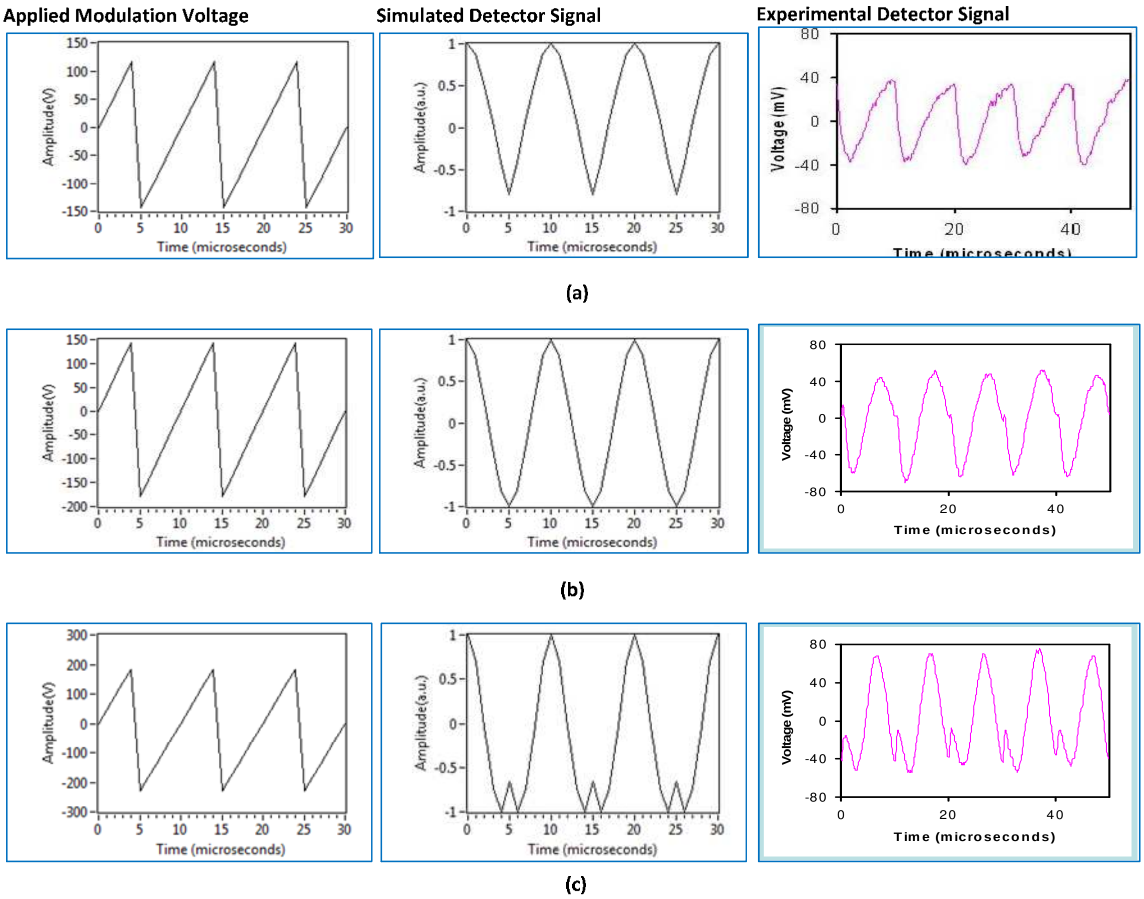

Figure 3.1 THz detector voltage output versus time as a function of modulated phase. The sawtooth waveforms (left column) illustrate the modulated voltage (modulation rate is 100 kHz). Middle column and left column are simulated detector signals and experimental detector output, respectively. (a) Phase modulation is 5 radian (smaller than 2π), corresponding modulation voltage is 290 V (b) Phase modulation is 2π , corresponding modulation voltage is 360 V (c) Phase modulation is 8 radian (larger than 2π), corresponding modulation voltage is 460 V.

As shown in Figure 3.1, a linear voltage ramp waveform with different maximum voltages swing corresponding to 5 radian (smaller than 2π), 2π, and 8 radian (larger than 2π) phase shift were applied to the phase modulator, the output of the THz receiver can then be recorded with a digital oscilloscope that locks to the ramp modulation frequency. The need for a complete 2π phase shift in the modulator is illustrated in Figure 3.1.b. For voltages below the equivalent of 2π phase shift (5 radian in Figure 3.1.a), the output waveforms are not complete sinusoids. For voltages that are too large (8 radian in Figure 3.1.c), a voltage swing larger than one cycle is observed. Also simulation results (middle column) are presented which matches well with the experimental waveforms (right column). Note, in order to achieve the clear waveforms and suppress the noise, the experimental waveforms shown in the Figure 3.1 are averaged 20 times.

3.1.2 Pseudorandom Bit Sequence (PRBS) Modulation

For the communication experiments reported here, the phase modulator is connected to a PRBS generator instead of a function generator. The PRBS data are linearly mapped onto the THz signal and form its envelope. The lasers are detuned by 0.16 nm which corresponds to 0.08 THz which is in the power peak region for the CW photomixing system. The amplitude of receiver output is 2 V with the separation of 2 cm between the THz Tx and Rx. A high impedance sampling scope recorded 150, 200, 400 and 500 kb/s eye diagrams (Figure 3.2) at the receiver output, which shows the data-rate-dependent intersymbol interference (ISI) caused by limited receiver bandwidth and high noise level.

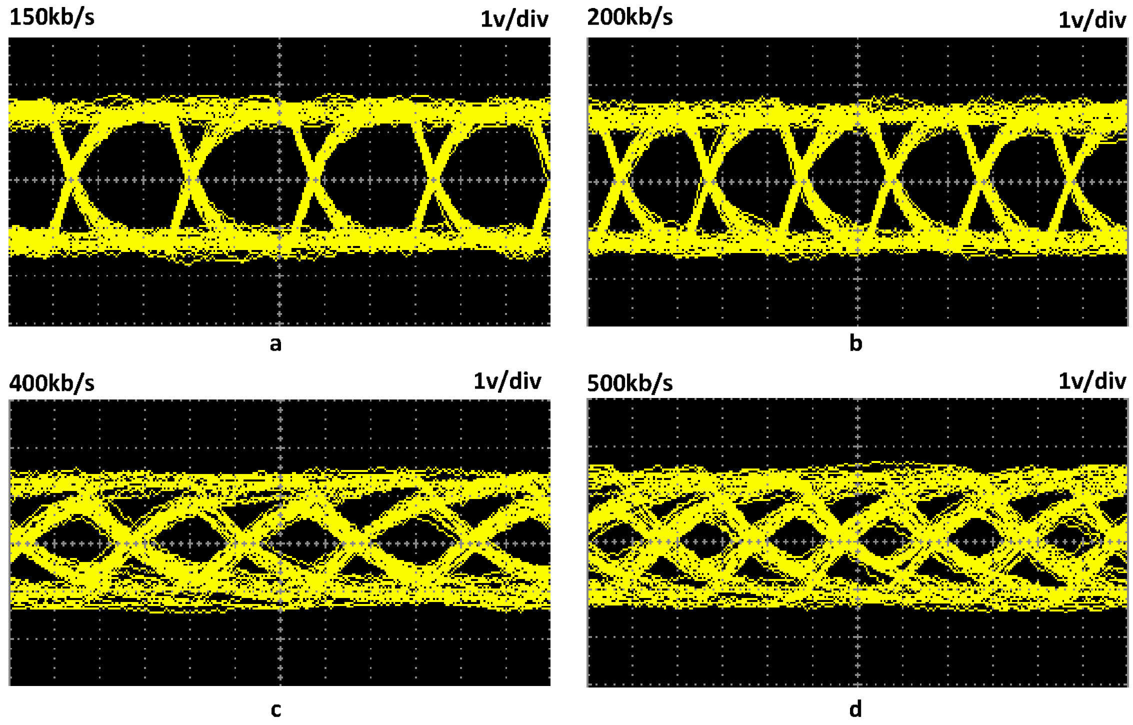

Figure 3.2 Eye diagrams at different data rates (a) data rate: 150 kb/s (b) data rate: 200 kb/s (c) data rate: 400 kb/s (b) data rate: 500 kb/s.

3.1.3 Characterization of THz Tx and Rx by Fast Spectrum Scanning

To demonstrate the utility of the method for fast spectral scanning, the lasers are detuned up to 1 THz by changing the temperature of two laser diodes. Figure 3.3 (a) illustrates the measured THz amplitude as measured with a digital lock-in amplifier (EG&G instruments, Model 7260) using a time constant of 640 μs. The THz is scanned at 1 GHz step per data point. The acquisition time for the 1000 data points scan of Figure 3.3 (a) (1 THz) is only several minutes.

However, Figure 3.3 reveals significant structure in the THz spectrum. Three power peaks are around 48 GHz, 91 GHz, and 133 GHz. If Figure 3.3 (a) is plotted in the logarithmic scale (Figure 3.3(b)), one can easily distinguish that the active range of spectrum only exists between the 30 GHz and 130 GHz. In order to explore the finer structures, a spectrum scanning from 30 GHz to 130 GHz with 100 MHz step size was performed. As shown in Figure 3.3(c), rather than a smoothly varying spectrum, significant structures in the spectrum can be observed.

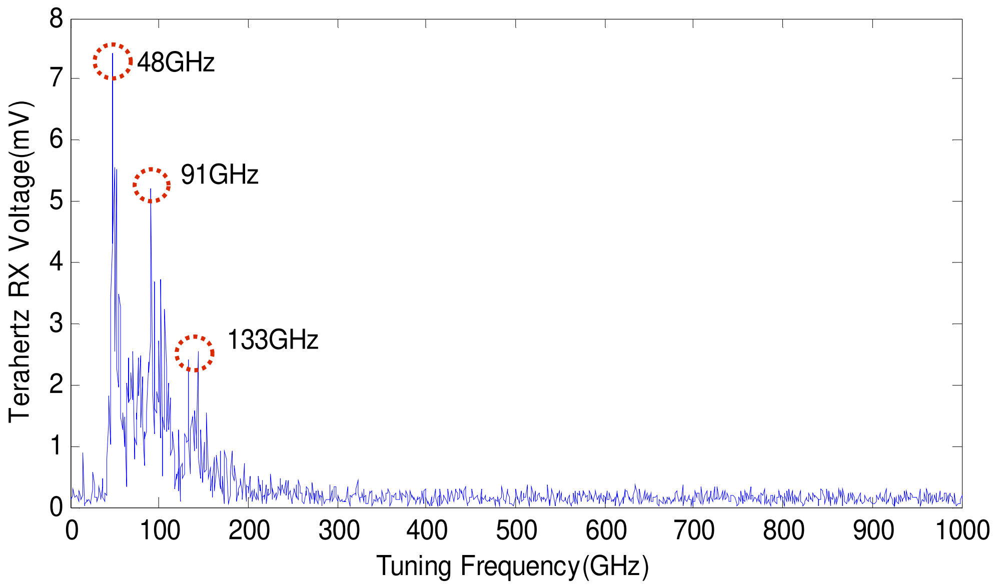

(a)

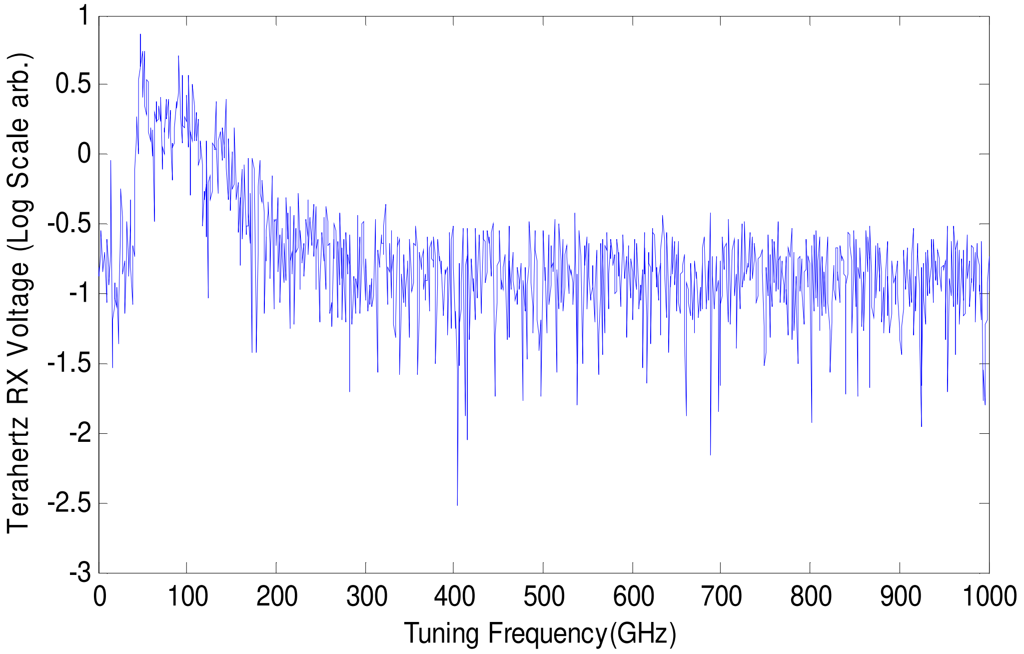

(b)

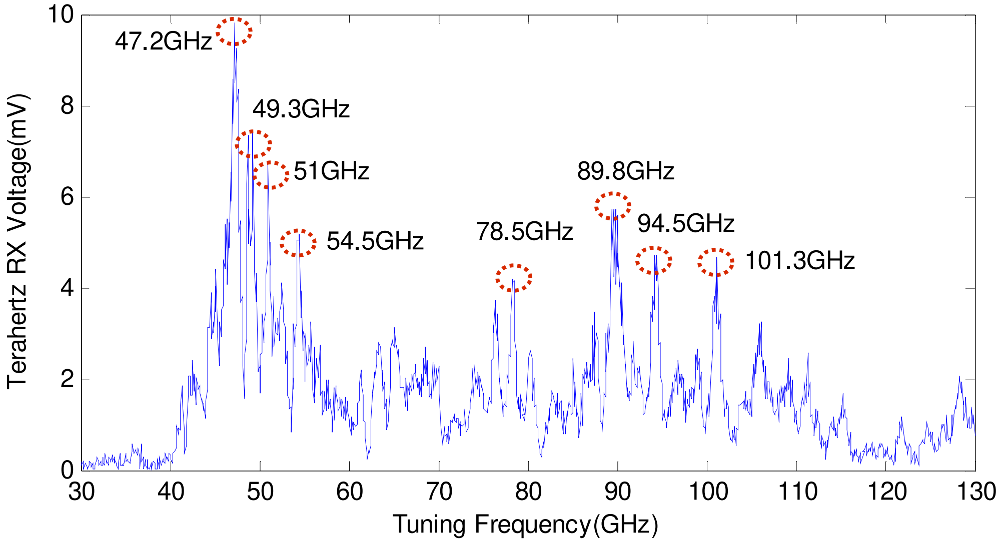

(c)

Figure 3.3 Rapid frequency tuning curves for the measured THz (a) 1 THz scanning range with 1 GHz step (b) Unit in logarithmic scale with 1 GHz step (c) 30 GHz to 130 GHz scanning range with 100MHz step.

3.1.4 Limitation of THz CW Photo Mixing Data Link

Analog ramp signal modulation, PRBS digital signal transmission, and fast spectrum scanning were demonstrated in the previous sections. The transmission bandwidth, low signal to noise ratio, vibration effects and significant structure of the THz Tx and Rx which limits the maximum transmission distance and bit error rate (BER) measurement will be discussed in the following sections.

3.1.4.1 THz Tx and Rx Spectrum Limitation. As shown in Figure 3.3, when the frequencies of two lasers are detuned from 0 THz to 1 THz, the detected signals from THz receiver contains quite abundant structures; especially there are three power peak regions around 48 GHz, 91 GHz and 133 GHz. Also the effect region of THz signals for this hardware system is limited to 200 GHz. Because of low THz signals above 200 GHz, the THz photomixing communication system can only operate at selected frequencies below 200 GHz. Unfortunately, within this frequency range, the atmosphere effects (humidity, fog, rain, particulates) on the THz transmission are relative low compared to higher THz frequencies, which means the comparable experiments of THz and IR under different weather conditions cannot be performed with the CW photomixing system.

3.1.4.2 Bandwidth Limitation. The RF bandwidth of the (MgO: $LiNbO_3$) 4002 phase modulator is 100 MHz and the electronic bandwidth of the amplifier of the photoconductive antenna (PDA) THz receiver is roughly 420 kHz. So the maximum speed of the current system is limited by 420 kHz.

3.1.4.3 Low Signal to Noise Ratio (SNR) and Vibration Effects.

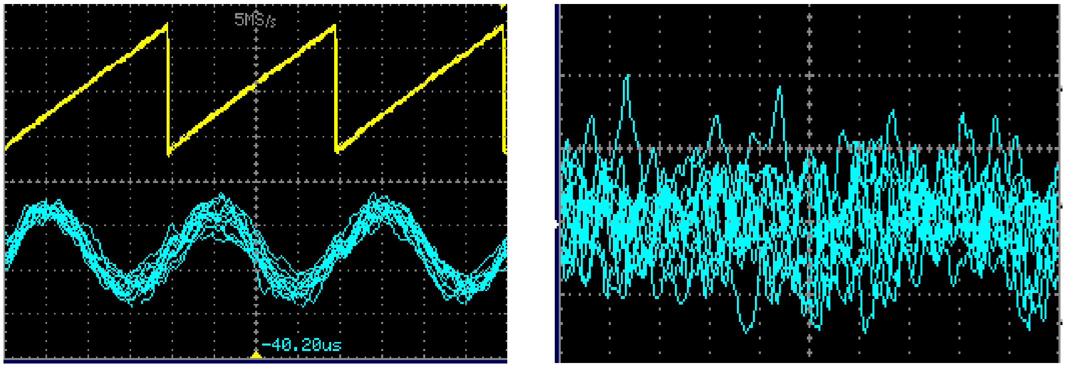

CH1 (yellow line): 5v/div
CH2(blue line):500mv/div
(a)

CH2(blue line):200mv/div
(b)

Figure 3.4 (a) THz detector voltage output versus time as a function of modulated phase. (modulation rate is 100 kHz, THz carrier wave frequency: 91 GHz). CH1: the sawtooth waveform (modulation function) CH2: detected signal from THz Rx. (b) noise level.

The 100 kHz ramp signals are modulated on the THz carrier wave at 91GHz (power peak region), transmitted and detected. The separation of the THz Tx and Rx around 1cm. As shown in Figure 3.4, the detected signal is around 1 volt peak to peak with 200mv noise. The low SNR limits the maximum transmission distance. The small vibrations of the table and air flow also change the optical path length and cause the detected signal unstable.

3.2 Characterization of Frequency Multiplier Chain Based 625 GHz Wireless Communication Link

3.2.1 Double Balanced Mixer Characteristics

Figure 3.5 shows the characterization of the double-balanced mixer used in the modulation section. For dc-voltages in the range of the voltage swing of the launched data signal and applied to the intermediate frequency (IF) port of the mixer, the amplitude swing of the output signal is recorded when a 12.933 GHz tone is connected to the local oscillator port of the mixer. A small offset for applied dc-voltage between -5 mV and +5 mV can be observed.

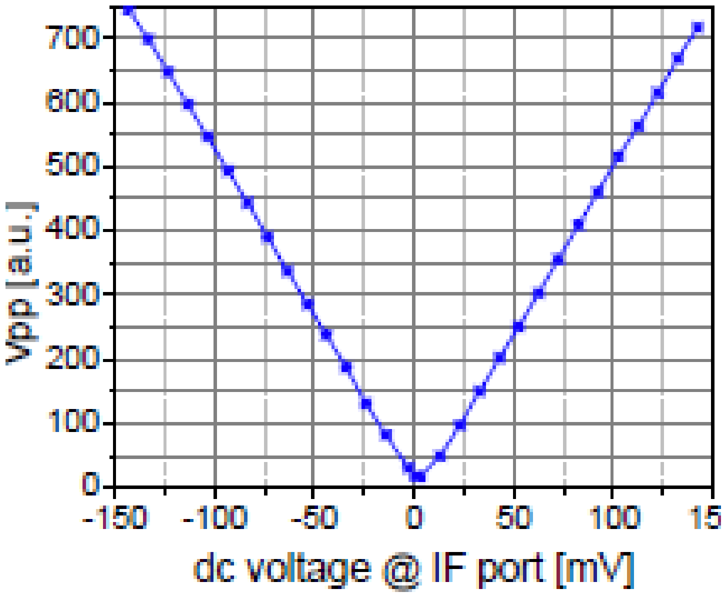

Figure 3.5 Double balanced mixer characteristics.

3.2.2 Power Transfer Function Measurement

As discussed in Chapter 2, for the 625GHz communication link, the receiver horn is connected to a zero biased Schottky diode, which functions in the low power regime (input power <10 μW) as square law detector with large baseband bandwidth, meaning that the detector's output voltage is proportional to its incident power measure in watts. The responsitivity of the detector is about 2500 V/W at 600 GHz. The "power transfer function" of the current system is characterized by sweeping the input frequency of the THz source across its acceptance band and the output voltage of the Schottky diode is also recorded. Figure 3.6 indicates a pass band that is impaired with a ~4 dB dip and 1 dB ripples. These ripples cause group delay variations across the filter passband and amplitude fluctuations, which together with the limited bandwidth make this source less suitable for signal modulation with a comparable wide spectrum (direct 2.5 Gb/s non-return-to-zero (NRZ)). Also Figure 3.6 indicates the optimal frequency position of the carrier at 12.933 GHz (corresponding to T-rays frequency at ~625 GHz) where best system performance is achieved.

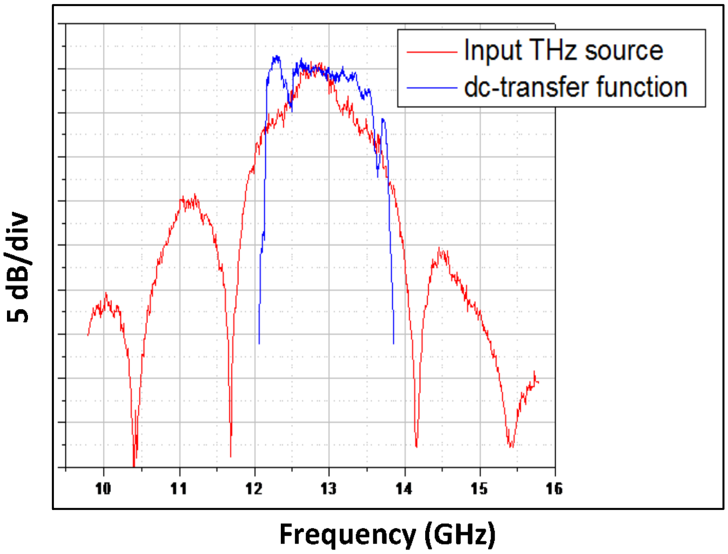

Figure 3.6 Power transfer function of system and spectrum of data signal at THz source input.

3.2.3 Performance of Duobinary Modulation Technique

Pre-coding the data reduces the signal bandwidth but keeps its payload the same, thus the aforementioned filter impairments affect the signal performance less. The performance of the duobinary modulation technique is shown in Figure. 3.7.

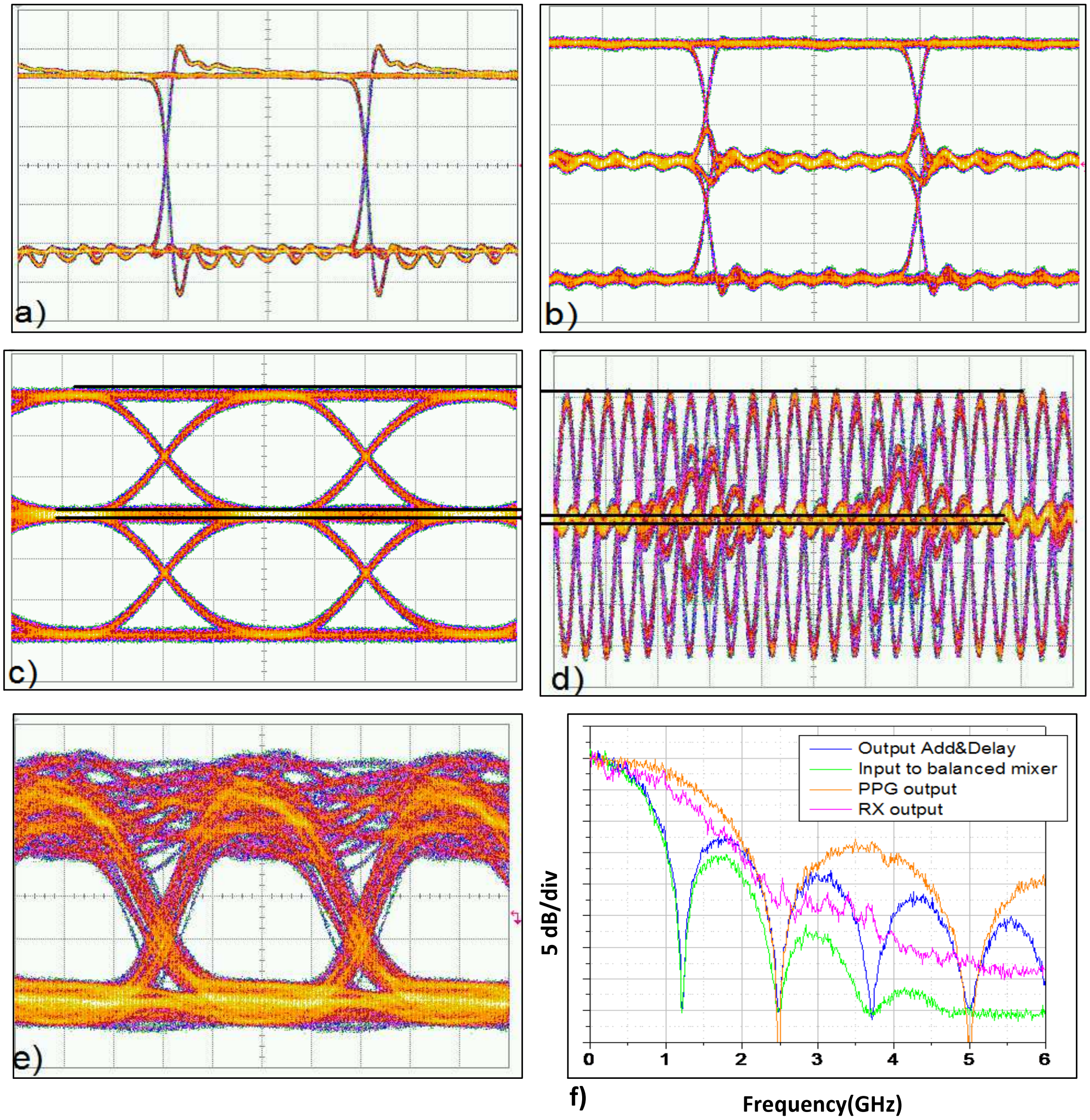

Figure 3.7 Eye diagrams at 100 ps/div (a) output PPG, (b) output add & delay filter, (c) after low pass filter (LPF1), (d) input to THz source (carrier @12.5 GHz), (e) output Rx LPF, and (f) corresponding signal spectra.

Figure 3.7a shows the 2.5 Gb/s NRZ signal produced by the pulse pattern generator (PPG). After NRZ signal gets split into two branches, with one branch delayed by 400 ps and then combined, the resulting signal (Figure 3.7b) possesses three amplitude levels (-1, 0, 1) and an advantageous phase coding, which significantly shrinks its bandwidth compared to its corresponding NRZ format. Figure 3.7c shows the signal waveform after a Gaussian low pass filter, which indicates the signal spectrum reduced further, mainly by cutting off its tail (Figure 3.7f). The almost rectangular NRZ eye at the PPG output and its converted three level version, which is ‘smoothed’ by the Gaussian filter but without introducing inter-symbol interference (ISI), drive a balanced mixer as the baseband signal to imprint its data on a carrier at a frequency accordingly to the acceptance band of the THz source. It is a specific feature of the balanced mixer that negative amplitudes of the driving signal result in a 180 degree phase shift of the carrier. A high-speed scope can conveniently be triggered to visualize the output of the balanced mixer as an eye diagram when the product of carrier frequency and bit duration equals an integer. Therefore, the eye diagram is recorded at 12.5 GHz carrier frequency, which is close to the operation frequency of 12.933 GHz, where the system best performs (Figure 3.7d). Both, frequency synthesizer and PPG are coupled to a 10 MHz reference tone to achieve synchronization. The center level of the eye appears to be broadened compared with the mixer input, which can be explained by the small offset of the mixer transfer function at 0 volt input (Figure 3.5). The eye diagrams (Figure 3.7e) for the carrier frequency that gives best system performance and spectra including those of the receiver output (Figure 3.7f) are recorded under ideal measurement conditions (ultra wideband sampling scope, high resolution electrical spectrum analyzer, negligible noise) and also to visualize signal distortions stemming from bandwidth reduction, system non-linearities, and filter effects.

3.2.4 Performance Analysis of Detected Signal

Power decay of the THz beam caused by longer propagation distances in air reduces the signal performance on the receiver side and leads to an increasing BER. In a real system several effects can contribute to such power decrease. However here the power decay is emulated by reducing the detected T-ray power with an iris inserted concentrically into beam to limit its effective diameter (Figure 2.5). The total receiver output power is measured with a RF power meter while we record the corresponding BER with and without threshold optimization (Figure 3.8). After optimizing the data decision threshold at a BER of about 1x 10^{-3} (BER level that can be reduced to ~1 x 10^{-15} by forward error correction coding with 7% overhead used in lightwave transmission systems[76]) increasing of the detected THz power leads to smaller BER up to 2.5 x 10^{-7} where further power enhancement does not reduce the error count (noise floor) for long PRBS (2^{31}-1). In case of threshold adjustment error-free operation is achieved at power levels above -14dBm at same pattern length. The impact of the PRBS length is investigated by performing similar BER measurements with shorter patterns. For this the data is directly triggered with the PPG clock in order to avoid artifacts caused by the clock recovery when driven with long PRBSs. Short PRBS do not show noise floors as exemplifies with a 2^7-1 pattern in both cases with and without decision threshold adjustment. A reason for this could be saturation effects of the receiver Schottky diode and bandwidth limitations of the receiver amplifiers. The clock recovery did not further degrade the system performance.

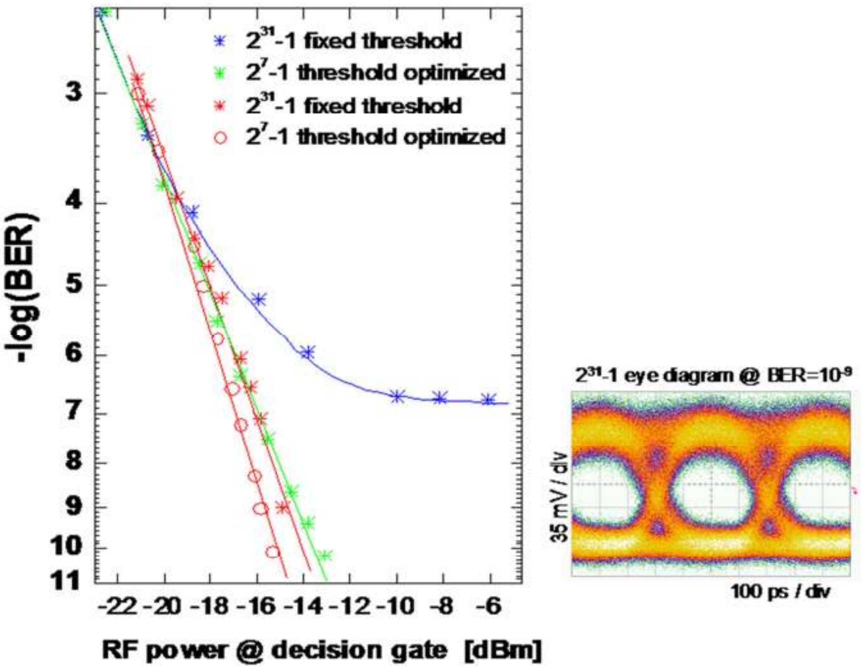

Figure 3.8 Bit error curves for long and short PRBSs with and without decision threshold optimization. Eye diagram at decision gate input.

3.2.5 Signal-To-Noise Ratio (SNR) Measurement

In order to determine the signal-to-noise ratio (SNR) a short and periodically repeated PRBS (2^7-1, 2^{15}-1) data is modulated and then measured with a high resolution electrical spectrum analyzer. The noise level at the Rx amplifier output is measured as well. The noise level is about 18 dB above the intrinsic noise floor of the electrical spectrum analyzer (ESA) and independent of the launched THz power. The total receiver noise was measured with a RF power meter to ~-36.4 dB. The obtained error rates are in fair agreement with the theoretical amounts expected for bipolar coding if vertical eye closure as visible in Figure 3.7e is accounted for in the calculation. The internal pre-amp of the 12.5 Gb/s bit error rate tester (BERT) does not significantly add noise to the data signal.

3.3 Characterization of IR Wireless Communication System at 1.5 µm

Figure 3.9 shows for the IR link the BER performance versus the received input power for same PRBSs and a typical eye diagram at the input to the decision gate. As before the decision threshold was optimized at BER =10^{-6}.

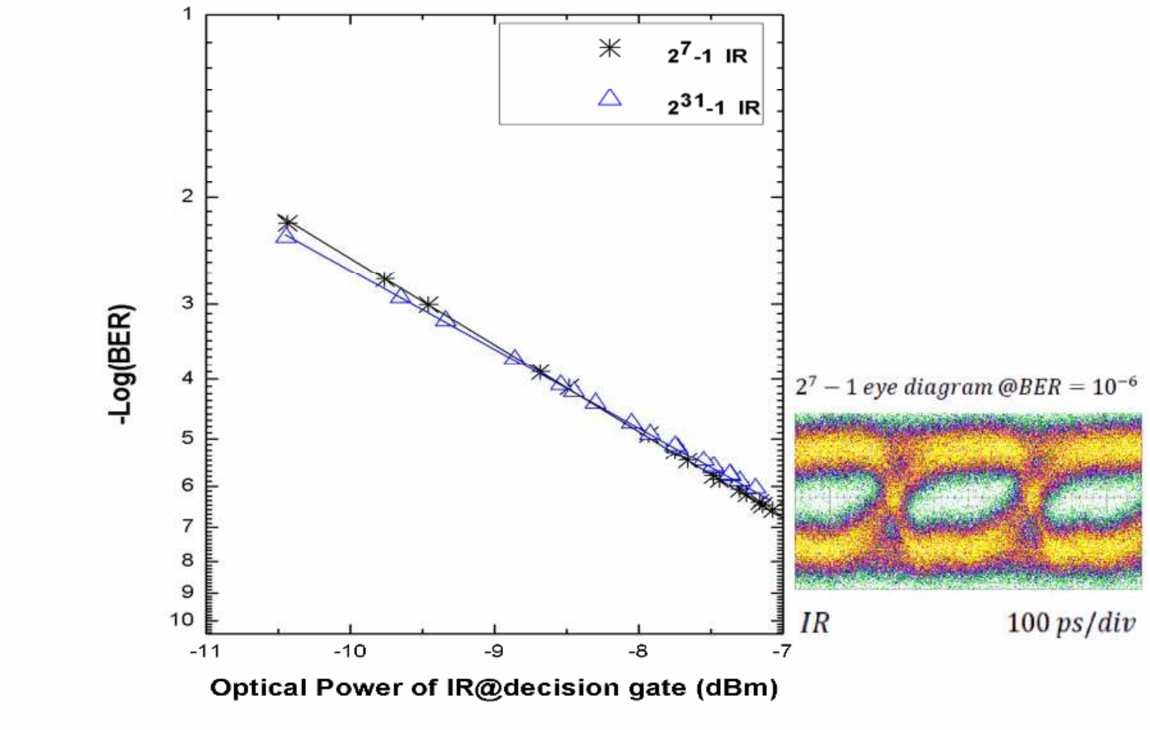

Figure 3.9 IR BER curves for long and short PRBSs with fixed decision threshold optimized at BER=10^{-6}.

CHAPTER 4

COMPARISON OF PERFORMANCE DEGRADATION FROM TERAHERTZ AND INFRARED WIRELESS LINKS IN FOG

Since weather conditions such as fog exhibit a spectral dependence in the atmospheric attenuation, the corresponding impact on THz in comparison with IR communications are not equivalent. At frequencies below 1000 GHz, the size of fog particles is considerably smaller than the carrier wavelength, so that the Rayleigh scattering can be applied to replace the much more complicated Mie scattering theory [77]. The attenuation by fog can be modeled using a simple double-Debye model for the dielectric permittivity of water [78], based on the total liquid water content. In the IR range, this is no longer true and the distribution of the particle size must be considered. Assuming that the particle size distributions follow the Deirmendjian modified gamma function [79], models such MODTRAN [80], LOWTRAN [81] and FASCOD [82, 83] can be applied in the IR range to perform the full Mie calculation scattering for some known particle size distributions. For a more practical approach, one could use visibility data to predict specific attenuation using the empirical models, such as the Kruse [84], Kim [85] and Naboulsi [86] models. In this chapter, simulation results of attenuation by fog in the millimeter and sub-millimeter waveband (from 0.1 to 1 THz) and infrared waveband (1.5 μm) are presented and compared. An IR beam at 1.5 μm wavelength carrying the same data load is superposed with the THz beam. After propagating through the same weather conditions (fog), performance of both channels are analyzed and compared.

4.1 Fog Introduction

Fog is a collection of suspended water droplet or ice crystals near the Earth's surface that leads to a reduction of horizontal visibility below 1 km [87]. Fog normally can form when the air becomes nearly saturated with water (relative humidity close to 100%) and water vapor produce condensation around nuclei in the air (assuming sufficient condensation nuclei are present in the air).

Fog can be characterized by several physical parameters, such as visibility, water content (g/m^3), and drop size distribution. Several types of fog can be distinguished depending on how the cooling induced the condensation occurred, but generally advection fog and radiation fog are most encountered [88]. Advection fog is usually coastal fog which forms when warm, moist air moves over colder surface (tropical air encounters cooler waters). The diameter of the drop size is close to 20 μm and the liquid water content is higher than 0.20 g/m^3. Radiation fog forms inland, which is generated by the cooling of land by thermal radiation until the air temperature approaches the dew point. Its liquid water content varies between 0.01 and 0.1 g/m^3 and particle diameter is around 4 μm.

In the lab environment, in order to compare propagation properties as measured by different regions of the electromagnetic spectrum, the artificial fog is generated by dripping liquid Nitrogen into a cup filled with hot water (temperature about ~80°C) which is placed inside the fog chamber containing the propagating IR and THz beams. In order to duplicate more closely naturally fogs, no condensation nuclei were added, the steam condensing on the nuclei normally present in the air. The only apparent difference between artificial fog produced in this manner and natural fog is the sized of the fog droplets, the artificial fog being composed of somewhat smaller particle of more uniform size [89].

The droplet sizes of the fog particles are measured using the microscope. The fog droplets are collected on slides covered with a thin layer of mineral oil. If the oil is properly saturated with water, the evaporation of the drops can be prevented and the drops will retain their spherical shape [90]. It suggests an average diameter of the fog drops in a range of 8 μm. Better photographic contrast can be obtained if a proper dark field illuminator is used [90].

4.2 Fog Attenuation and Scattering Mechanisms

4.2.1 Fog Attenuation

Atmospheric attenuation is also called extinction, defined as the process whereby some or all the energy of an electromagnetic wave is lost (absorbed and/or scattered) when traversing the atmosphere. According to the Beer's-Lambert Law [91], the attenuation of laser radiation through the atmosphere can be expressed as:

$$\tau(\lambda, R) = \frac{P(\lambda, R)}{P(\lambda, 0)} = e^{-\gamma(\lambda)R} \tag{4.1}$$

where R is transmission distance, $\tau(\lambda, R)$ is total transmittance of the atmosphere at the wavelength λ, $P(\lambda, R)$ is optical power at the distance R, $P(\lambda, 0)$ is initial emitted optical power, and $\gamma(\lambda)$ is attenuation or the total extinction coefficient (per unit of length). The total extinction coefficient $\gamma(\lambda)$ is composed of two parts: absorption term and scattering term and can be expressed as:

$$\gamma(\lambda) = \alpha(\lambda) + \beta(\lambda) = \alpha_m(\lambda) + \alpha_p(\lambda) + \beta_m(\lambda) + \beta_p(\lambda) \tag{4.2}$$

where $\alpha(\lambda)$ is absorption coefficient, $\beta(\lambda)$ is scattering coefficient, and the subscripts m and p designate the molecular and aerosol processes, respectively.

The absorption and scattering can be expressed in terms of the absorption and scattering cross section (σ_a and σ_s , respectively) of the individual particles that are involved:

$$\alpha = \sigma_a N_a \tag{4.3}$$

$$\beta = \sigma_s N_s \tag{4.4}$$

where N_a and N_s are the concentrations of the absorbers and scatterers, respectively.

Fog droplets in the atmosphere can be considered as approximately spheres with a complex refractive index, which is also temperature dependent. In both THz region (625 GHz) and Infrared region (1.5 µm), the contributions of absorption to the total attenuation coefficient are very small, while the effects of scattering dominate the total attenuation coefficient [92].

4.2.2 Scattering Mechanism

The type of scattering is determined by the size of the specific particle with respect to the transmission wavelength and can be divided into three domains based on a dimensionless size parameter α which is defined as:

$$a = \frac{2\pi r}{\lambda} \tag{4.5}$$

where r is radius of the particle, $2\pi r$ is the circumference of the particle and λ is the wavelength of incident radiation. Based on the value of a, those domains are [93]:

- If $a \ll 1$ (particle size is much smaller than the wavelength), Rayleigh scattering will be applied in this case.
- If $a \approx 1$ (particle size is comparable in size to the wavelength), Mie scattering will fit in this case. Generally, the size parameter varies between 0.1 and 50 during Mie scattering [93].
- If $a \gg 1$ (particle size is much larger than the wavelength of light), geometric scattering (nonselective scattering) is appropriate in this case.

Table 4.1 Typical Fog Droplets with Radius, and Corresponding Size Parameter for Wavelengths of 480 µm and 1.5 µm

Particle Type	Radius (µm)	Size Parameter a	
		625GHz (480 µm)	1.5 µm
Fog droplet	1~20	0.013-0.261	4.18~83.73

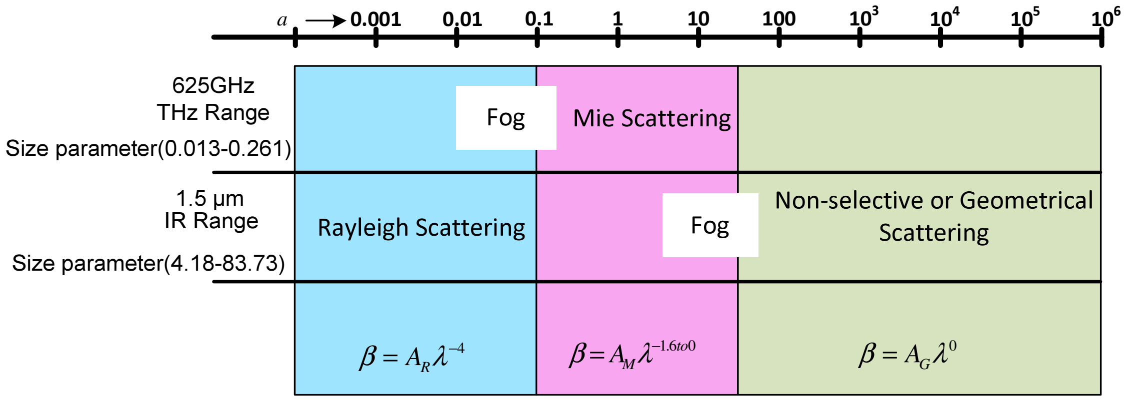

Figure 4.1 (a) Size parameter distribution of fog particles for wavelength of 480 µm (625 GHz) and 1.5 µm and the corresponding regions for Rayleigh, Mie, and non-selective or geometrical scattering. β is scattering coefficient, A_M, A_R, A_C are constants, λ is wavelength.

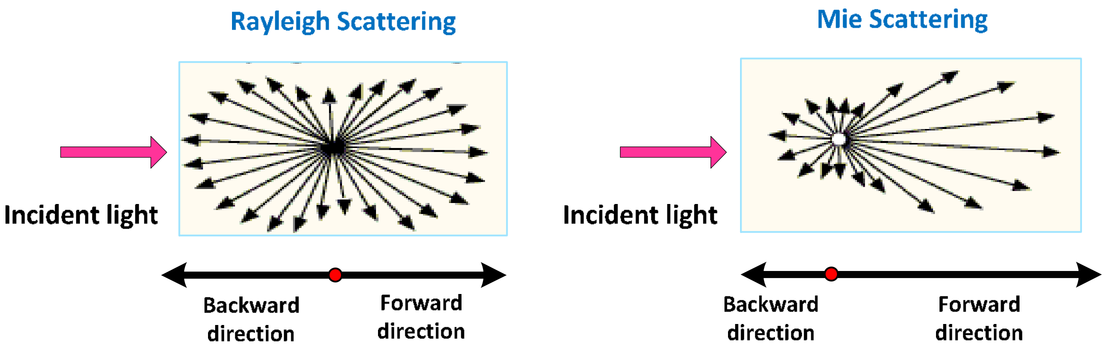

Figure 4.1 (b) Isotropic scattering (Rayleigh scattering) and forward scattering (Mie scattering).

Table 4.1 shows the radius of the fog droplet and their corresponding size parameter for laser for wavelengths of 480 µm (625 GHz) in the terahertz range and 1.5 µm in the IR range. Figure 4.1 (a) shows the size parameter distribution of fog particles for THz and IR and corresponding regions for different scattering types. For the 625 GHz, the Rayleigh scattering occurs primarily of the fog particles in the atmosphere. The radiation from Rayleigh scattering is equally divided between forward and back scattering (as shown in Figure 4.1 (b)). The attenuation coefficient varies as λ^{-4}. For the laser wavelengths of 1.5 µm (IR range), the scattering of radiation becomes more dominant in the forward direction as opposed to the backward direction (as shown in Figure 4.1 (b)). Mie scattering is not strongly wavelength dependent and the exponent in the power law dependence on wavelength for the attenuation coefficient varies from 1.6 to 0 [94].

4.3 Scintillation Effects on the THz and IR Communication Link

There are three primary atmospheric process that affect optical wave outdoor propagations: absorption, scattering and refractive-index fluctuation (optical turbulence).

Absorption and scattering by the gases and particulates of the atmosphere give rise primarily to attenuation of the laser beam, which are introduced in Section 4.2. In the following section, scintillation effects will be introduced.

With regard to communications, scintillation is defined as a random intensity fluctuation on the received field strength caused by irregular changes in the transmission path over time [46]. The strength variation of an optical signal as it travels through air derives from small fluctuations (optical turbulence) in the index of refraction along the optical path. The atmospheric turbulence arises when air parcels of different temperatures are mixed by wind and convection. The individual air parcels, or turbulence cells, break up into smaller cells and eventually lose their identity. In the meantime, however, the mixing produces fluctuation in the density and therefore in the refractive index of air [95].

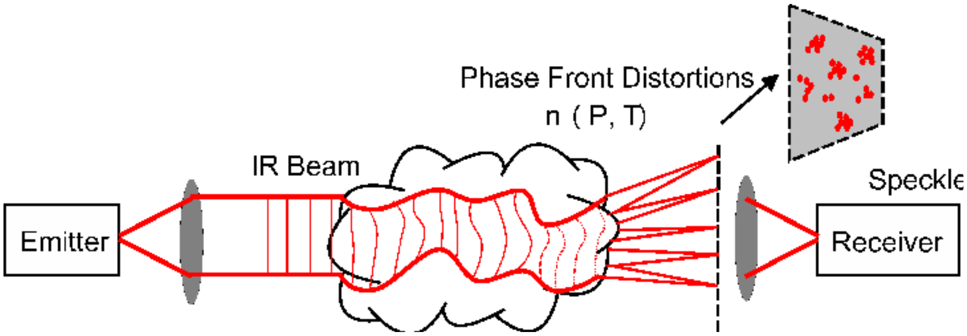

Figure 4.2 Air turbulence causes refractive index fluctuations resulting into speckle (intensity variations at receiver) that limits the reach of IR systems.
Source: [16]

The fluctuations of the real refractive index through the path of a beam can cause random deflection and interference between different portions of the wavefront and destroy the flat phase front of an IR light beam when it passes through a few kilometers of air. Even if a single local refractive index fluctuation only slightly distort the wave’s phase front, the effect can accumulate over a few kilometers of propagation distance resulting into a complete or almost complete destruction of the phase front. As a consequence, on the receiver side the beam cross section appears as a speckle pattern (Figure 4.2) with huge local and temporal intensity variations preventing detection of constant signal power. After passing through fog, low clouds, and direct sunlight, scintillation of the carrier wave is the factor that causes most significant performance deterioration of an optical wireless link. Because of the constantly changing pattern, scintillation appears to be more significant when the receiver has s small aperture.

As will be shown below, THz beams are much less susceptible to scintillation compared to IR beams. The index of refraction value in the atmosphere depends on temperature, pressure, and humidity of air and on the temperature, pressure, and humidity of air and on the wavelength used for the transmission. The refraction index of air in the millimeter wave band up to a few hundred GHz can be well approximated as function of temperature and pressure by [96]:

$$n_{mmW} \approx 1+\frac{7.76}{T}\left[P_a + 4810\frac{P_v}{T}\right]\times10^{-6} \tag{4.6}$$

where T, P_a, P_v stand for the temperature in Kelvin, the atmospheric pressure in kPa, and the water vapor pressure in kPa, respectively. Similarly, for IR wavelengths the refraction index of air can be written as[95]:

$$n_{IR} \approx 1+7.76\times10^{-6}\left[1+7.52\times10^{-3}\lambda^{-2})\right]\frac{P_a}{T} \cong 1+7.76\times10^{-6}\frac{P_a}{T} \tag{4.7}$$

where λ stands for the wavelength in µm. The formula does not consider humidity as it only insignificantly degrades IR propagation. Under the assumption of relevant air parameters a numerical comparison of both formulas shows that even at high levels of water vapor pressure the refraction index changes in both the THz and IR bands are comparable. Since scintillation effects are driven by variations in phase, the relevant parameter is the variation in the optical path length relative to the electromagnetic wavelength. Since the variation in the optical path length for both the IR and THz are comparable (the changes in refractive index are commensurate), the relative magnitudes of the phase variations are predominately determined by the electromagnetic wavelength. The wavelength of THz at ~200 GHz is approximately 1000 times longer than the wavelength of 1.5 µm light. In summary, while time-varying fluctuations in the real refractive index of the atmospheric path leads to scintillation effects in wireless communications, these effects are smaller for THz compared to IR wireless links [16].

4.4 Millimeter Wave Attenuation Due to Fog

For the fog particles, generally less than 20 µm, the Rayleigh approximation is valid for the frequency range between 10 GHz and 1000 GHz. To calculate propagation effects, the Rayleigh scattering approximation can be applied to replace the much more complicated Mie scattering theory.

4.4.1 Double-Debye Model

The attenuation by fog from 10 to 1000 GHz can be calculated using a simple double-Debye model for the dielectric permittivity of water based on the total liquid water content, developed by Liebe [78] and adopted by the international Telecommunication Union in Recommendation (ITU-R P.840-4) [97, 98].

When the Rayleigh scattering approximation is valid, the specific attenuation within fog can be written as:

$$\gamma_c = K_l w \tag{4.8}$$

$$K_l = \frac{0.819 f}{\varepsilon''(1+\eta^2)} \tag{4.9}$$

$$\eta = \frac{2+\varepsilon'}{\varepsilon''} \tag{4.10}$$

where γ_c is specific attenuation (dB/km) in the fog, K_l is specific attenuation coefficient (dBkm^{-1}g^{-1}m^3), w is liquid water density (g/m^3). The liquid water density in fog is typically about 0.05 g/m^3 for medium fog (visibility of the order of 300 m) and 0.5 g/m^3 for thick fog (visibility of the order of 50 m). In the above equation f is the frequency(GHz), ε' and ε'' are the real and image part of the complex dielectric permittivity of water which can be computed with double-Debye model:

$$\varepsilon''(f) = \frac{f(\varepsilon_0-\varepsilon_1)}{f_p[1+(f/f_p)^2]} + \frac{f(\varepsilon_1-\varepsilon_2)}{f_s[1+(f/f_s)^2]} \tag{4.11}$$

$$\varepsilon'(f) = \frac{\varepsilon_0-\varepsilon_1}{[1+(f/f_p)^2]} + \frac{\varepsilon_1-\varepsilon_2}{[1+(f/f_s)^2]} + \varepsilon_2 \tag{4.12}$$

with three permittivity constants given by,

$$\varepsilon_0(T) = 77.6 + 103.3(\theta-1) \tag{4.13}$$

$$\varepsilon_1 = 5.48 \tag{4.14}$$

$$\varepsilon_2 = 3.51 \tag{4.15}$$

The relative inverse temperature variable θ can be expressed as,

$$\theta = 300 / T \tag{4.16}$$

with T representing the temperature (K). The principal and secondary relaxation frequencies are:

$$f_p(T) = 20.09 - 142(\theta - 1) + 294(\theta - 1)^2 \tag{4.17}$$

and

$$f_s(T) = 590 - 1500(\theta - 1) \tag{4.18}$$

In summary, (4.8)-(4.18) represent the propagation model for the fog droplets from 10 to 1000 GHz.

4.4.2 Simulation Results

The fog attenuation from 10 GHz to 1000 GHz at several temperatures are evaluated by Rayleigh approximation and displayed in Figure 4.3(a). Figure 4.3(b) is in the logarithmic scale. Selected numerical values of the attenuation are listed in Table 4.2.

Table 4.2 Double-Debye Model Predication of Attenuation for Frequency Up to 1000 GHz, Water Content: w=1g/m^3

Frequency (GHz)	γ_c **(T=-20℃) (dB/km)**	γ_c **(T=-10℃) (dB/km)**	γ_c **(T=0℃) (dB/km)**	γ_c **(T=10℃) (dB/km)**	γ_c **(T=20℃) (dB/km)**
300	11.0843	12.4123	13.9210	15.1108	15.7974
400	14.0374	15.8171	17.7635	19.4355	20.6363
500	16.4556	18.8518	21.3424	23.5158	25.1914
800	20.9017	25.1923	29.5697	33.5219	36.8206
1000	22.4296	27.6469	33.0955	38.1767	42.5875

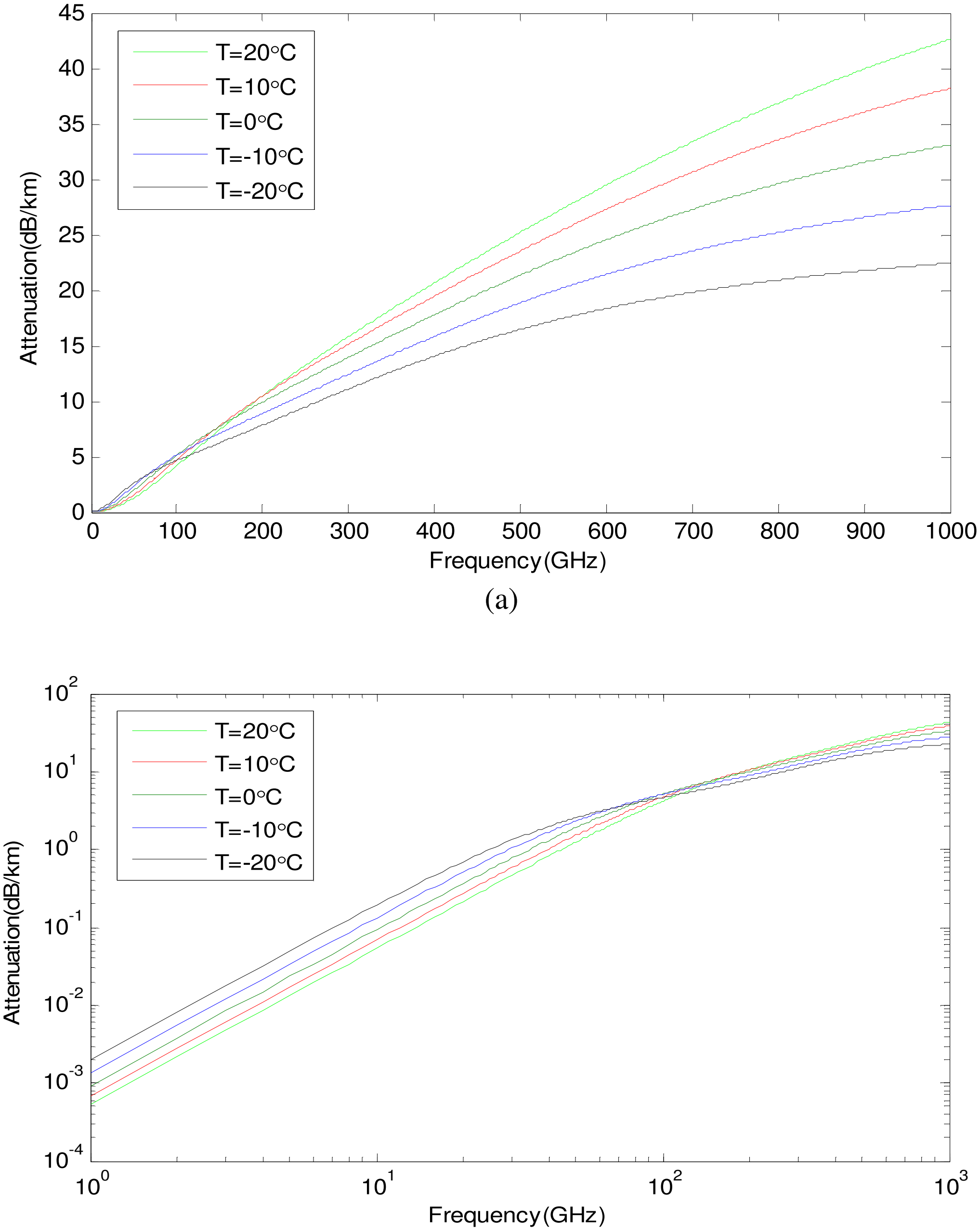

(a)

(b)

Figure 4.3 (a) Double-Debye model predication of attenuation for frequency up to 1000 GHz, water content: w=1g/m^3 and temperature from -20 ℃ to +20 ℃ (b) Logarithmic scale.

4.5 Infrared Wave Attenuation Due to Fog

At infrared wavelengths (λ =1.5 μm), the fog particle size is $r \leq 20$ μm, the size parameter varies between 4.18 and 83.73, which mostly belongs to Mie scattering. The Rayleigh scattering approximation could not fit the IR range.

4.5.1 Full Mie Scattering Calculation: Theoretical Approach

4.5.1.1 Total Extinction Coefficient. According to the Mie Scattering theory, the absorption coefficient $\alpha(\lambda)$ (Equation 4.2) is given by [79, 82, 83]:

$$\alpha(\lambda) = \int_0^\infty Q_a(\frac{2\pi r}{\lambda}, n")\pi r^2 n(r)dr \tag{4.19}$$

where $n"$ is the imaginary part of the refractive index, which represents the absorption part of the particle, λ is the wavelength, $n(r)$ is the particle size distribution, r is the particle radius, Q_a is Mie normalized absorption cross section ($Q_a = C_a / \pi r^2$), C_a is the Mie absorption cross section and $n(r)dr$ is the number of particles per unit within the range from $r + dr$.

The scattering coefficient $\beta(\lambda)$ can be expressed as [79, 83]:

$$\beta(\lambda) = \int_0^\infty Q_d(\frac{2\pi r}{\lambda}, n')\pi r^2 n(r)dr \tag{4.20}$$

where n' is the real part of the refractive index, representing the scattering part of the particle, Q_d is Mie normalized scattering cross section ($Q_d = C_d / \pi r^2$), and C_d is the Mie scattering cross section.

4.5.1.2 Particle Size Distribution. Silverman and Sprague use the Deirmendjian modified gamma distribution [79] to describe the size distribution of the particles, which can be expressed as:

$$n(r) = c \cdot r^{m} \exp(-b \cdot r^{n}) \tag{4.21}$$

where $n(r)$ is the number of the particles per unit volume and per unit increasement of the particle radius r (μm), while m, b and n are parameters that characterize the particle size distribution. The constant c is a normalization constant. For two different types of fog: heavy adventure fog and moderate radiation fog, the typical parameters are given in the Table 4.3.

4.5.1.3 Fog Attenuation. If the particle size distribution, water refractive index and absorption and scattering cross sections are known, the extinction coefficients can be calculated using Equation 4.20 and Equation 4.21 and software modeling code such as FASCOD [82], LOWTRAN [80] and MODTRAN [80].

Table 4.3 DSD Gamma Parameters, Reflectivity Z, LWC and Visibility V of the Considered Four Models of Fog

Type of fog	Model	c	α	b	γ	Z(dBz)	LWC (gm^{-3})	V(km)
Advection	1. strong	0.06592	3	0.3	1	-3.03	0.9	0.02
	2. light	0.027	3	0.375	1	-16.79	0.078	0.089
Radiation	3. strong	2.37305	6	1.5	1	-31.27	0.062	0.146
	4. light	607.5	6	3.0	1	-46.32	0.016	0.352

Figure 4.4a shows the calculated wavelength dependent extinction coefficient in presence advection fog for various values of visibility (100 m, 200 m, 500 m, 800 m) based on FASCOD program.

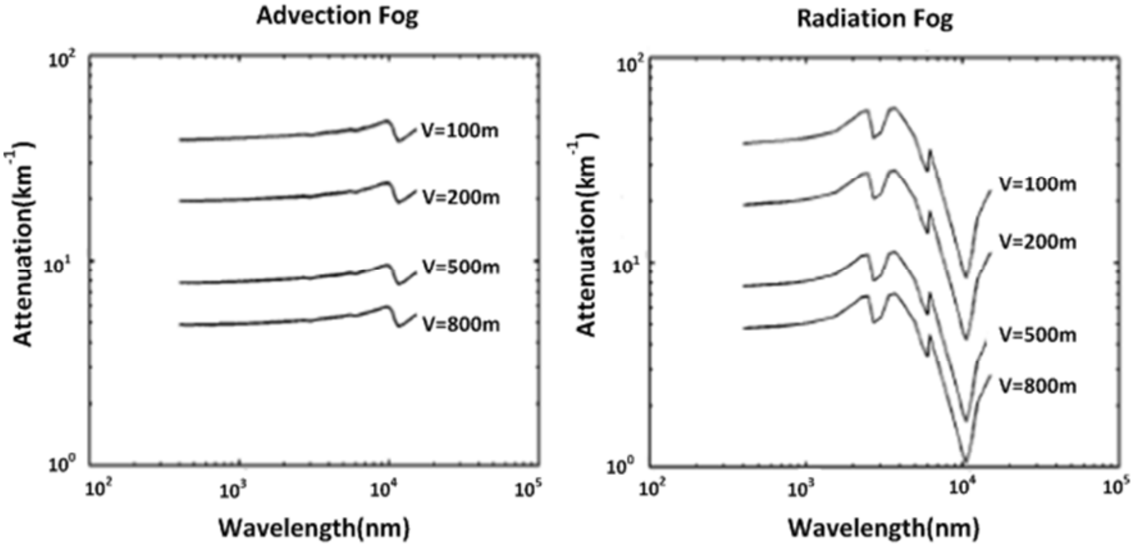

(a) (b)

Figure 4.4 (a) Extinction coefficients versus wavelength for advection fog and various visibility values as derived from FASCOD (b) Extinction coefficients versus wavelength for radiation fog and various visibility values as derived from FASCOD.
Source: [86]

4.5.2 Empirical Approach

4.5.2.1 Principles of Kruse, Kim and Al Nabulsi Models. Since the scattering particle size distribution is not readily available in many cases, determining the attenuation coefficient using Full Mie scattering calculations is not very practical. Several empirical models have been developed to calculate the relationship between the attenuation coefficient and the visibility, such as the Kruse [84], Kim [85] and Al Nabulsi models [86].

The atmospheric visibility is defined as a distance where the 550 nm collimated light beam is attenuated to a fraction (5% or 2%) of original power [84], which can be given by the Koschmieder Law:

$$V = \frac{3.912}{\gamma_{550nm}} \tag{4.22}$$

For both Kruse and Kim model, the attenuation coefficient is approximated by

$$\gamma(\lambda) = \frac{3.912}{V}\left(\frac{\lambda}{550}\right)^{-q} \tag{4.23}$$

where q is depends on the scattering particle size distribution, which can be determined by the experimental data. It is given by the Kruse model:

$$q = \left\{\begin{matrix} 1.6 \\ 1.3 \\ 0.585V^{1/3} \end{matrix}\right\} \begin{matrix} V > 50km \\ 6km < V < 50km \\ V < 6km \end{matrix} \tag{4.24}$$

A new expression for the value of q in Equation 6 for visibility< 6 km, is proposed by the Kim model

$$q = \left\{\begin{matrix} 1.6 \\ 1.3 \\ 0 \\ V - 0.5 \\ 0.16V + 0.34 \end{matrix}\right\} \begin{matrix} V > 50km \\ 6km < V < 50km \\ V < 500m \\ 500m < V < 1km \\ 1km < V < 6km \end{matrix} \tag{4.25}$$

For the Al Naboulsi model, fog attenuation coefficient caused by advection fog is:

$$\gamma(\lambda) = \frac{0.11478\lambda + 3.38367}{V} \tag{4.26}$$

The fog attenuation coefficient caused by radiation fog is:

$$\gamma(\lambda) = \frac{0.18126\lambda^2 + 0.13709\lambda + 3.7502}{V} \tag{4.27}$$

The specific attenuation in dB/km could be calculated by fog attenuation coefficient $\gamma(\lambda)$

$$a_{spec}(dB/km) = \frac{10}{\ln(10)}\gamma(\lambda) \tag{4.28}$$

4.5.3 Simulation Results

Simulations were performed to calculate the fog specific attenuation for 1.5 μm IR radiation. The attenuation predicted by Kruse model is shown in Figure 4.5. Kim model investigated the fog attenuation in detail from 0 m to 6 km and corresponding results are presented in Figure 4.6. Figure 4.7 shows the specific attenuation for radiation fog and advection fog given by Al Naboulsi models. All three plots are in logarithm scale. In order to compare the specific attenuation predicted by the different models, the predicted attenuation using different models is shown in Figure 4.8 with the visibility from 0 to 1 km. The Kim model is more proper for the low visibility, which is the case for current experiments. Kim model is utilized to calculate the specific attenuation versus wavelength for various visibility values shown in Figure 4.9. The simulation result is comparable with the exact Mie theory calculation shown in Figure 4.4.

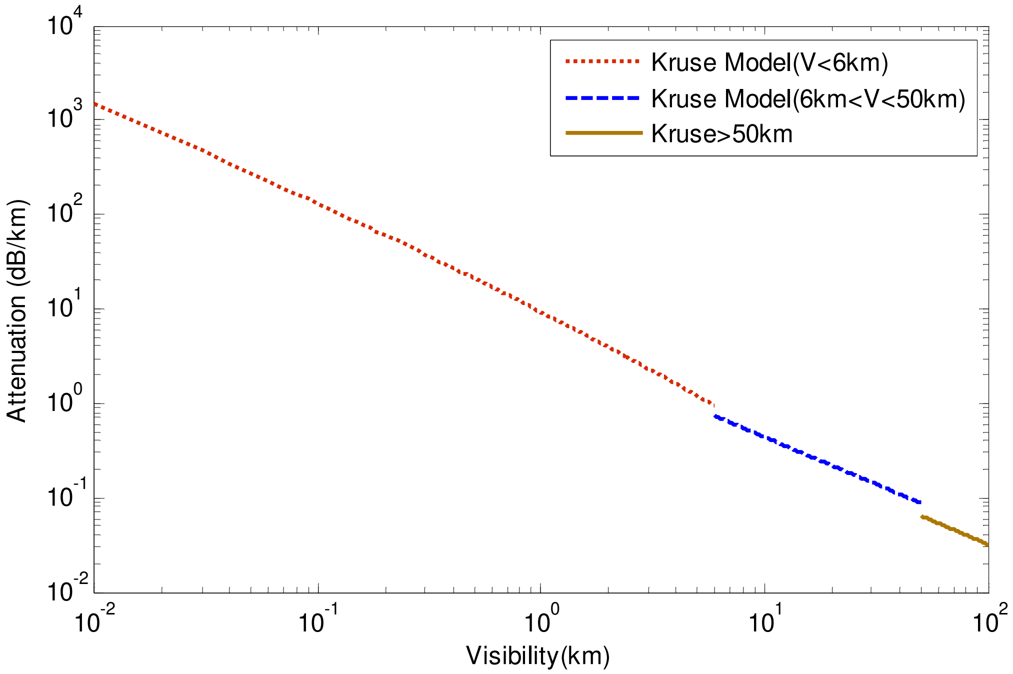

Figure 4.5 Specific attenuation using the Kruse model for 1550 nm wavelength.

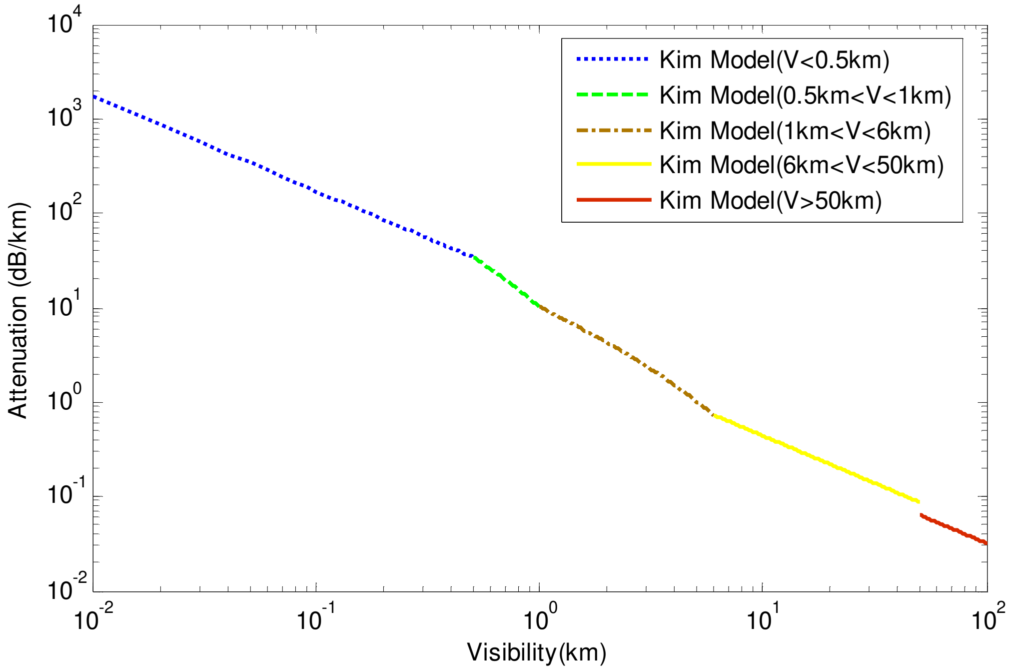

Figure 4.6 Specific attenuation using the Kim model for 1550 nm wavelength.

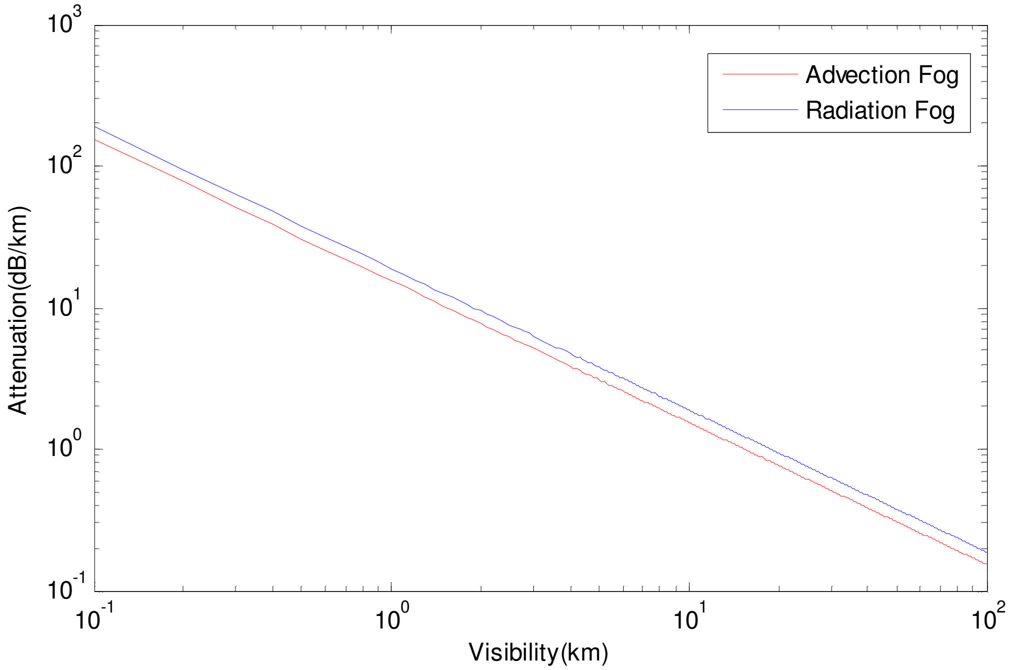

Figure 4.7 Specific attenuation using Al Nabulsi model for 1550 nm wavelength.

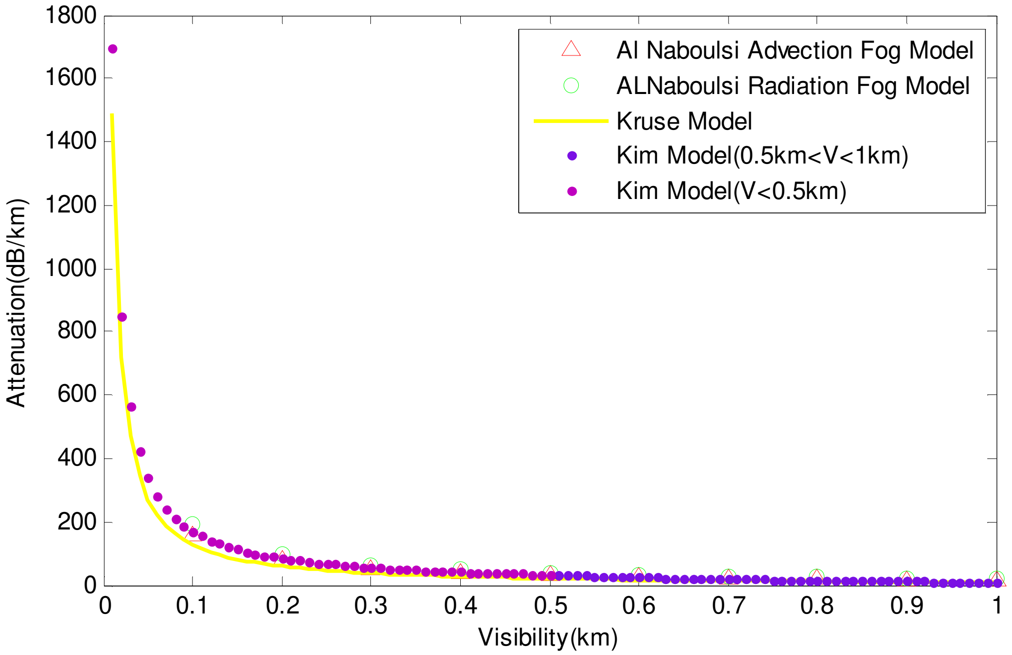

Figure 4.8 Specific attenuation for 1550 nm wavelength predicted by different models.

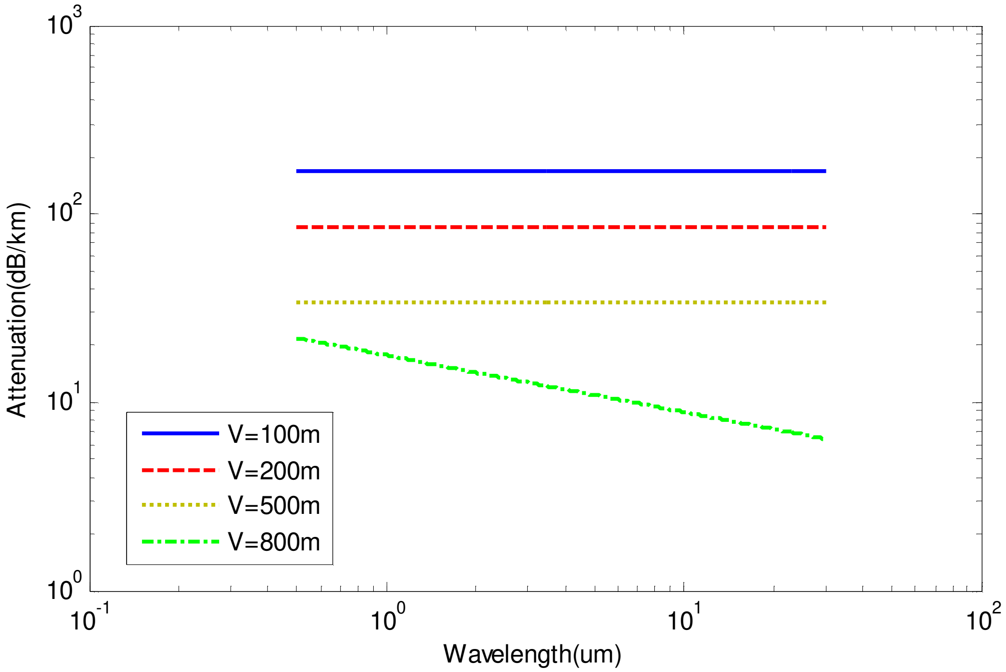

Figure 4.9 Specific attenuation versus wavelength for various visibility values derived from the Kim model.

4.6 Experimental Results

4.6.1 Experimental Setup

An IR beam at 1.5 μm wavelength carrying the same data load as the THz system is superposed with the THz beam, propagating through the same weather conditions (fog) (shown in Figure 4.10). As both beams pass through the same channel perturbations and as their degradations are recorded simultaneously, the weather impact on both channels can be simultaneously analyzed and compared. The block diagram (Figure 4.10) shows the main transmitter and receiver elements of the THz and IR communication links, the optics for combining beams, the fog chamber, data acquisition interfaces, and control loops for IR power stabilization. The features of the THz link followed by some remarks about the IR channel have been explained in Chapter 2 and Chapter 3.

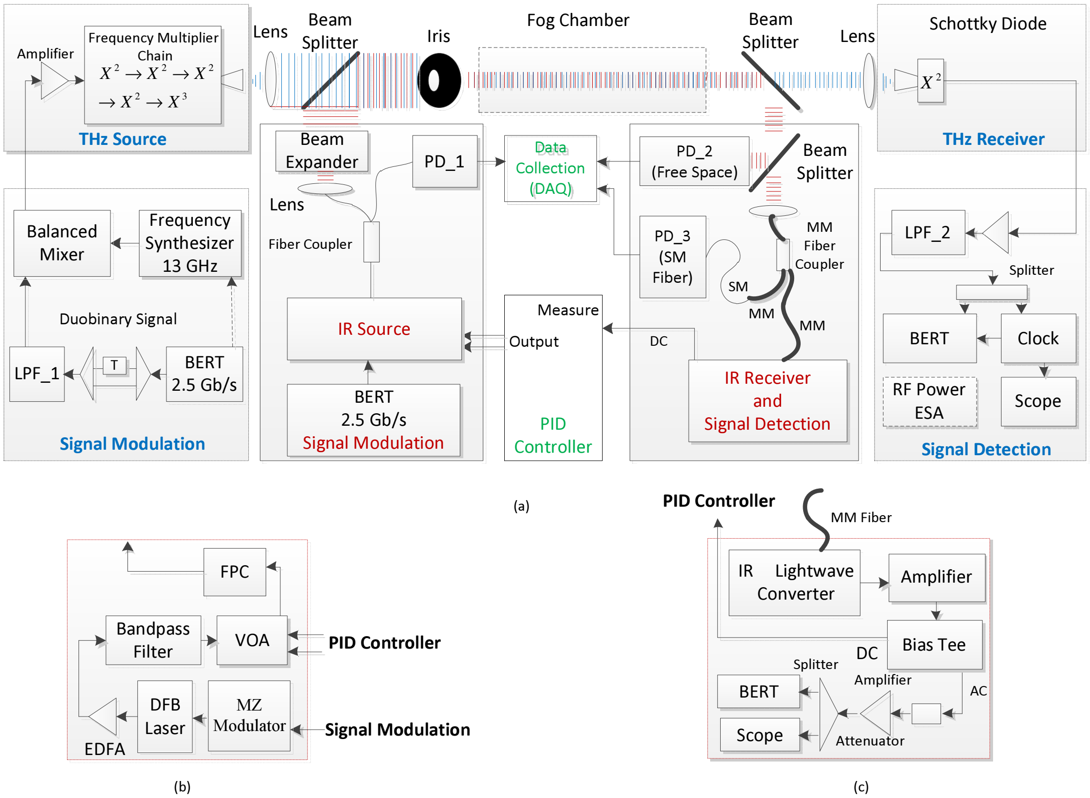

Figure 4.10 (a) Schematic diagram of THz and IR wireless communication link through fog chamber, (b) IR source, (c) IR receiver and signal detection.

4.6.2 Experimental Results

4.6.2.1 Signal Attenuation by Fog. First the transmission links performance is shown with a disabled PID controller. The constant IR power is launched into the chamber. As expected, when fog fume reaches the propagation path of the beams strong attenuation of the IR light is observed while the THz signal exhibits only a minor but measurable decreased in power. A typical evolution of the attenuations in both channels is shown in Figure 4.11(a). The measurement capabilities are limited to about 42 dB dynamic range during certain time intervals, as indicated in Figure 4.11(a). The recording shows the noise floor of the power meter and not the actual IR power level. Clearly there is a huge difference in the IR and THz attenuation. Usually, even ‘small’ amounts of fog are sufficient to block the IR beam after a few seconds of diffusion. When the IR attenuation reaches about 4 dB, the BER measurement of the IR signal collapses in agreement with the receiver performance shown in Figure 4.11(a) and Figure 4.11(b). For the THz channel, a functional relation between the attenuation for both signals and the recorded BERs is clearly visible. After some 10s of second the fog disappears into the lab environment or is converted into humidity thus both links regain or approach their original performance, respectively. The ratio of the IR channel attenuation over the THz channel attenuation (Figure 4.11(c)), both measured in dB, shows a trend to become smaller towards the end of the measurement. However, while one would expect the total attenuation in either channel to change in time as the particle density of the fog decreases in time, one would expect the ration of attenuation coefficients in the IR and THz to be fixed. Likely, over time, the fog is converted into humidity during the recording time. The conversion of fog to humidity impairs the THz signal relatively stronger than the IR signal. This hypothesis is in agreement with Figure 4.11(b) where the THz link towards the end of the measurement maintains a small attenuation while the IR attenuation approaches zero.

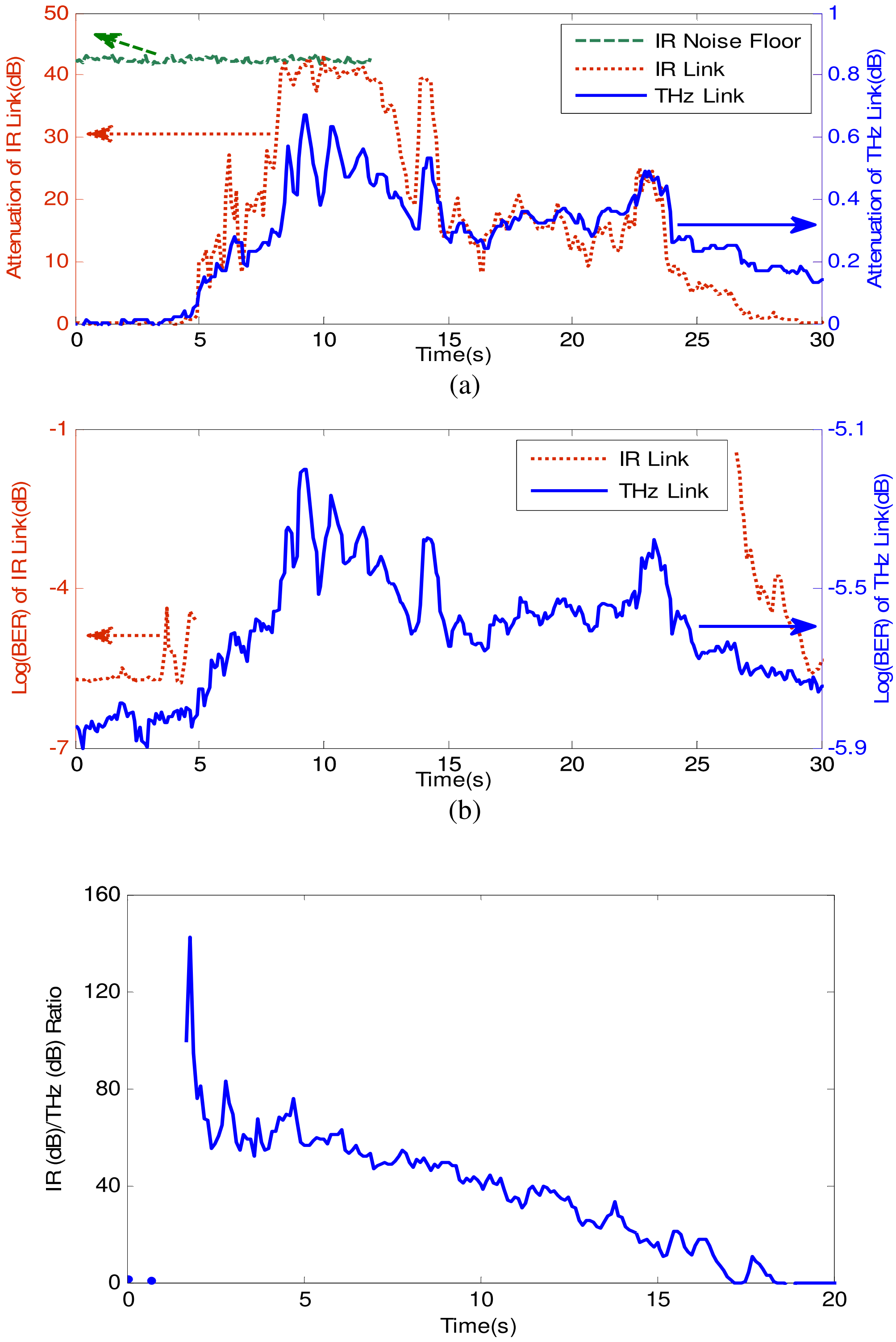

(a)

(b)

(c)

Figure 4.11 (a) Attenuation of THz link and IR link with time (b) Log(BER) of THz link and IR link with time (c) IR attenuation in dB relative to THz attenuation in dB over time.

4.6.2.2 Fog Visibility Characterization. In order to characterize the visibility of fog, the specific attenuation (dB/km) (shown in Figure 4.12) is derived from Figure 4.11(a) since the length of the fog chamber is 1 m. Following the Kim model, the visibility of fog is calculated over time. From Figure 4.6, one can see the maximum specific attenuation Kim model can fit is 1699 dB/km which corresponds to 10 m visibility. Consequently, the dense fog corresponding to visibility below 10 m could not be analyzed here.

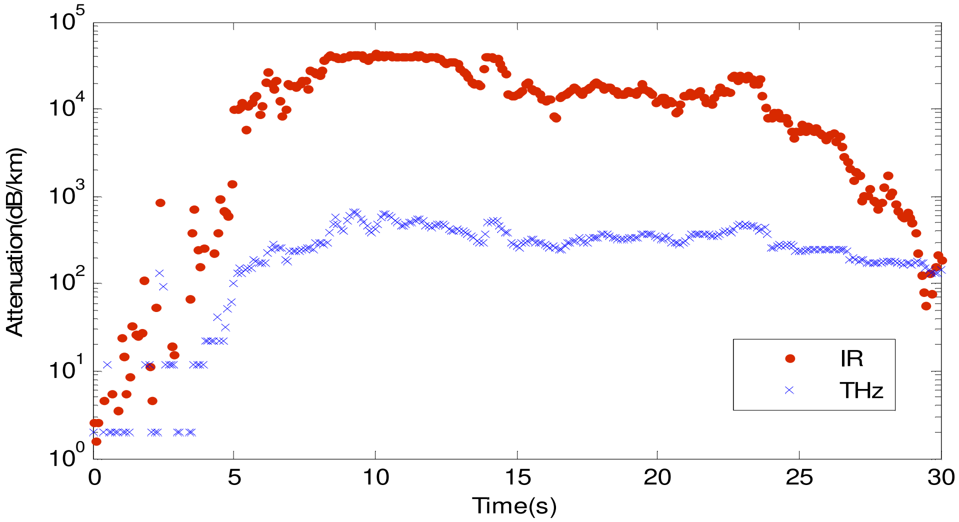

Figure 4.12 Specific Attenuation of THz link and IR link with time (dB/km).

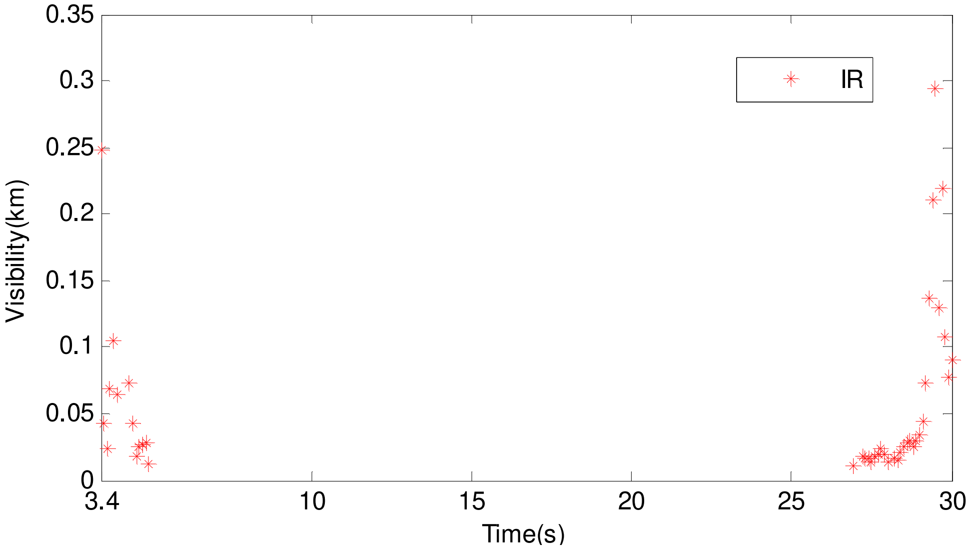

Figure 4.13 Infrared visibility with time calculated by Kim model.

With different visibility, the specific attenuation of THz is calculated by Double-Debye Model and compared with experimental data. (Shown in Table 4.4)

Table 4.4 Comparison of THz Experimental and Theoretical Specific Attenuation at Different Visibility

Visibility (m)	Water Density (g/m^3)	Experimental Specific Attenuation (dB/km)	Theoretical Specific Attenuation (dB/km)
300	0.05	2	1.406
50	0.5	14.06	12
10	1	28.1381	22

4.6.2.3 Scintillation Effects in Fog Chamber. Two effects investigated by fog contribute to the IR power reduction on the receiver side. While attenuation of the IR beam by power decay has been demonstrated above, local refraction index inhomogenities -as discussed below- cause phase front distortions of the optical mode that is coupled into the detector fiber. If the mode of the IR beam was only attenuated in the fog chamber but the phase front was not degraded, then the IR power coupled into the receiver fiber would to a good approximation proportional to the IR power detected by PD-2. However, if phase front distortions of the IR beam were to occur one would expect a smaller coupling efficiency especially into the SSMF with small aperture. In order to simultaneously visualize the effect of phase front distortions on the detection with large and small aperture fibers, the IR signal is coupled into a 1 x 2 multimode power splitter whose output ports are connected to photodetector PD-3 via a SSMF and the aforementioned lightwave converter with multimode fiber input. The goal is to keep the optical power at the data receiver's input constant by means of the PID controller when fog enters the beam so that the BER should not change (constant signal quality). The outputs of all photo detectors are simultaneously recorded along with the BER and transmitter output power of the IR channel (Figure. 4.14). In order to allow an easier overview on the variations of the recorded signals we plot relative changes on a decibel scale. When fog diffuses into the IR beam after about 3s recording time the PID controller enhances the IR power launched into the chamber and measured by photodetector PD-1. Up to about 17s recording time the control loop can compensate the power loss inside the chamber. Thereafter, the maximum transmitter output power is insufficient to further equalize the losses of the link until the link attenuation drops back at about 22s recording time to a level within the power margin of the system. While the detected optical power at the data receiver stays almost constant (for t< 17s) we see small changes of the output of PD-2. Around pointer 'A' these variations are less than 0.15 dB but show that the receiver power and detected power of PD-2 are not always exactly proportional to each other. However, the variations of the power coupled into the SSMF appear more pronounced (up to +/- 2dB). The variations in outputs of both PD-2 and PD-3 indicate that scintillation effects impair the IR beam. The fog and humidity impact on the THz signal is generally small while visualization of possible scintillation effects in the THz beam is below the measurement precision. Small kinks in the received power of the data receiver (pointer 'B') could be caused by rapidly changing signal attenuation and noise which affects the stable operation of the PID controller for short time. Interestingly, at pointer 'C' and 'D' the chamber attenuation for the IR beam is almost zero whereas the attenuation of the THz signal is about 0.1 dB. Likely, at these recording times fog was converted into humidity which impacts the IR signal comparably less than the THz signal. The RF power meter provides a two digit reading after the comma, which explains the rough quantization of the recorded signal.

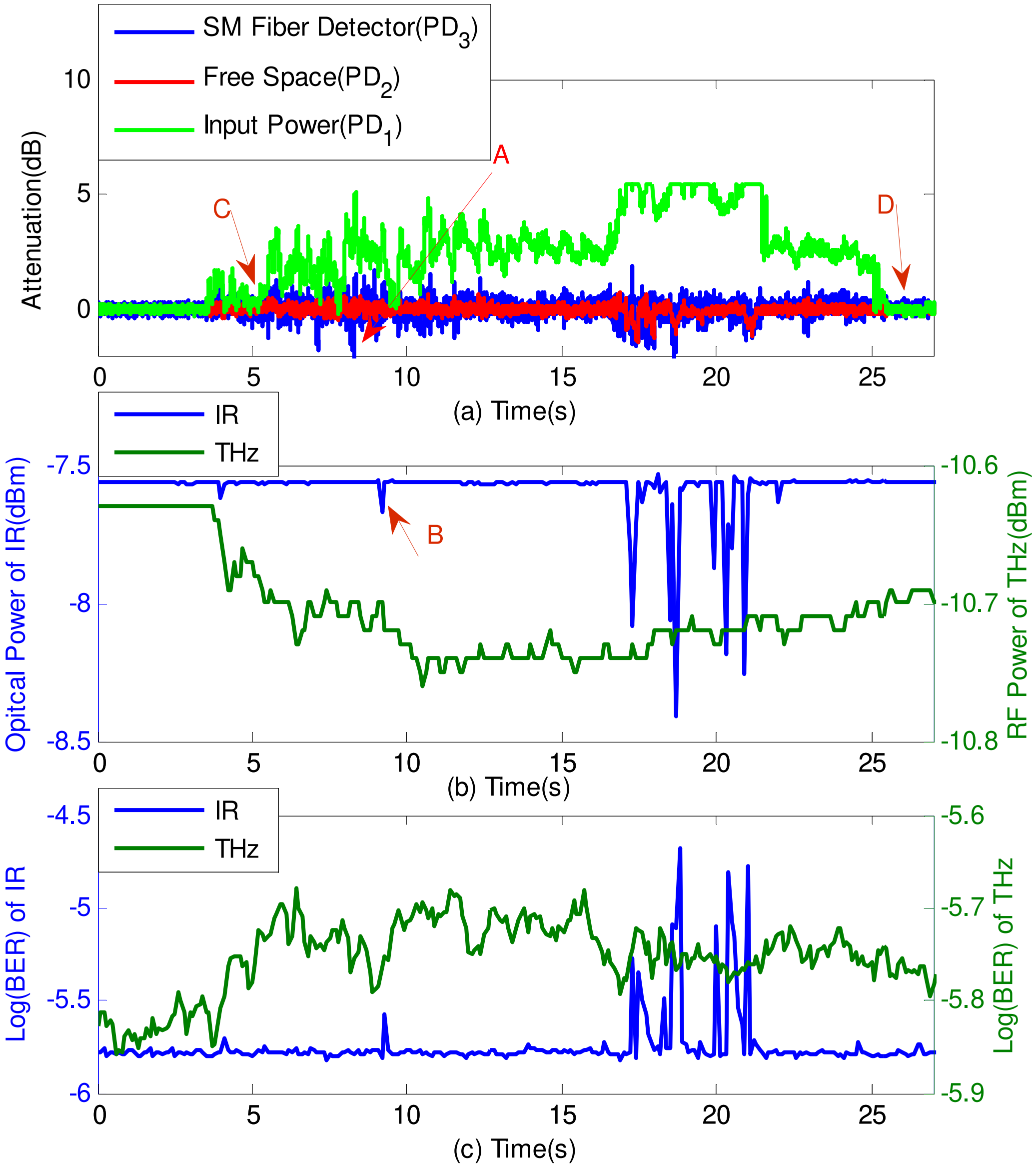

Figure 4.14 (a) Individiually normalized outputs of photodetectors (PD-1, PD-2, PD-3) in dB, (b) Opitcal power of IR and RF power of THz due to fog, (c) Log(BER) of IR and THz links impaired by fog.

CHAPTER 5

COMPARISON OF PERFORMANCE DEGRADATION FROM TERAHERTZ AND INFRARED WIRELESS LINKS IN DUST

Due to the relatively small size of atmospheric particles such as dust and smoke compared to THz wavelength, one would expect minimal THz attenuation due to airborne particulates. Mann had predicted that smoke has little or no effect up to 1 THz [57]. Attenuation caused by scattering strongly increases when the wavelength of the radiation nears the particle size, which explains why dust and pollution can significantly impair IR transmission. Under the dust conditions, IR transmission is considerable better than for fog [99]. Gebhart et al. [47] mentions that for the typical wavelengths employed by wireless IR links (780 nm and 1550 nm), attenuation due to dust is around 10 dB/km in urban regions. On the other hand, the attenuation due to heavy fog can reach values great than 300 dB/km. In this chapter, an IR beam (1.5 μm wavelength) carrying the same data load as the THz beam is superposed with the THz beam (625 GHz), and propagated through the same aerosol conditions (Bentonite particle with mean size of diameter 8.6 μm). Different amounts of dust (0.05 g, 0.08 g and 0.13 g) are loaded in the test chamber to generate a variety of dust concentrations for beam propagation. The optical power attenuation and BER are measured, analyzed and compared. As the dust loading becomes heavier (and extinction increases), the measured attenuation becomes more severe. Under identical dust concentrations, IR wavelengths are strongly attenuated while THz wavelength shows almost no impact. Therefore, THz communications are a better option than IR wireless links in a battle-field or wildfire environments in which large concentrations of airborne particulates would be expected. For some specific link length requirements THz can enable reliable communication as compared to IR-based systems under dust conditions.

5.1 Experimental Methodology

5.1.1 Dust Particle Source Distribution for Bentonite

Bentonite powder, which is the dust particle used in the experiment, is a mixture of clay minerals such as mica, feldspar, quartz and lime. The particle size distribution for Bentonite is measured by laser diffraction (LS) particle size analyzer and the result is shown in Figure 5.1. Table 5.1 shows the calculated size parameters of the Bentonite.

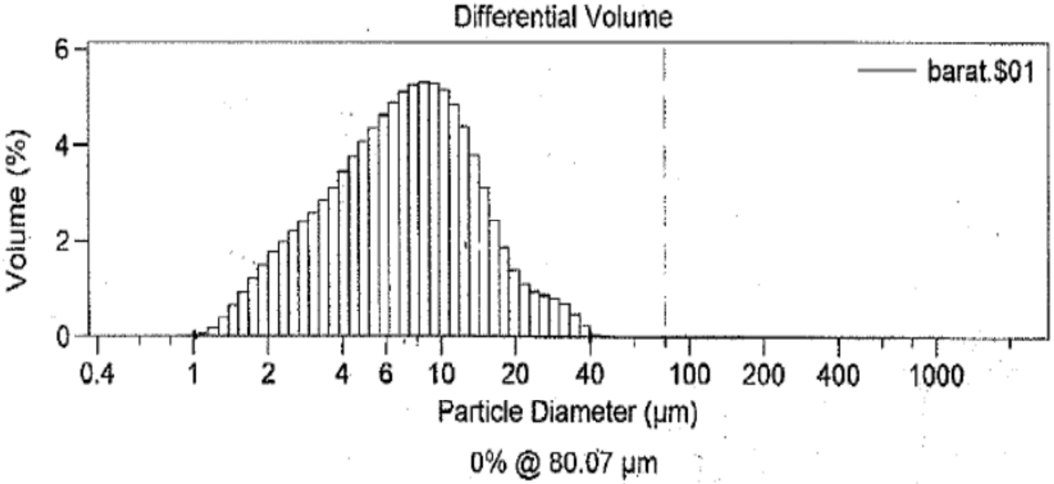

Figure 5.1 Particle size distribution of Bentonite measured by laser diffraction particle size analyzer.

Table 5.1 Bentonite Particle Size Distribution Parameter (calculations from 0.375 µm to 2000 µm)

Mean(µm)	Median(µm)	Mean/Median Ratio(µm)	Variance (µm)
8.613	7.151	1.204	37.87

5.1.2 Dust Chamber Design

The dust chamber is shaped like a cylinder with 12 inch diameter of the bottom and top plate and 12 inch height. Figure 5.2 (a) shows the schematic diagram of dust chamber design and (b) shows real picture of dust chamber design.

The dust is placed inside the hopper, which sits above the dust holder. The electronic pulse switch controls the air valve and the released air removes the dust from the dust holder and ejects it at a high speed into the chamber from the top plate of the dust chamber. The hopper can be easily refilled during operation and it can produce a very constant and reproducible feed of dust.

The air is flowed into the chamber with constant volume speed through the holes from the bottom plate. Holes form 5 concentric set of circles with diameter $\frac{7}{8}, 1\frac{7}{8}, 2\frac{7}{8}, 3\frac{7}{8}, 4\frac{7}{8}$ inches. All the holes maintain the same diameter of $\frac{1}{14}$ inch. The constant air volume flow rates are regulated by the air flow controller to achieve the specific flow rates which are need in the system.

Two Picarin window [100] are utilized in the system since it is highly transparent in both THz and IR ranges. After experiments are completed, the dusty air can be extracted by the exhaust pump which is installed on the top plate.

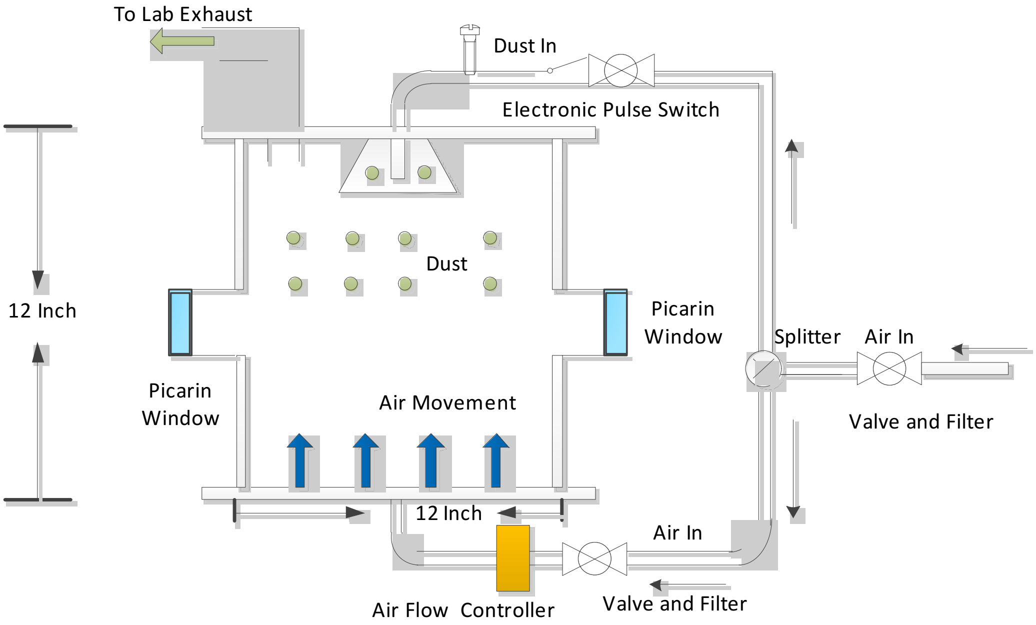

(a)

(b)

Figure 5.2 (a) Schematic diagram of dust chamber design (b) real picture of dust chamber design.

5.1.3 Force Balance Analysis of the Dust Particle

In order to keep the dust elevated in the air as long as possible and make the concentration of the dust maintain constant for a longer time interval, the air volume speed need to be calculated through the force balance theory.

As shown in Figure 5.3, there are three forces applied on the dust particle, gravity, buoyancy and drag. The force balance condition could be expressed as:

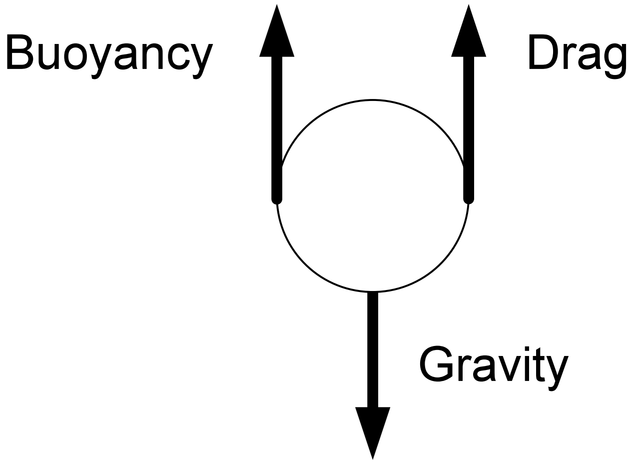

Figure 5.3 Free body diagram of the dust particle.

$$F_{gravity} = F_{buoyancy} + F_{drag} \tag{5.1}$$

The force on a dust particle due to buoyancy is giving by Archimedes' principle[101]: buoyancy is equal to the weight of displace fluid.

$$F_{buoyancy} = m_g g = \rho_g V_p g = m_p \frac{\rho_g}{\rho_p} g \tag{5.2}$$

where m_g is the mass of the gas displaced, g is gravitational acceleration, ρ_g is gas (air) density, V_p is volume of gas, ρ_p is particle density, and m_p is mass of the particle (dust).

The gravity force can be expressed as:

$$F_{gravity} = m_p g \tag{5.3}$$

The drag force (air resistance) could be calculated using:

$$F_{drag} = \frac{C_D (V_g - V_p)^2 \rho_g A}{2} \tag{5.4}$$

where C_D is drag coefficient, V_g is the velocity of gas, V_p is the velocity of the particle, $V_g - V_p$ is the speed of the particle (dust) relative to the gas (air), A is area of the orthographic projection of the object on a plane perpendicular to the direction of motion, for a sphere $A = \pi(\frac{d_p}{2})^2$, where d_p is particle diameter. The drag force can further be expressed as:

$$F_{drag} = \frac{C_D (V_g - V_p)^2 \rho_g {d_p}^2 \pi}{8} \tag{5.5}$$

substituting Equations 5.2, 5.3 and 5.5 into the Equation 5.1. The force balance condition could be rewritten as:

$$m_p g = m_p \frac{\rho_g}{\rho_p} g + \frac{C_D (V_g - V_p)^2 \rho_g {d_p}^2 \pi}{8} \tag{5.6}$$

substituting $V_p = 0$ into the Equation 5.6 and solving the Equation for V_g, which should be the air velocity which could keep particle remains elevated and motionless, yields

$$V_g = \left(\frac{m_p g}{\pi C_D} (1 - \frac{\rho_g}{\rho_p}) \frac{8}{\rho_g {d_p}^2} \right)^{\frac{1}{2}} \tag{5.7}$$

where the density of the Bentonite particles is $\rho_p = 2.7 g / cm^3$,[102] and the average diameter $d_p = 8um = 8 \times 10^{-4} cm$.

The drag coefficient C_D is defined as:

$$C_D = \frac{a}{\mathrm{R}_e^{\ b}} \tag{5.8}$$

where R_e is Reynolds number[103], which is defined as:

$$\mathrm{R}_e = \frac{d_p (V_g - V_p) \rho_g}{\mu_g} \tag{5.9}$$

where μ_g is dynamic viscosity of the gas ($kg / (m \cdot s)$. This value depends mostly on the temperature 300K (26.85 degrees Celsius) and is computed using Sutherland's formula[104]:

$$\mu_g = \mu_0^{\ *} (a / b)^* (T / T_0)^{3/2} \tag{5.10}$$

where $a = 0.555 T_0 + C$, $b = 0.555 T + C$, μ_0 is reference viscosity in centipoise at reference temperature T_0, T_0 is reference temperature in degrees, and C is Sutherland's constant. The dynamic viscosity μ_g can be calculated as:

$$\mu_g = 0.01827 m \cdot Pa \cdot s \frac{0.555 \times 524.07 + 120}{0.555 \times (300 \times \frac{9}{5}) + 120} \times (\frac{300 \times \frac{9}{5}}{524.07})^{\frac{3}{2}} = 0.0187 m \cdot Pa \cdot s \tag{5.11}$$

According to the Reynolds number, there are three regimes, Stocks regimes, Intermediate regimes and Newton's regimes [105] for C_D, shown in Table 5.2.

Table 5.2 Reynolds Numbers for Different Regimes

Reynolds Number	Regime	*a*	*b*
$0 < R_e < 0.4$	Stokes	24	1
$0.4 < R_e < 500$	Intermediate	10	0.5
$R_e > 500$	Newton's	0.43	0.0

In the following sections, the Reynolds number will be calculated to determine the appropriate regime.

5.1.3.1 The Intermediate Range of Reynolds Numbers.

Assuming the drag coefficient C_D is in the intermediate regime:

$$C_D = \frac{a}{R_e^{\,b}} = \frac{10}{R_e^{1/2}} = 10\left(\frac{\mu_g}{d_p V_g \rho_g}\right)^{\frac{1}{2}} \tag{5.12}$$

$$m_p = \frac{\pi d_p^{\,3}}{6}\rho_p \tag{5.13}$$

substituting Equation 5.12 and 5.13 into Equation 5.7 yields

$$V_g = \left[\frac{\pi d_p^{\,3} g \rho_p}{6\pi 10}\left(1-\frac{\rho_g}{\rho_p}\right)\frac{8}{\rho_g d_p^{\,2}}\left(\frac{d_p V_g \rho_g}{\mu}\right)^{\frac{1}{2}}\right]^{\frac{1}{2}} \tag{5.14}$$

V_g can be solved from Equation 5.14:

$$V_g = 0.26\frac{d_p\left[g\left(\rho_p - \rho_g\right)\right]^{\frac{2}{3}}}{(u\rho_g)^{\frac{1}{3}}}$$

$$= 0.26 * \frac{8*10^{-4}cm\left[9.8m/s^2\left(2.7-1.169*10^{-3}g/cm^3\right)\right]^{\frac{2}{3}}}{(1.87*10^{-5}kg/ms*1.169*10^{-3}g/cm^3)^{\frac{1}{3}}} = 6.618cm/s \tag{5.15}$$

substituting Equation 5.15 to 5.9 gives a Reynolds number value of

$$R_e = \frac{d_p v_g \rho_g}{\mu} = \frac{8*10^{-4} cm * 6.618 \frac{cm}{s} * 1.169*10^{-3} g/cm^3}{0.02 g/ms} = 0.03 \tag{5.16}$$

The calculated value of the R_e should be in the Stoke's regime, which is conflict with the assumption (intermediate regime).

5.1.3.2 Is Newton's Regime Appropriate? Assuming that the drag coefficient C_D is in the Newton's regime:

$$C_D = \frac{a}{R_e^{\ b}} = 0.43 \tag{5.17}$$

$$V_g = 3.1 \left[\frac{d_p g \left(\rho_p - \rho_g \right)}{\rho_g} \right]^{\frac{1}{2}}$$

$$= 3.1 \left[\frac{8*10^{-4} cm 9.8 m/s^2 (2.7 - 1.169*10^{-3}) g/cm^3}{1.169*10^{-3} g/cm^3} \right]^{\frac{1}{2}} = 131.886 cm/s \tag{5.18}$$

substituting Equation 5.18 into Equation 5.9,

$$R_e = \frac{d_p v_g \rho_g}{\mu} = \frac{8*10^{-4} cm * 131.886 \frac{cm}{s} * 1.169*10^{-3} g/cm^3}{0.02 g/ms} = 0.59 \tag{5.19}$$

R_e is in the Stoke's regime, which shows that the assumption of Newton's regime is incorrect.

5.1.3.3 Is the Reynolds Number in the Stoke's Regime? Assuming that the drag coefficient C_D is in the Stoke's regime:

$$C_D = \frac{a}{R_e^{\ b}} = \frac{24}{R_e} \tag{5.20}$$

$$V_g = \frac{d_p^{\ 2} g}{18\mu}\left(\rho_p - \rho_g\right) = \frac{64*10^{-8} cm^2 9.8 m/s^2}{18*0.02 g/ms}(2.7 - 1.169*10^{-3}) g/cm^3 = 0.47 cm/s \tag{5.21}$$

$$R_e = \frac{d_p v_g \rho_g}{\mu} = \frac{8*10^{-4} cm * 0.47 \frac{cm}{s} * 1.169*10^{-3} g/cm^3}{0.02 g/ms} = 0.002 \tag{5.22}$$

Note that this value for Reynolds number is in the Stoke's regime, clearly, the choice of the drag coefficient and corresponding Reynolds number are consistent.

5.1.3.4 Volumetric Flow Rate Calculation. The volumetric flow Q_g rate is kept constant in the whole system:

$$Q = A * v_g = \frac{\pi d_c^{\ 2}}{4} v_g = \frac{\frac{\pi\, ft^2}{4} 0.47 cm}{s}$$

$$= \frac{0.47 \times 3.14 \times 30.5^2}{4} cm^3/s = \frac{0.47 \times 3.14 \times 30.5^{2?} \times 60}{4 \times 10^3} lit/min == 20.59 lit/min \tag{5.23}$$

where $d_c = 12$ inches is diameter of the dust chamber cylinder.

From the calculation, one can conclude that in order to keep the dust elevated and motionless as long as possible and maintain an approximately constant dust concentration, the gas flow rate should keep 20.59 lit/min.

5.1.4 Experiment Setup

As shown in Figure 5.4, the schematic diagram of THz and IR wireless communication link through dust chamber is same with the fog link (in Chapter 4) except that the fog chamber is replaced by the dust chamber. Also, for the fog chamber, picarin is used as the transmission window material instead of the polyethylene foil, because the air flow noise will cause vibrations of the beam splitter film, which consequently will generate background noise of the collected data. The features of the THz link followed by some remarks about the IR channel have been explained in Chapter 2.

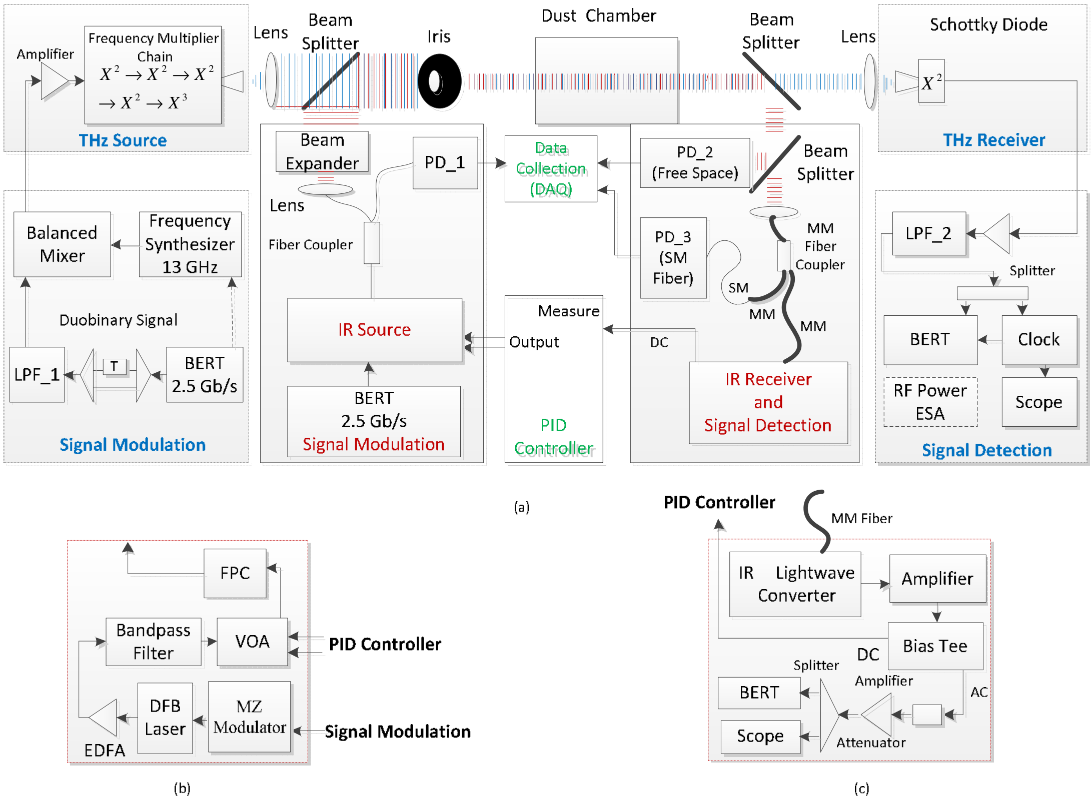

Figure 5.4 (a) Schematic diagram of THz and IR wireless communication link through dust chamber, (b) IR source, (c) IR receiver and signal detection.

5.2 Mie Scattering Theory

A rough estimate of the attenuation can be made assuming that the particulates act as spherical Mie scattering centers. Following a simple Mie scattering formalism [106] that was used previously to study attenuation of THz radiation due to particle grains [106], one can estimate the attenuation at IR, THz and sub-THz frequencies using known particles sizes and concentrations. The extinction coefficient takes on the following form:

$$\gamma_{th}(v) = N\frac{c^2}{2\pi v}\sum_{m=1}^{\infty}(2m+1)\,\mathrm{Re}(a_m + b_m) \tag{5.24}$$

where N is number of grains per unit volume, which will vary greatly depending on the method of dust production processes, c is the speed of light and a_m, b_m are coefficient of the infinite summation such that,

$$\begin{aligned} a_m &= \frac{\psi'_m(y)\psi_m(x) - n\psi_m(y)\psi'_m(x)}{\psi'_m(y)\zeta_m(x) - n\psi_m(y)\zeta'_m(x)} \\ b_m &= \frac{n\psi'_m(y)\psi_m(x) - \psi_m(y)\psi'_m(x)}{n\psi'_m(y)\zeta_m(x) - \psi_m(y)\zeta'_m(x)} \end{aligned} \tag{5.25}$$

where

$$\begin{aligned} \psi_m(z) &= zj_m(z) \\ \zeta_m(z) &= zh_m^{(2)}(z) \end{aligned} \tag{5.26}$$

here $j_m(z)$ and $h_m^{(2)}(z)$ are spherical Bessel functions of the first kind and third kind [107], respectively. The parameter z can be either $x = \frac{2\pi v r}{c}$ or $y = \frac{2\pi v r}{c}$, where r is the radius of the spherical particle and n is the frequency independent refractive index of the particle. And the extinction coefficient $u_{th}(v)$ here takes into account both the intrinsic absorption of the materials as well as extrinsic losses involving single scattering events. As an example, attenuation due to the battlefield particles can be estimated using Equations 5.24, 5.25 and 5.26. For the calculation, parameters used are particle density: $N = 5\times10^6\,/\,cc$, particle radius $r = 0.2\mu m$ and a real index of refraction: 1.5. The size parameter for the THz range (0-3THz) is from (0~0.012) and for IR range (0.6 μm~100 μm) is from (0.012~2.09). Figure 5.5 shows that IR wavelengths are strongly attenuated while THz wavelengths would enable communications.

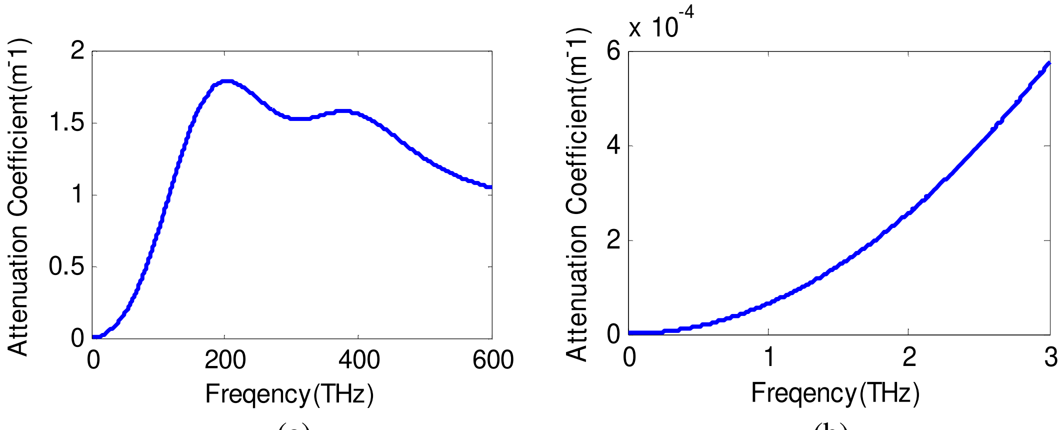

(a) (b)

Figure 5.5 (a) Predicted IR attenuation due to spherical airborne particles, (b) Predicted THz attenuation due to spherical airborne particles.

5.3 Experimental Results

Three different amounts of dusts (0.05 g, 0.08 g and 0.13 g) are loaded in the dust chamber. For each amount, three trials have been done to verify the reproducibility of the experimental results.

5.3.1 0.05 g of Dust

5.3.1.1 Transmission Link Performance with Disabled PID Controller. With a disabled PID controller, constant IR power is launched into the dust chamber. Figure 5.6 (a) shows the normalized signals detected by free space detector (PD-2), (b) shows the single mode fiber signal (PD-3), (c) shows optical power of incoming IR signal, and (d) shows Log(BER) signal detected by the BERT. Signal (a) and (b) are recorded by a Data Acquisition card (DAQ) and signal (c) and (d) are collected via GPIB. The results showed good repeatability of all three trials, which ensure the accuracy and reliability of each experiment.

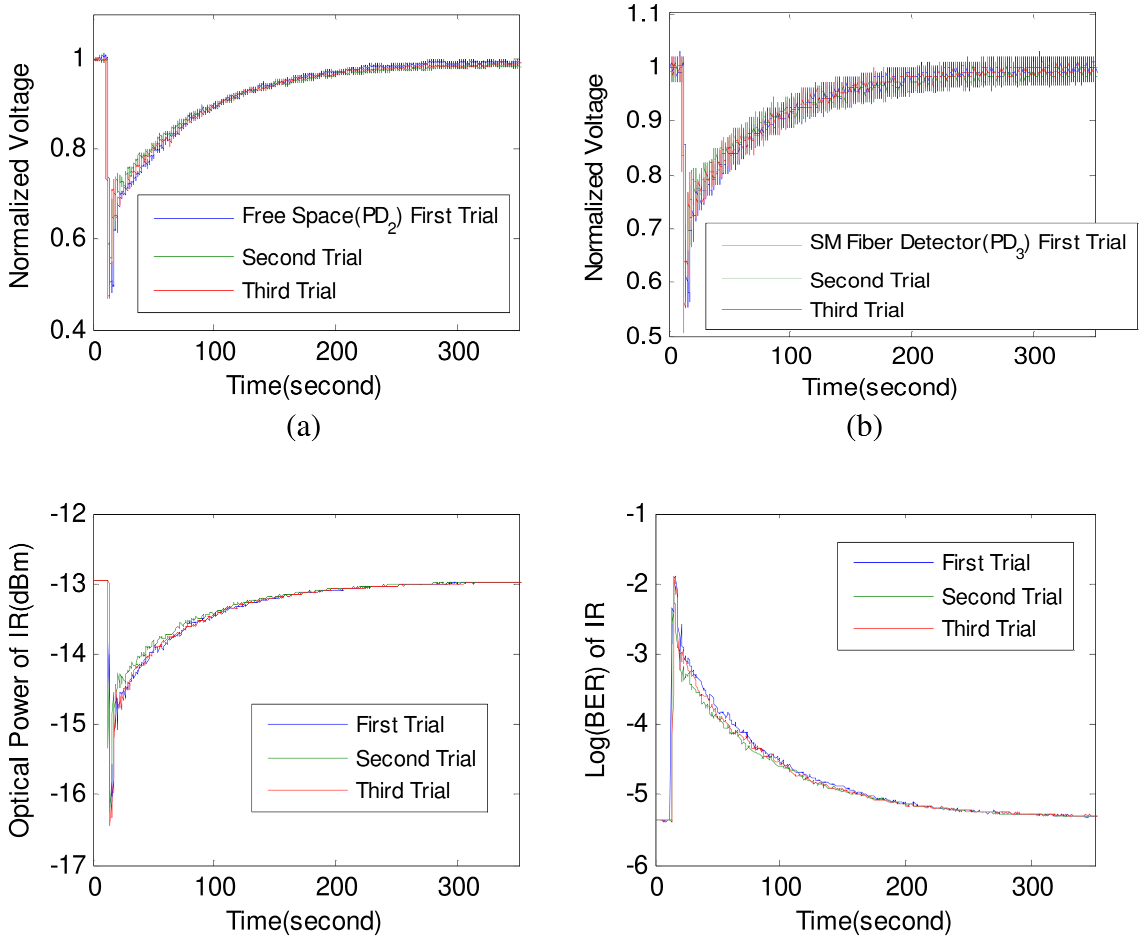

(a) (b) (c) (d)

Figure 5.6 Detected IR signal for the 0.05gram dust (a) Free Space (PD-2) (b) SM Fiber Detector (PD-3) (c) Optical Power of IR(dBm), (d) Log(BER) of IR.

A typical evolution of the attenuations in both THz and IR channels is shown in Figure 5.7 (a). As expected, when dust is launched in the propagation path of the beams, the attenuation (around 1.8 dB) of the IR light is visible while the impact on THz could be neglected. The IR signal collapses in agreement with the receiver performance shown in Figure 5.7 (b) and record BERs of THz in Figure 5.7 (b) verify again that the dust effects on THz is negligible. After 350 seconds almost all the dust particles have fallen down to the bottom of the chamber thus both links regain and approach their original performance, respectively.

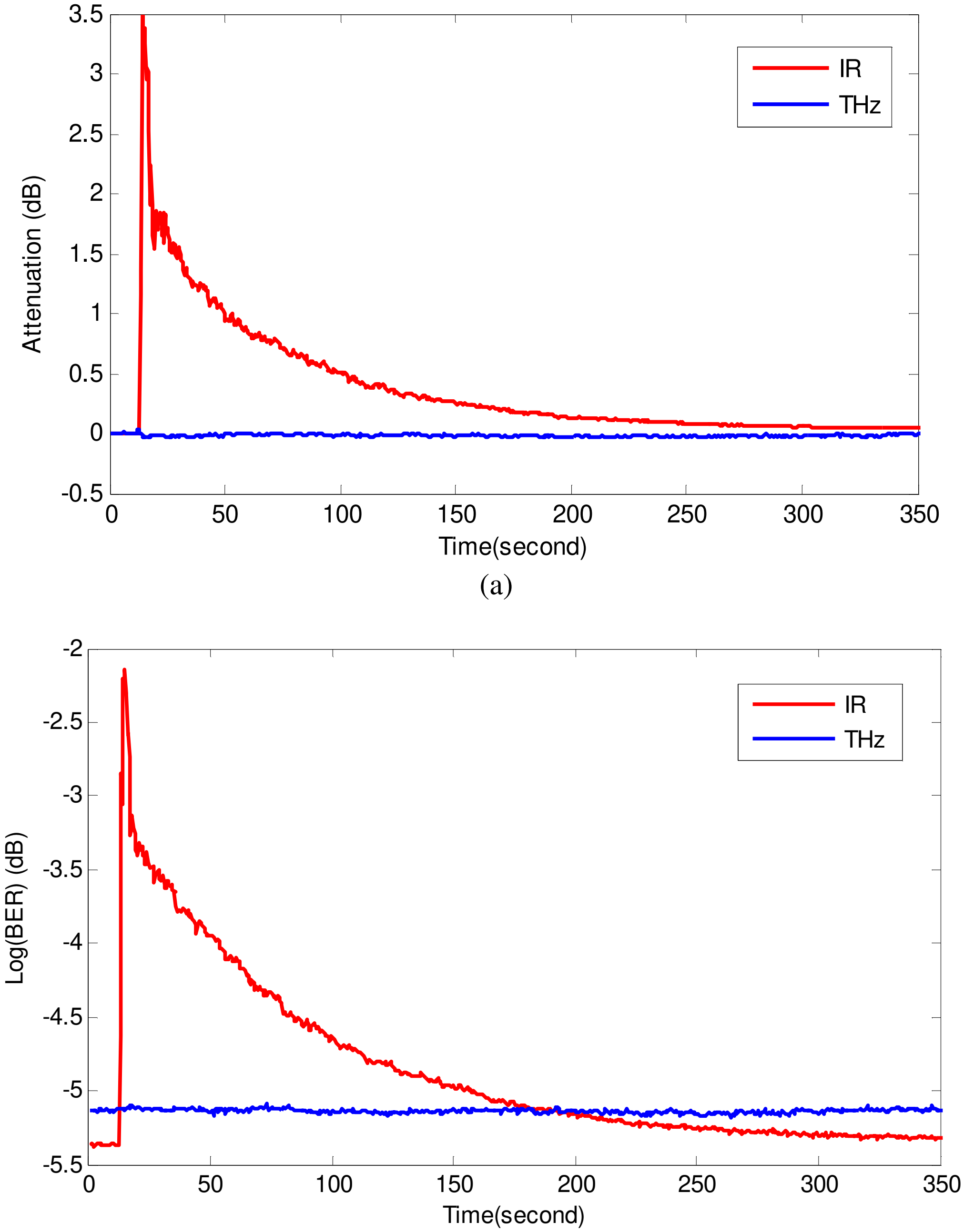

(a)

(b)

Figure 5.7 (a) Attenuation of THz link and IR link with time (b) Log(BER) of THz link and IR link with time.

One can observe a sharp peak in Figure 5.7 (a) with the attenuation around 3.5 dB at 14.4 seconds. This is generated by the fast vibration of the beam split film duo to the sharp noise of the dust release shutter, which could not be counted as the real attenuation due to dust. This sharp peak also appears in Figure 5.6 at the 14.4 seconds. To prove this, the data is recorded when the shutter is released without launching dust into the chamber. Clearly, there is a peak around 13.86 seconds.

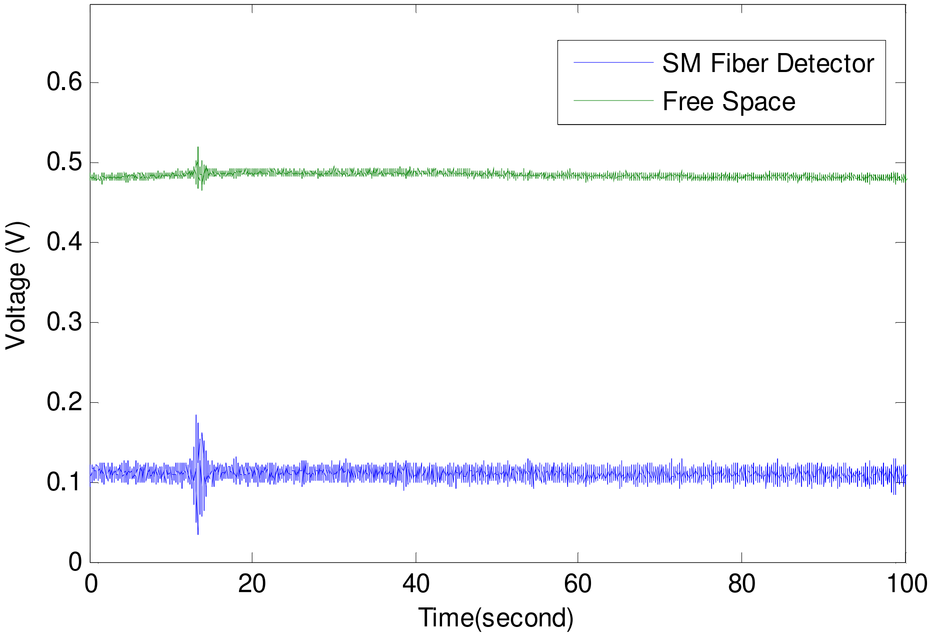

Figure 5.8 Detected IR signal with single mode fiber detector and free space detector for the source caused vibration.

5.3.1.2 Scintillation Effects study with PID Controller. The goal is to keep the optical power at the data receiver's input constant by means of the PID controller when dust enters the beam so that the BER should not change (constant signal quality). The outputs of all photo detectors are simultaneously recorded along with the BER and transmitter output power of the IR channel (Figure 5.9).

When dust is launched into the IR beam after about 20 s recording time, the PID controller enhances the IR power launched into the chamber and measured by photodetector PD-1. Up to about 50 s recording time the control loop can not compensate the power loss inside the chamber, the maximum transmitter output power is insufficient to further equalize the losses of the link until the link attenuation drops back at about 50s recording time to a level within the power margin of the system. After that, the detected optical power at the data receiver stays almost constant (for t>50 s).

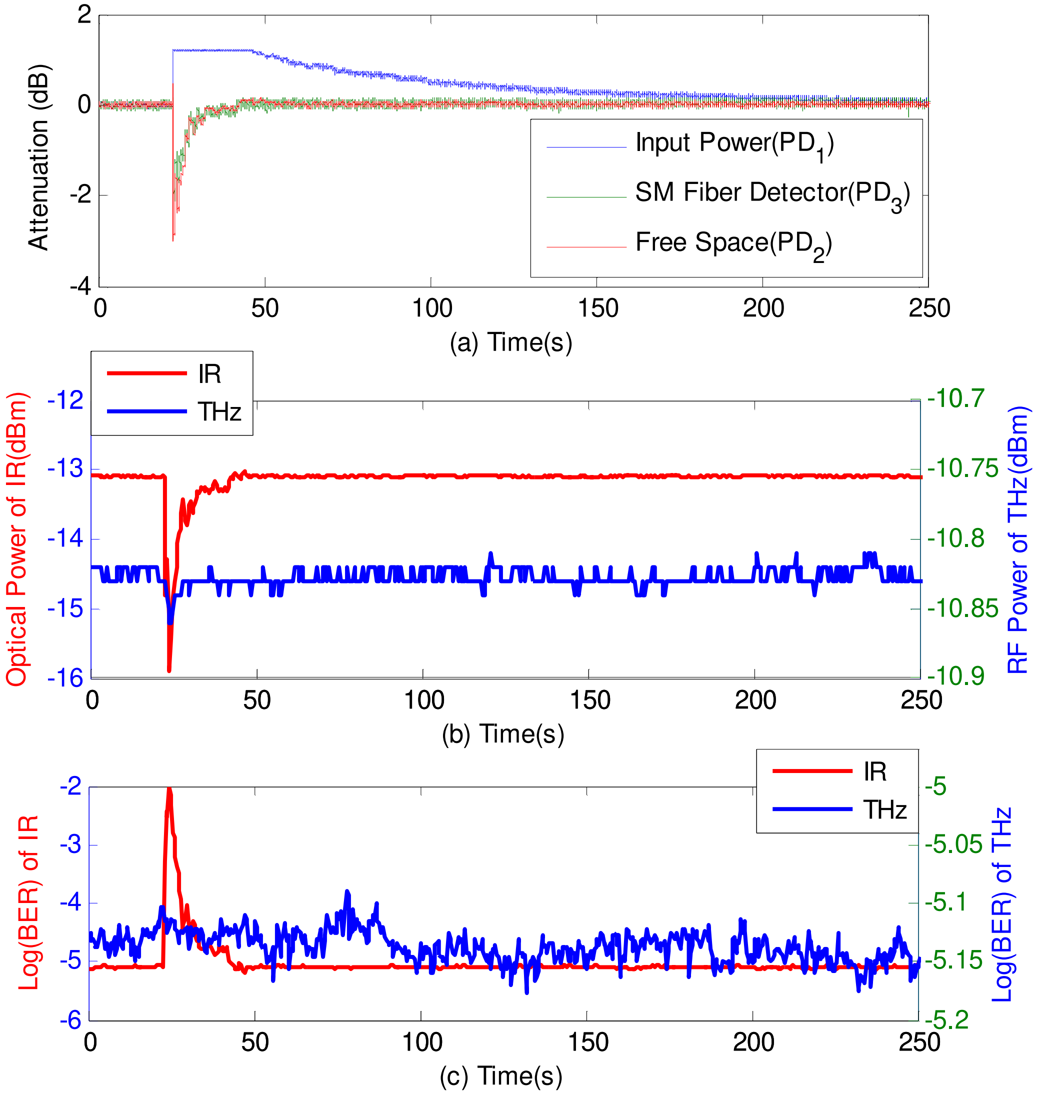

Figure 5.9 (a) Individually normalized outputs of photodetector(PD-1, PD-2, PD-3) in dB, (b) opitcal power of IR and RF power of THz due to dust, (c) Log(BER) of IR and THz links impaired by dust.

Unlike the fog, scintillation effects can not be observed in the IR links when the dust is launched. The possible reasons are listed below:

- Attenuation in the link: the attenuation due to the fog is 5 dB, which is more significant than the dust link (1.5 dB).

- Fluctuation changing speed: fog generation process causes much more irregular changes, which strengthen the scintillations effects. However, when dust is launched in the chamber, due to the force balance design, the density of the dust is changed very smoothly and slowly and the fluctuation effects will become smaller.

5.3.2 0.08 g of Dust

5.3.2.1 Transmission Link Performance with Disabled PID Controller. Figure 5.10 shows the detected signals for 0.08 gram dust. The results also showed good repeatability of all three trials.

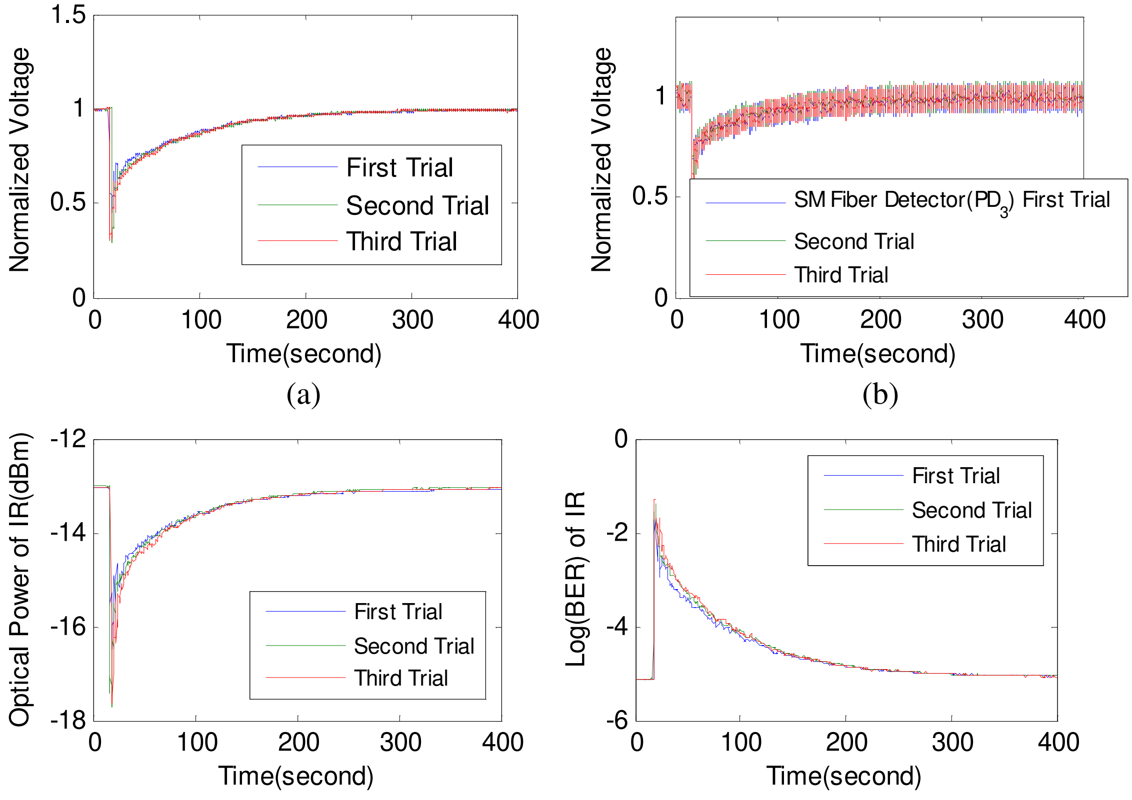

(a) (b)

(c) (d)

Figure 5.10 Detected IR signal for the 0.08gram dust (a) Free Space (PD_2) (b) SM Fiber Detector (PD_3) (c) Optical Power of IR(dBm), (d) Log(BER) of IR.

Figure 5.11 shows the comparison of IR and THz for power attenuation and BER change. Clearly there is a huge difference in the IR and THz attenuation.

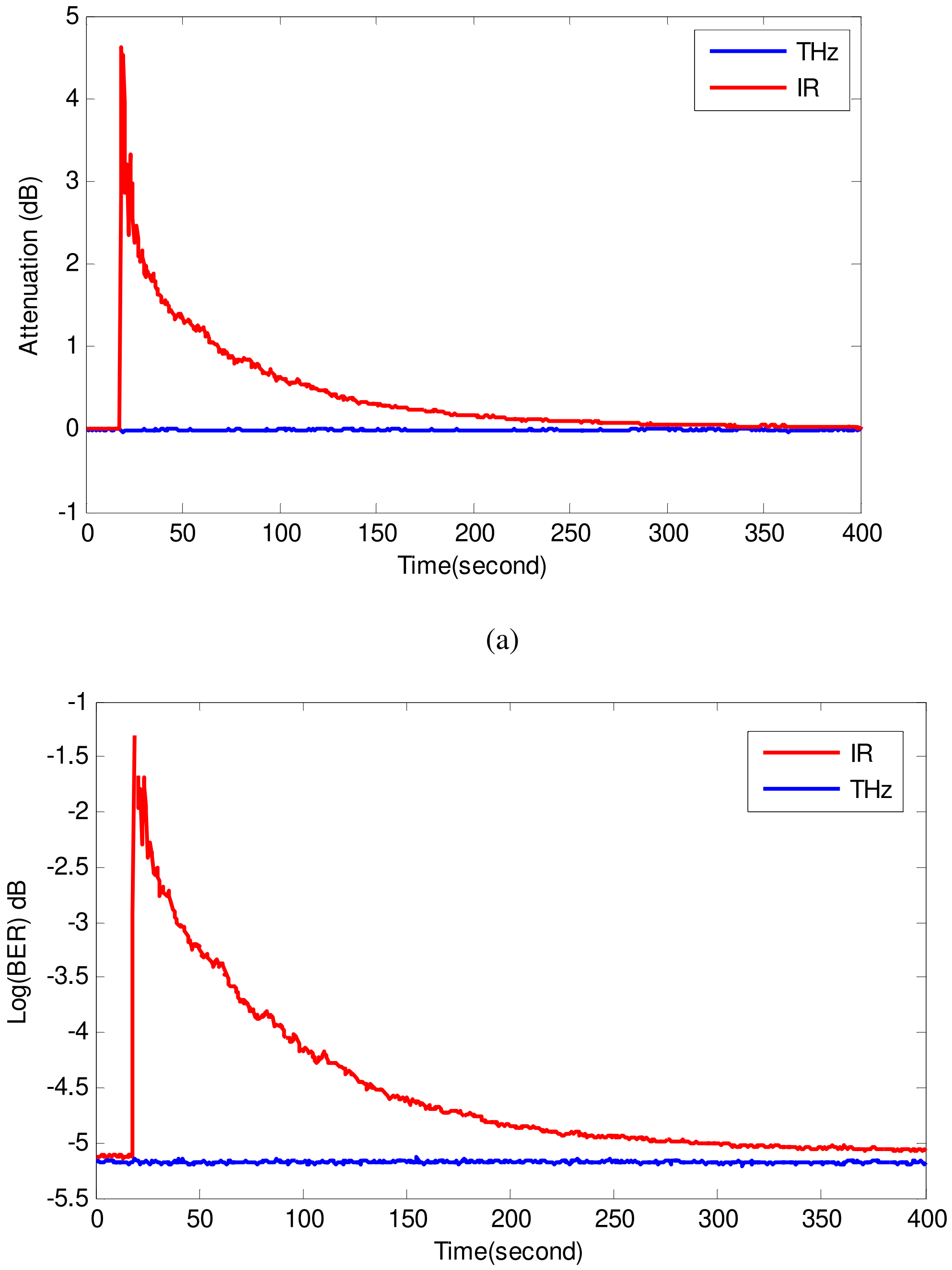

(a)

(b)

Figure 5.11 (a) Attenuation of THz link and IR link with time (0.08g) (b) Log(BER) of THz link and IR link with time.

5.3.2.2 Scintillation Effects study with PID Controller.

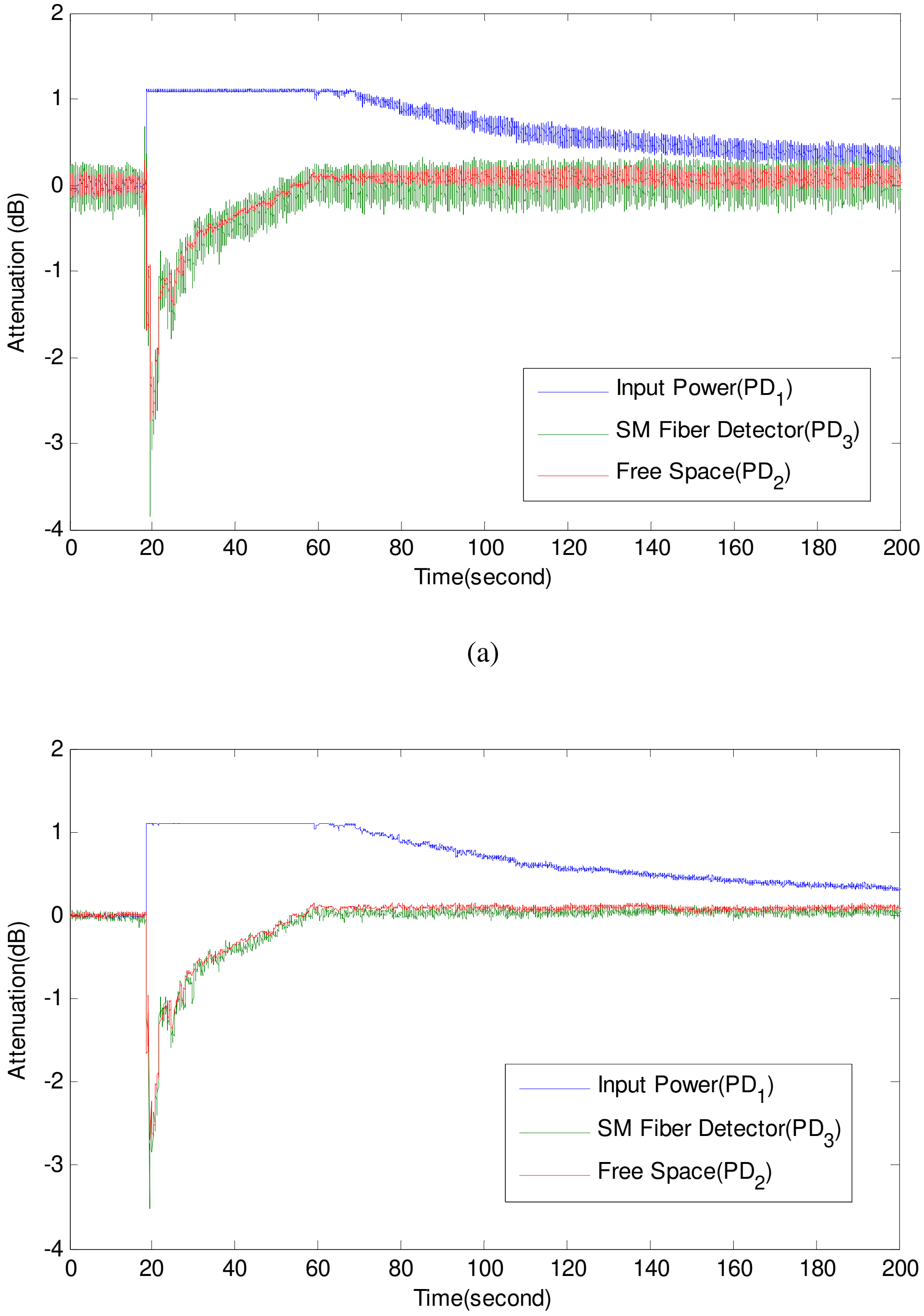

(a)

(b)

Figure 5.12 (a) Individually normalized outputs of photodetector (PD1, PD2, PD3) (b) outputs of the photodetector with noise elimination.

Scintillation effects testing are also performed for the 0.08 g of the dust. Figure 5.12 (a) shows individually normalized outputs of photodetector (PD-1, PD-2, PD-3). Still scintillation effects cannot be clearly observed in the process. In order to eliminate noise, the average has been taken for each 100 points, corresponding to 1ms and the result is shown in Figure 5.12(b), there is no evidence of scintillations effects in the links.

5.3.3 Comparison of Different Dust Densities

Three different amounts of dusts (0.05 g, 0.08 g and 0.13 g) are loaded in the dust chamber (shown in Figure 5.13). One observes that as the dust loading becomes heavier (and IR extinction increases), the IR attenuation will become much more severe as expected.

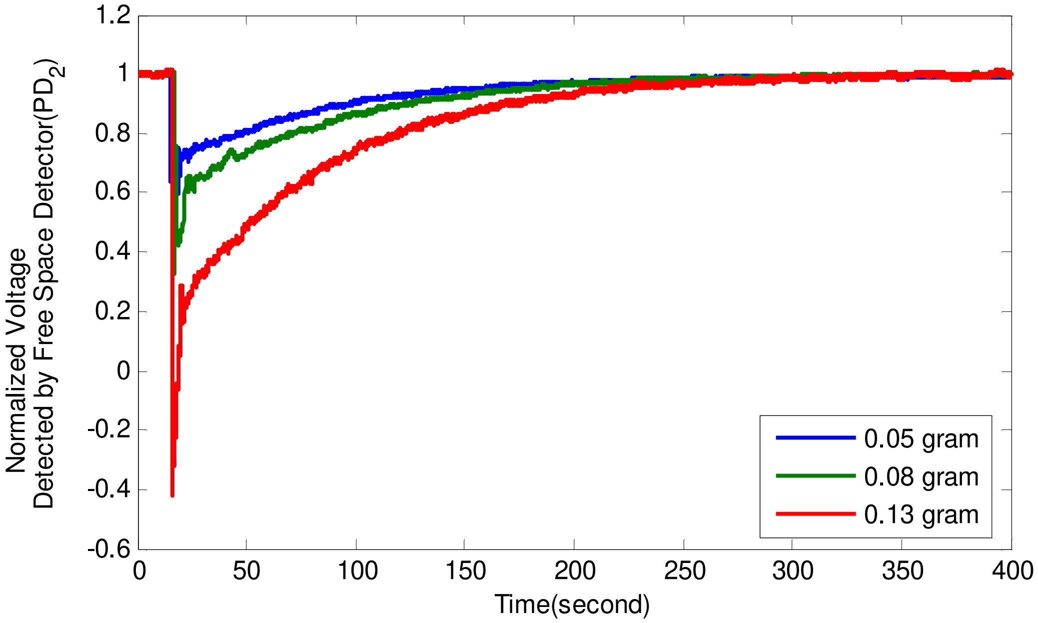

(a)

Figure 5.13 (a) Normalized voltage detected by free space detector (PD-2) for different amount of the dust.

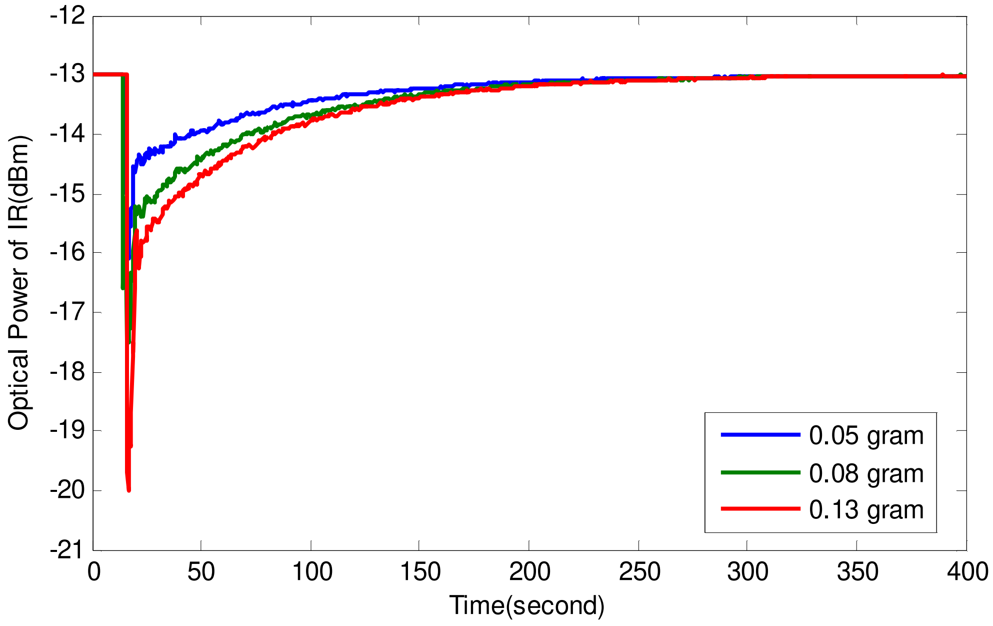

(b)

Figure 5.13 (b) Optical power of IR for different amounts of dust.

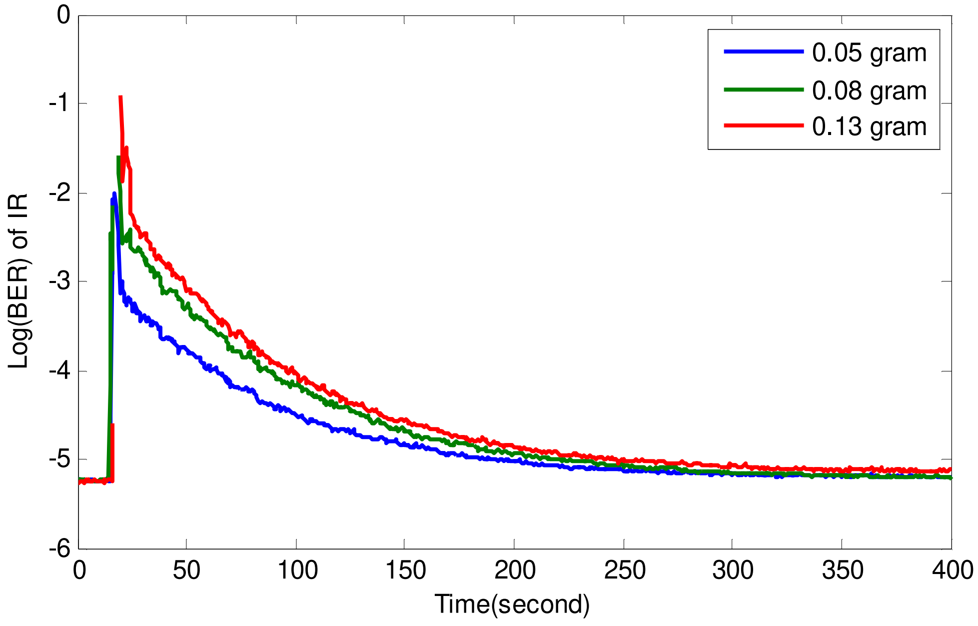

(c)

Figure 5.13 (c) Log(BER) of IR for different amounts of dust.

From Figure 5.14, one can see there is no effect on the THz links for different density of dust. Still, the peak around 14.4 seconds is due to the vibration of the beam splitter caused by the powder release shutter noise.

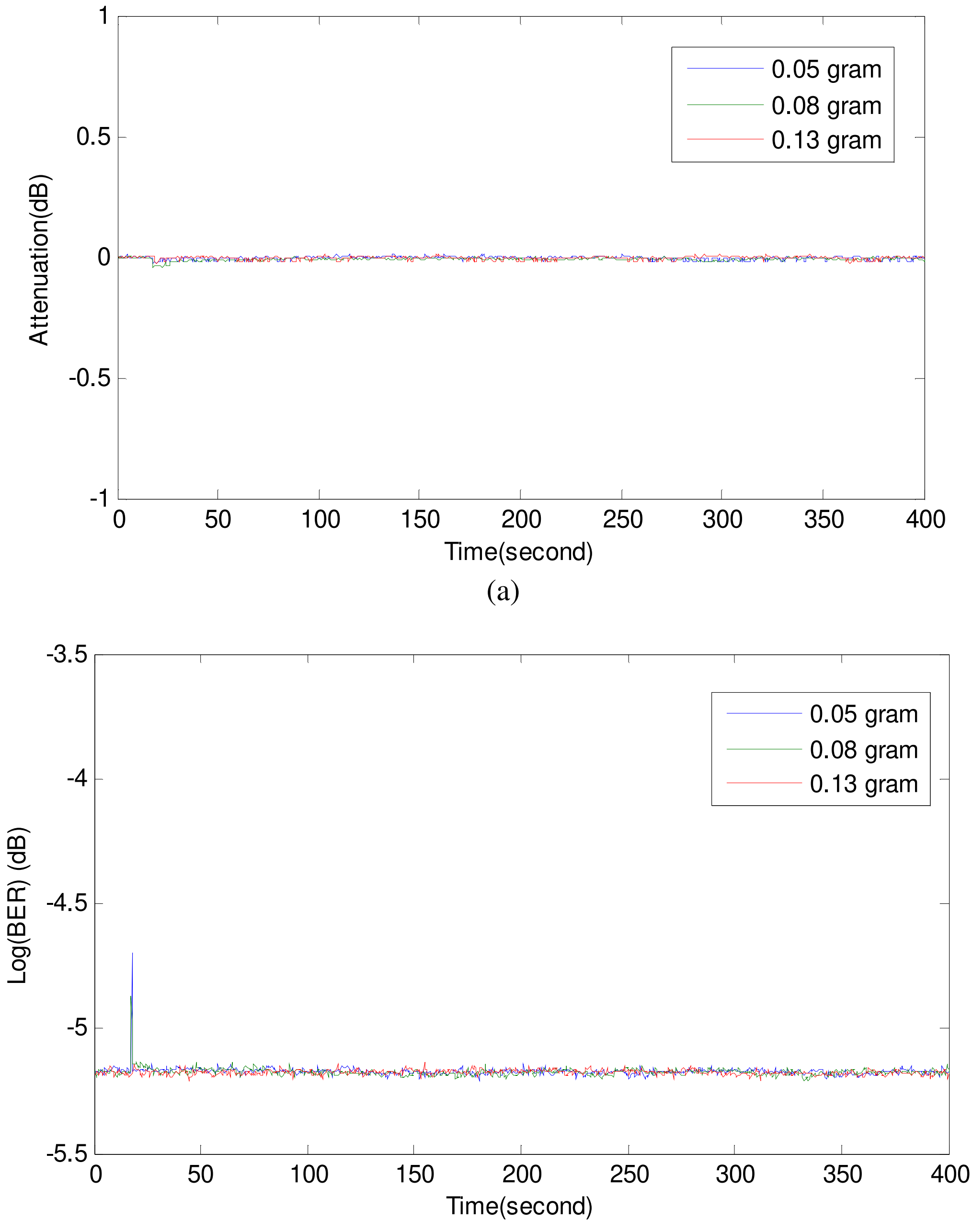

(a)

(b)

Figure 5.14 (a) Attenuation for different amount of the dust (b) Log(BER) of THz for different amounts of dust.

5.4 Simulation Results

The particle concentration is decreasing slowly with time, since all the dusts will finally fall down to the bottom of the chamber. In this section, the particle concentration at different time is estimated though the IR attenuation according Beers-Lambert Law(Chapter 4.2) and Mie scattering theory[106]. Then the THz attenuation is simulated through Mie scattering theory, which shows good agreement with the experimental data.

According to the Beers-Lambert Law, the attenuation of laser radiation through atmosphere can be expressed as (see Chapter 4.2):

$$\tau(\lambda, R) = \frac{P(\lambda, R)}{P(\lambda, 0)} = e^{-\gamma(\lambda)R} = e^{-(\alpha+\beta)R} = e^{-\beta R} = e^{-\sigma_s N_s R} \tag{5.27}$$

where $P(\lambda, R)$ is optical power at the distance R , $P(\lambda, 0)$ is initial emitted optical power, $\gamma(\lambda)$ is extinction coefficient (per unit of length). α is absorption coefficient, β is scattering coefficient, σ_s is scattering section, and N_s is particle concentration.

From Equation 5.27, the particle concentration N_s can be calculated as:

$$N_s = \frac{-\ln\left(\frac{P(\lambda, R)}{P(\lambda, 0)}\right)}{R\sigma_s} \tag{5.28}$$

The attenuation is defined as:

$$att\_dB = 10 \times \log_{10} \frac{P(\lambda, 0)}{P(\lambda, R)} \tag{5.29}$$

According the Equation 5.28 and 5.29, the relationship between the N_s and attenuation in dB can be expressed as:

$$N_s = \frac{att\_dB \times \ln 10}{10 \times R \times \sigma_s} \tag{5.30}$$

From Equation 5.24, the total extinction cross sections can be calculated as:

$$\sigma_s(v) = \frac{c^2}{2\pi v^2} \sum_{m=1}^{\infty} (2m+1)\,\mathrm{Re}(a_m + b_m) \tag{5.31}$$

According to the Mie scatter theory (Chapter 5.1.2), the total extinction cross sections can be calculated and plotted as a function of particle size parameter (Figure 5.15 a) and frequency (Figure 5.15 b). The mean size of the bentonite particle is 8.6 μm, and the real part index of refraction is 1.52. And Figure 5.15 b shows the relationship between the particle size parameter and frequency (with particle radius 8.6 μm). For wavelength of IR is 1.5 μm (200 THz), the corresponding particle size parameter $a = 33.51$ and the extinction cross section is $\sigma_s = 4.737 \times 10^{-10}$.

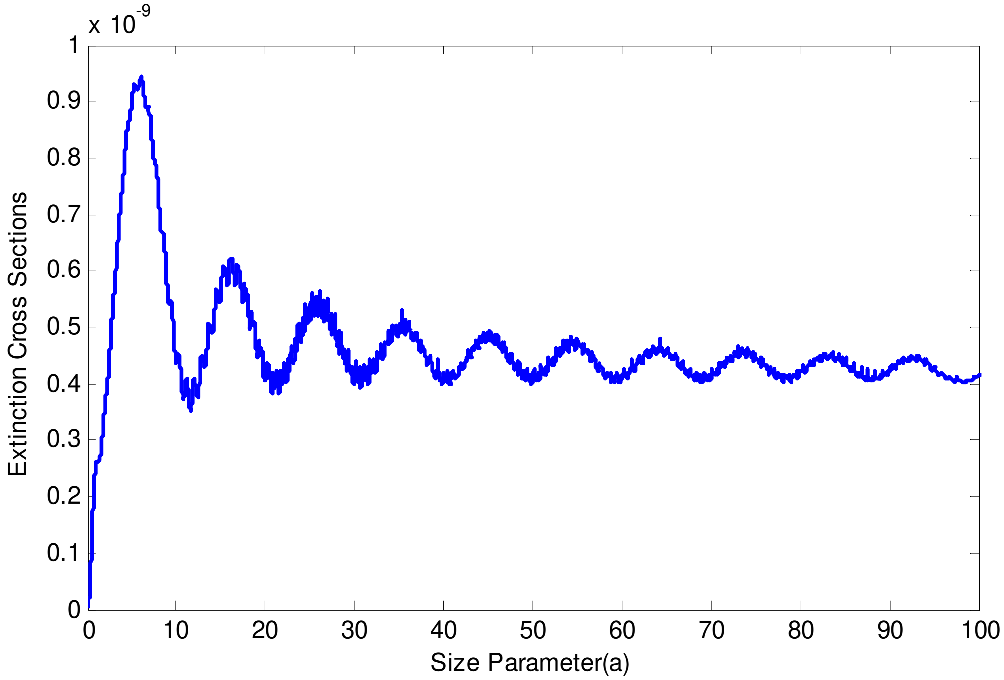

(a)

Figure 5.15 (a) The extinction efficiency as a function of size parameter.

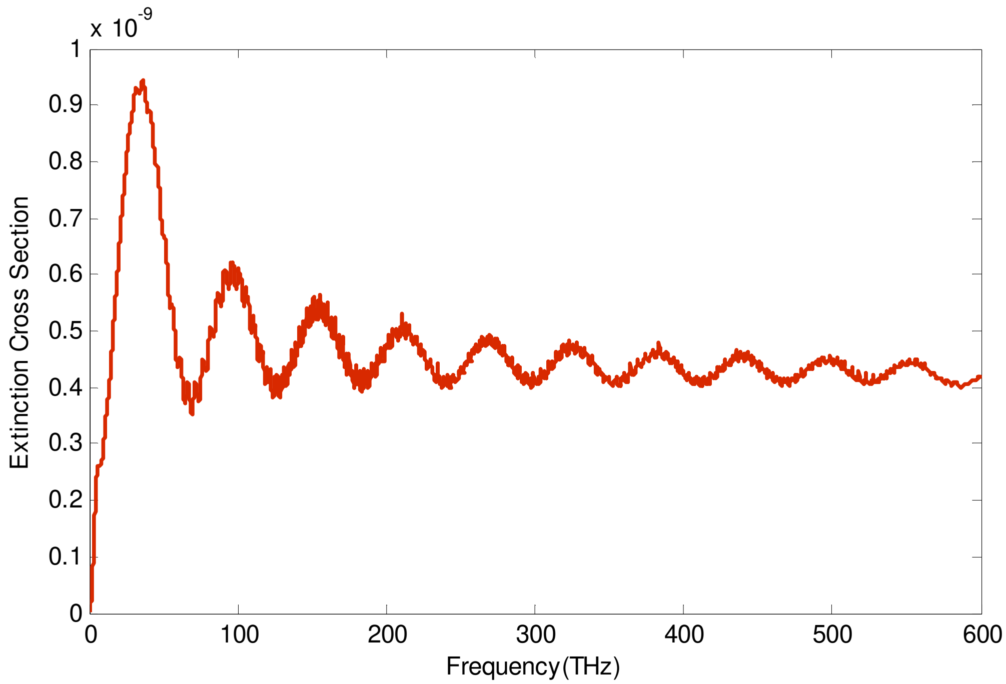

(b)

Figure 5.15 (b) The extinction efficiency as a function of frequency.

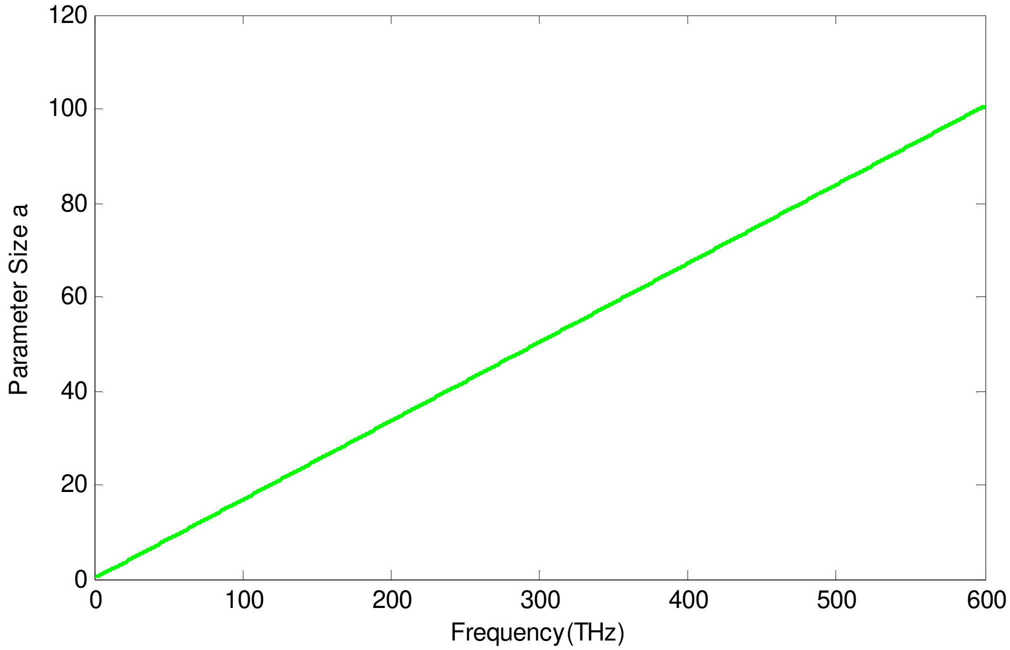

(c)

Figure 5.15 (c) The relationship between parameter size and frequency.

According to the IR attenuation data of 0.08 g of dust (Figure 5.10a) and substituting extinction cross section $\sigma_s = 4.737 \times 10^{-10}$ to Equation 5.30, the particle concentration during different time can be calculated and plotted as Figure 5.16. The particle concentration varies from $1.5 \times 10^9 / m^3$ to almost 0. Using Equations 5.24, 5.29 and 5.30, the THz attenuation with time is calculated and plotted as Figure 5.17. The maximum attenuation of the THz is 0.1, which is twice of the experimental curve shown in Figure 5.11 b. The possible reason could be in the simulation process, only mean particle size is considered. To achieve the better results, particle size distribution could be considered in the simulation process.

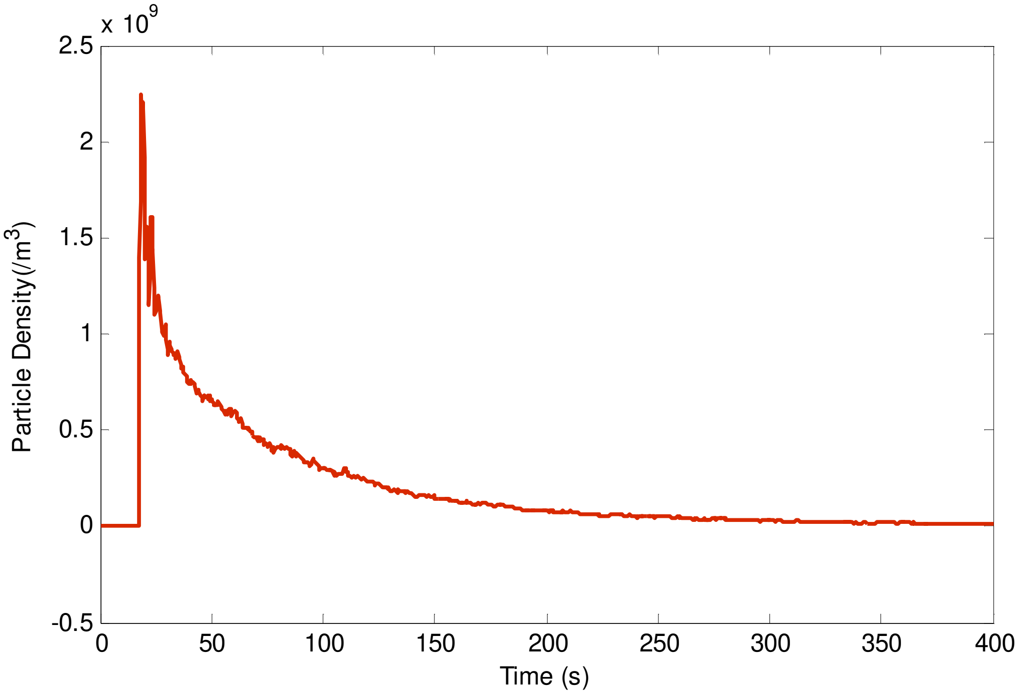

Figure 5.16 The particle density with time.

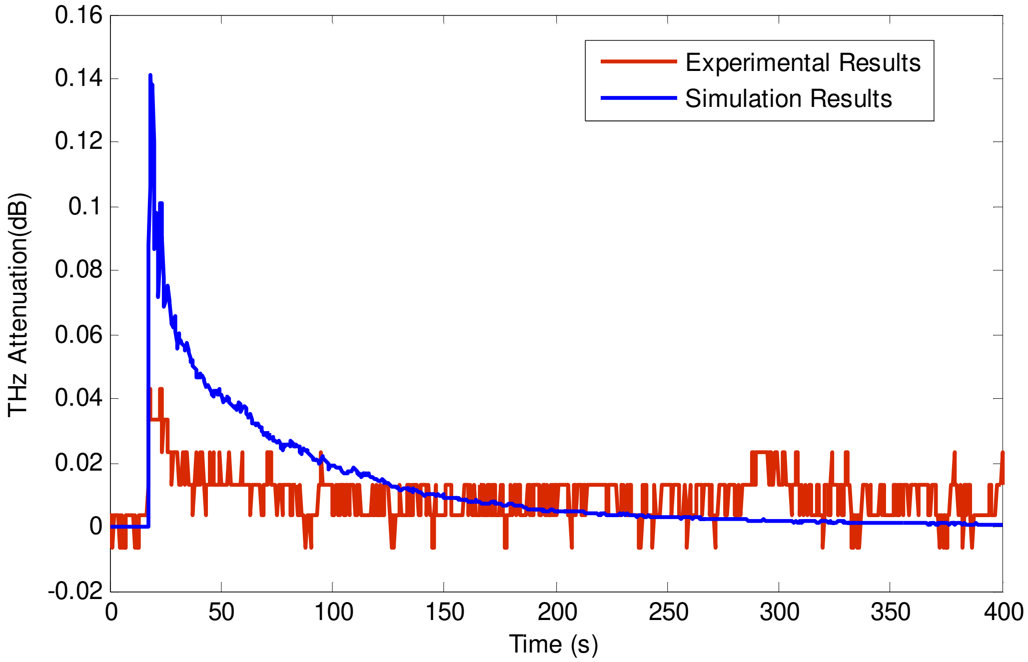

Figure 5.17 Comparison of experimental results and simulation results of THz attenuation.

CHAPTER 6

CONCLUSIONS AND FUTURE PERSPECTIVES

In this chapter, the contribution made in this dissertation research work is summarized and the future work is mentioned. The research work described in this thesis has made unique, original contributions in several areas of instrument development (625 GHz transmission link), comparison of the atmosphere attenuation due to airborne particulates (fog and dust), and experimental scintillation effects study of IR links.

6.1 Summary of Research Results

In order to study and compare propagation features of Terahertz (THz) links with Infrared (IR) links under different weather conditions such as fog and dust, a THz and IR communications lab setup with a maximum data rate of 2.5 Gb/s at 625 GHz carrier frequency and 1.5 um wavelength, respectively have been developed. A usual non return-to-zero (NRZ) format is applied to modulate the IR channel but a duobinary coding technique is used for driving the multiplier chain based 625 GHz source, which enables signaling at high data rate and higher output power. The bit-error rate (BER), signal-to-noise ratio (SNR) and power on the receiver side have been measured, which describe the signal performance.

At frequencies below 1000 GHz, the size of fog particles is considerably smaller than the carrier wavelength, so that the Rayleigh absorption can be applied to replace the much more complicated Mie scattering theory. On the frequency range from 10 GHz-1000 GHz, the attenuation by fog is modeled using a simple double-Debye model for the dielectric permittivity of water, based on the total liquid water content. In the IR range, this is no longer true and the distribution of the particle size must be considered. The specific attenuation is predicted using the empirical models, such as the Kruse, Kim and Alnabulsi models. Simulation results of attenuation by fog in the millimeter and sub-millimeter waveband (from 0.1 to 1 THz) and infrared waveband (1.5 μm) are presented and compared. An IR beam at 1.5 μm wavelength carrying the same data load is superposed with the THz beam. After propagating through the same weather conditions (fog), experimental performance of both channels are analyzed and compared.

Due to the relatively small size of atmosphere particles such as dust and smoke compared to THz wavelength, one would expect minimal THz attenuation due to airborne particulates. Gebhart et al. [47] mentions for the typical wavelengths employed by wireless IR links (780 nm and 1550 nm), attenuation due to dust is around 10dB/km in urban regions. An IR beam at 1.5 μm wavelength carrying the same data load is superposed with the THz beam (625 GHz), propagating through the same aerosol conditions (Bentonite particle with mean size of diameter 8.6 μm). The optical power attenuation and BER are measured, analyzed and compared. Under same dust concentration, IR wavelengths are strongly attenuated while THz wavelength shows almost no impact, so THz communication could apply in the battle filed or wildfire environments and for some specific link length requirements THz can enable reliable communication instead of IR based systems under dust environment. Also, different amounts of dust (0.05 g, 0.08 g and 0.13 g) are loaded in the chamber to generate different dust concentration environment. As the dust loading becomes heavier (and extinction increases), the attenuation will become more severe.

6.2 Future Work

As mentioned above, atmosphere attenuation caused by fog and dust are investigated theoretically and experimentally in this thesis dissertation. The characteristics and effects of other atmosphere phenomena to which outdoor wireless links are exposed, such as rain, humidity, turbulence should be studied in the future research work.

REFERENCES

1. G. K. Kitaeva, "Terahertz generation by means of optical lasers," Laser Physics Letters **5**, 559-576 (2008).

2. K. Vodopyanov, "Terahertz-wave generation with periodically inverted gallium arsenide," Laser Physics **19**, 305-321 (2009).

3. V. Bratman, M. Glyavin, T. Idehara, Y. Kalynov, A. Luchinin, V. Manuilov, S. Mitsudo, I. Ogawa, T. Saito, Y. Tatematsu, and V. Zapevalov, "Review of subterahertz and terahertz gyrodevices at IAP RAS and FIR FU," Plasma Science, IEEE Transactions on **37**, 36-43 (2009).

4. R. Appleby and H. B. Wallace, "Standoff detection of weapons and contraband in the 100 GHz to 1 THz region," Antennas and Propagation, IEEE Transactions on **55**, 2944-2956 (2007).

5. J. F. Federici, D. Gary, R. Barat, and Z.-H. Michalopoulou, "Detection of explosives by terahertz imaging," in *Counter-Terrorist Detection Techniques of Explosives*, J. Yinon, ed. (Elsevier, Boston, MA, 2007).

6. A. Sinyukov, I. Zorych, Z.-H. Michalopoulou, D. Gary, R. Barat, and J. F. Federici, "Detection of explosives by Terahertz synthetic aperture imaging—focusing and spectral classification," Comptes Rendus Physique **9**, 248-261 (2008).

7. K. Ajito and Y. Ueno, "THz chemical imaging for biological applications," Terahertz Science and Technology, IEEE Transactions on **1**, 293-300 (2011).

8. P. H. Siegel, "Terahertz technology in biology and medicine," Microwave Theory and Techniques, IEEE Transactions on **52**, 2438-2447 (2004).

9. J. F. Federici, R. L. Wample, D. Rodriguez, and S. Mukherjee, "Application of terahertz Gouy phase shift from curved surfaces for estimation of crop yield," Appl. Opt. **48**, 1382-1388 (2009).

10. Y. L. Hor, J. F. Federici, and R. L. Wample, "Nondestructive evaluation of cork enclosures using terahertz/millimeter wave spectroscopy and imaging," Appl. Opt. **47**, 72-78 (2008).

11. S. Cherry, "Edholm's law of bandwidth," Spectrum, IEEE **41**, 58-60 (2004).

12. P. Zhouyue and F. Khan, "An introduction to millimeter-wave mobile broadband systems," Communications Magazine, IEEE **49**, 101-107 (2011).

13. M. Koch, "Terahertz communications: A 2020 vision," in *Terahertz Frequency Detection and Identification of Materials and Objects*, R. E. Miles, X.-C. Zhang, H. Eisele, and A. Krotkus, eds. (Springer Science and Business Media, Dordrecht, The Netherlands 2007), pp. 325-338.

14. V. Jungnickel, T. Haustein, A. Forck, and C. v. Helmolt, "155 Mbit/s wireless transmission with imaging infrared receiver," Electronics Letters **37**, 314-315 (2001).

15. R. Piesiewicz, T. Kleine-Ostmann, N. Krumbholz, D. Mittleman, M. Koch, J. Schoebel, and T. Kurner, "Short-range ultra-broadband terahertz communications: concepts and perspectives," Antennas and Propagation Magazine, IEEE **49**, 24-39 (2007).

16. J. F. Federici and L. Moller, "Review of terahertz and subterahertz wireless communications," J. Appl. Phys. **107**, 111101 (2010).

17. T. Kleine-Ostmann, K. Pierz, G. Hein, P. Dawson, and M. Koch, "Audio signal transmission over THz communication channel using semiconductor modulator," Electronics Letters **40**, 124-126 (2004).

18. T.-A. Liu, G.-R. Lin, Y.-C. Chang, and C.-L. Pan, "Wireless audio and burst communication link with directly modulated THz photoconductive antenna," Opt. Express **13**, 10416-10423 (2005).

19. L. Möller, J. Federici, A. Sinyukov, C. Xie, H. C. Lim, and R. C. Giles, "Data encoding on terahertz signals for communication and sensing," Opt. Lett. **33**, 393-395 (2008).

20. A. Hirata, T. Kosugi, N. Meisl, T. Shibata, and T. Nagatsuma, "High-directivity photonic emitter using photodiode module integrated with HEMT amplifier for 10-Gbit/s wireless link," Microwave Theory and Techniques, IEEE Transactions on **52**, 1843-1850 (2004).

21. A. Hirata, H. Takahashi, R. Yamaguchi, T. Kosugi, K. Murata, T. Nagatsuma, N. Kukutsu, and Y. Kado, "Transmission characteristics of 120-GHz-band wireless link using radio-on-fiber technologies," Lightwave Technology, Journal of **26**, 2338-2344 (2008).

22. A. Hirata, "10-Gbit/s wireless communications technology using sub-terahertz waves," Proc. SPIE **6772**, 67720B (2007).

23. G. Ducournau, P. Szriftgiser, D. Bacquet, A. Beck, T. Akalin, E. Peytavit, M. Zaknoune, and J. F. Lampin, "Optically power supplied Gbit/s wireless hotspot using 1.55 um THz photomixer and heterodyne detection at 200 GHz," Electronics Letters **46**, 1349-1351 (2010).

24. H. J. Song, K. Ajito, A. Hirata, A. Wakatsuki, T. Furuta, N. Kukutsu, and T. Nagatsuma, "Multi-gigabit wireless data transmission at over 200-GHz," in *34th International Conference on Infrared, Millimeter, and Terahertz Waves,* (2009), pp. 1-2.

25. H. J. Song, K. Ajito, A. Hirata, A. Wakatsuki, Y. Muramoto, T. Furuta, N. Kukutsu, T. Nagatsuma, and Y. Kado, "8 Gbit/s wireless data transmission at 250 GHz," Electronics Letters **45**, 1121-1122 (2009).

26. T. Nagatsuma, H. Ito, and T. Ishibashi, "High-power RF photodiodes and their applications," Laser & Photonics Reviews **3**, 123-137 (2009).

27. T. Kleine-Ostmann and T. Nagatsuma, "A review on terahertz communications research," Journal of Infrared, Millimeter and Terahertz Waves **32**, 143-171 (2011).

28. R. Yamaguchi, A. Hirata, T. Kosugi, H. Takahashi, N. Kukutsu, T. Nagatsuma, Y. Kado, H. Ikegawa, H. Nishikawa, and T. Nakayama, "10-Gbit/s MMIC wireless link exceeding 800 meters," in *Radio and Wireless Symposium, IEEE*, 2008), 695-698.

29. A. Hirata, T. Kosugi, H. Takahashi, J. Takeuchi, K. Murata, N. Kukutsu, Y. Kado, S. Okabe, T. Ikeda, F. Suginosita, K. Shogen, H. Nishikawa, A. Irino, T. Nakayama, and N. Sudo, "5.8-km 10-Gbps data transmission over a 120-GHz-band wireless link," in *Wireless Information Technology and Systems (ICWITS), 2010 IEEE International Conference on*, 2010), 1-4.

30. C. Jastrow, K. Munter, R. Piesiewicz, T. Kurner, M. Koch, and T. Kleine-Ostmann, "300 GHz channel measurement and transmission system," in *IRMMW-THz 33rd International Conference on Infrared, Millimeter and Terahertz Waves*, 2008), 1-2.

31. C. Jastrow, S. Priebe, B. Spitschan, J. Hartmann, M. Jacob, T. Kurner, T. Schrader, and T. Kleine-Ostmann, "Wireless digital data transmission at 300 GHz," Electronics Letters **46**, 661-663 (2010).

32. L. Moeller, J. Federici, and K. Su, "2.5 Gbit/s duobinary signalling with narrow bandwidth 0.625 terahertz source," Electronics Letters **47**, 856-858 (2011).

33. H. C. Liu, L. Hui, S. Chun-ying, Z. R. Wasilewski, A. J. SpringThorpe, and J. C. Cao, "Terahertz Quantum Well Photodetectors," Selected Topics in Quantum Electronics, IEEE Journal of **14**, 374-377 (2008).

34. P. D. Grant, S. R. Laframboise, R. Dudek, M. Graf, A. Bezinger, and H. C. Liu, "Terahertz free space communications demonstration with quantum cascade laser and quantum well photodetector," Electronics Letters **45**, 952-954 (2009).

35. J. F. Federici, L. Moeller, and K. Su, "Terahertz communications " in *Handbook of Terahertz Technology for Imaging and Sensing* (2011).

36. T. Kosugi, M. Tokumitsu, T. Enoki, M. Muraguchi, A. Hirata, and T. Nagatsuma, "120-GHz Tx/Rx chipset for 10-Gbit/s wireless applications using 0.1 um-gate InP HEMTs," in *Compound Semiconductor Integrated Circuit Symposium, 2004. IEEE*, 2004), 171-174.

37. G. Planinsic, "Infrared thermal imaging: fundamentals, research and applications," European Journal of Physics **32**, 1431 (2011).

38. N. T. Hunt, "2D-IR spectroscopy: ultrafast insights into biomolecule structure and function," Chemical Society Reviews **38**, 1837-1848 (2009).

39. P. Zappi, E. Farella, and L. Benini, "Tracking motion direction and distance with pyroelectric IR sensors," Sensors Journal, IEEE **10**, 1486-1494 (2010).

40. K. Krishnamurthy, H. K. Khurana, J. Soojin, J. Irudayaraj, and A. Demirci, "Infrared heating in food processing: an overview," Comprehensive Reviews in Food Science and Food Safety **7**, 2-13 (2008).

41. J. M. Kahn and J. R. Barry, "Wireless infrared communications," Proceedings of the IEEE **85**, 265-298 (1997).

42. K. D. Langer and J. Grubor, "Recent developments in optical wireless communications using infrared and visible light," in *ICTON 9th International Conference on Transparent Optical Networks,* (2007), pp. 146-151.

43. J. R. Barry, J. M. Kahn, E. A. Lee, and D. G. Messerschmitt, "High-speed nondirective optical communication for wireless networks," Network, IEEE **5**, 44-54 (1991).

44. K. S. Natarajan, K. C. Chen, and P. D. Hortensius, "Considerations for the design of high speed wireless optical networks," IEEE Workshop on Wireless LANs, 140-143 (1991).

45. D. Kedar and S. Arnon, "Urban optical wireless communication networks: the main challenges and possible solutions," Communications Magazine, IEEE **42**, S2-S7 (2004).

46. R. Ramire-Iniguez, S. M. Idrus, and Z. Sun, *Optical Wireless Communications: IR for Wireless Connectivity* (Auerbach Publications, Boca Raton, FL, 2008).

47. M. Gebhart, E. Leitgeb, and J. Bregenzer, "Atmospheric effects on optical wireless links," in *Proceedings of the 7th International Conference on Telecommunications,* (2003), pp. 395-401 vol.392.

48. A. Al-habasch, K. W. Fischer, C. S. Cornish, K. N. Desmet, and J. Nash, "Comparison between experimental and theoretical probability of fade for free space optical communications," Optical Wireless Communications V, Proceedings of SPIE **4873**, 79-89 (2002).

49. MMW_Concepts, retrieved 11/01/2011, http://mmwconcepts.com/home.html.

50. E. R. Brown, "THz generation by photomixing in ultrafast photoconductors," in *Terahertz Sensing Technology*, D. L. Woolard, W. R. Loerop, and M. Shur, eds. (World Scientific, River Edge, NJ, 2003).

51. Y. Yang, A. Shutler, and D. Grischkowsky, "Measurement of the transmission of the atmosphere from 0.2 to 2 THz," Opt. Express **19**, 8830-8838 (2011).

52. S. A. Khan, A. N. Tawfik, C. J. Gibbins, and B. C. Gremont, "Extra-high frequency line-of-sight propagation for future urban communications," Antennas and Propagation, IEEE Transactions on **51**, 3109-3121 (2003).

53. T. Utsunomiya and M. Sekine, "Rain attenuation at 103 GHz in millimeter wave ranges," International Journal of Infrared and Millimeter Waves **26**, 1651-1660 (2005).

54. A. Hirata, R. Yamaguchi, H. Takahashi, T. Kosugi, K. Murata, N. Kukutsu, and Y. Kado, "Effect of Rain Attenuation for a 10-Gb/s 120-GHz-Band Millimeter-Wave Wireless Link," Microwave Theory and Techniques, IEEE Transactions on **57**, 3099-3105 (2009).

55. S. Ishii, S. Sayama, and T. Kamei, "Measurement of rain attenuation in terahertz wave range," Wireless Engineering and Technology **2**, 119-124 (2011).

56. K. Su, L. Moeller, R. Barat, and J. F. Federici, " Experimental comparison of performance degradation from terahertz and infrared wireless link in fog," Journal of the Optical Society of America A: Optics and Image Science, and Vision (Accepted) (2011).

57. C. M. Mann, "Towards terahertz communications systems " in *Terahertz Sources and Systems*, R. E. Miles, P. Harrison, and D. Lippens, eds. (Kluwer Academic Norwell, MA, 2001).

58. M. Al-Habash, "Mathematical model for the irradiance probability density function of a laser beam propagating through turbulent media," Opt. Eng. **40**, 1554 (2001).

59. L. C. Andrews and R. L. Phillips, "I-K distribution as a universal propagation model of laser beams in atmospheric turbulence," J. Opt. Soc. Am. A **2**, 160-163 (1985).

60. Z. Liu, K. Su, D. E. Gary, J. F. Federici, R. B. Barat, and Z.-H. Michalopoulou, "Video-rate terahertz interferometric and synthetic aperture imaging," Appl. Opt. **48**, 3788-3795 (2009).

61. K. Su, Z. Liu, R. B. Barat, D. E. Gary, Z.-H. Michalopoulou, and J. F. Federici, "Two-dimensional interferometric and synthetic aperture imaging with a hybrid terahertz/ millimeter wave system," Appl. Opt. **49**, E13-E19 (2010).

62. A. M. Sinyukov, Z. Liu, Y. L. Hor, K. Su, R. B. Barat, D. E. Gary, Z.-H. Michalopoulou, I. Zorych, J. F. Federici, and D. Zimdars, "Rapid-phase modulation of terahertz radiation for high-speed terahertz imaging and spectroscopy," Opt. Lett. **33**, 1593-1595 (2008).

63. L. Moeller, J. F. Federici, and K. Su, "THz wireless communications: 2.5 Gb/s error-free transmission at 625 GHz using a narrow-bandwidth 1 mW THz source," in *General Assembly and Scientific Symposium, URSI,* (Istanbul 2011).

64. A. Visioli, *Practical PID control* (Springer, London, 2006).

65. S. M. Duffy, S. Verghese, and K. A. McIntosh, in *Sensing with Terahertz Radiation*, D. Mittleman, ed. (Springer, Berlin, 2003).

66. E. R. Brown, "Electronic devices and advanced systems technology " in *Terahertz Sensing Technology*, D. L. Woolard, W. R. Loerop, and M. S. Shur, eds. (World Scientific NJ, 2003).

67. E. F. Plinski, "Terahertz photomixer," Bulletin of the Polish Academy of Sciences **58**(2010).

68. Toptica, retrieved 11/01/2011, http://www.toptica.com/.

69. M. Wirts, "Method and device for measuring and stabilization using signals from a Fabry-Perot," (2001).

70. P. Kordos, M. Marso, and M. Mikulics, "Performance optimization of GaAs-based photomixers as sources of THz radiation," Applied Physics A: Materials Science & Processing **87**, 563-567 (2007).

71. K. Sakai, *Terahertz Optoelectronics*, Topics in applied physics (Springer, Berlin, 2005).

72. D. Penninckx, M. Chbat, L. Pierre, and J. P. Thiery, "The phase-shaped binary transmission (PSBT): a new technique to transmit far beyond the chromatic dispersion limit," Photonics Technology Letters, IEEE **9**, 259-261 (1997).

73. A. Lender, "The duobinary technique for high-speed data transmission," IEEE Trans. Commun. Electron. **82**, 214-218 (1963).

74. S. Haykin, *Digital Communications* (Wiley, New York, 1988).

75. T. W. Crowe, D. W. Porterfield, J. L. Hesler, and W. L. Bishop, "Submillimeter-wave and terahertz diodes, components and subsystems," in *Infrared Millimeter Waves and 14th International Conference on Teraherz Electronics, Joint 31st International Conference on IRMMW-THz,* (2006), pp. 396-396.

76. T. Mizuochi, "Recent progress in forward error correction and its interplay with transmission impairments," Selected Topics in Quantum Electronics, IEEE Journal of **12**, 544-554 (2006).

77. H. C. van de Hulst, *Light Scattering by Small Particles*, Structure of matter series (Wiley, New York, 1957).

78. H. J. Liebe, T. Manabe, and G. A. Hufford, "Millimeter-wave attenuation and delay rates due to fog/cloud conditions," Antennas and Propagation, IEEE Transactions on **37**, 1617-1612 (1989).

79. D. Deirmendjian, *Electromagnetic Scattering on Spherical Polydispersions* (Elsevier, New York, 1969).

80. L. W. Abreu and G. P. Anderson, "The MODTRAN 2/3 Report and LOWTRAN 7 MODEL," F19628-91-C-0132 (1996).

81. "LOWTRAN 7: Status, review, and impact for short-to-long-wavelength infrared applications," in *AGARD, Atmospheric Propagation in the UV, Visible, IR, and MM-Wave Region and Related Systems Aspects,* F. X. Kneizys, G. P. Anderson, E. P. Shettle, L. W. Abreu, J. H. Chetwynd, J. E. A. Selby, W. O. Gallery, and S. A. Clough, eds. (1990).

82. S. A. Clough, F. X. Kneizys, E. P. Shettle, and G. P. Anderson, "Atmospheric radiance and transmittance: FASCOD2," in *Sixth Conference on Atmospheric Radiation, American Meteorological Society,* (Boston, MA, 1986), p. 141.

83. S. A. Clough, F. X. Kneizys, L. S. Rothman, and W. O. Gallery, "Atmospheric spectral transmittance and radiance - FASCOD1B," in *Atmospheric transmission*, (SPIE - The International Society for Optical Engineering, 1981), 152-166.

84. P. W. Kruse, L. D. McGlauchilin, and R. B. McQuistan, *Elements of Infrared Technology: Generation, Transmission and Detection* (Wiley, New York, 1962).

85. I. Kim, B. McArthur, and E. Korevaar, "Comparison of laser beam propagation at 785 and 1550 nm in fog and haze for optical wireless communications," in *Proc. SPIE* (2001), pp. 26-37.

86. M. Alnaboulsi, H. Sizun, and F. de Fornel, "Fog attenuation prediction for optical and infrared waves," Optical Engineering **43**, 11 (2004).

87. I. Gultepe, *Fog and Boundary Layer Clouds: Fog Visibility and Forecasting* (Birkhauser Basel, Toronto, Canada, 2007).

88. H. R. Byers, *General Meteorology* (McGraw-Hill, New York, 1959).

89. H. G. Houghton, "The transmission of visible light through fog," Physical Review **38**, 152 (1931).

90. H. G. Houghton and W. H. Radford, "On the measurement of drop size and liquid water content in fogs and clouds," Physical Oceanography and Meteorology **6**(1938).

91. H. Weichel, *Laser Beam Propagation in the Atmosphere* (SPIE, Bellingham, WA, 1990).

92. D. Harris, "The attenuation of electromagnetic waves due to atmospheric fog," International Journal of Infrared and Millimeter Waves **16**, 1091-1108 (1995).

93. J. M. Wallace and P. V. Hobbs, *Atmospheric Science: An Introductory Survey* (Academic Press, Orlando, FL, 1977).

94. W. E. K. Middleton, *Vision Through the Atmosphere* (University of Toronto Press, Toronto, Canada, 1952).

95. L. C. Andrews and R. L. Phillips, *Laser Beam Propagation through Random Media* (SPIE Press, Bellingham, WA, 1998).

96. R. L. Freeman, *Radio system design for telecommunications* 2nd ed. (Wiley, New York 1997).

97. "ITU-R recommendation P.840-4: attenuation due to clouds and fog," (International Telecommunication Union (ITU), Switzerland, 2009).

98. Z. Zhao and Z. Wu, "Millimeter-wave attenuation due to fog and clouds," International Journal of Infrared and Millimeter Waves **21**, 1607-1615 (2000).

99. J. Williams, "Infrared Transmission and Path Radiance through Dust and Fog," (Army Research Lab., MD, 1993).

100. Picarin, "Microtech Instrument, Inc", retrieved 11/01/2011, http://www.mtinstruments.com/.

101. T. L. Heath, *The Works of Archimedes* (Cambridge University Press, UK, 1897).

102. G. D. Brunton, "Density and compressibility of wyoming bentonite particles," Clays and Clay Minerals **36**, 94-95 (1988).

103. O. Reynolds, "An experimental investigation of the circumstances which determine whether the motion of water shall be direct or sinuous, and of the law of resistance in parallel channels," Proceedings of the Royal Society of London **35**, 84-99 (1883).

104. *Crane Technical Paper No. 410 "Flow of Fluids through Valves, Fittings, and Pipe"* (Crane Co., Michigan, 1988).

105. R. J. Emrich, *Fluid Dynamics*, Methods of Experimental Physics (Academic Press, New York, 1981), Vol. 18.

106. C. F. Bohren and D. R. Huffman, *Absorption and Scattering of Light by Small Particles* (Wiley, New York, 1983).

107. *Handbook of Mathematical Functions: with Formulas, Graphs, and Mathematical Tables* (Dover Publications, Mineola, NY, 1964).